ADVANCING ATOMIC FORCE MICROSCOPY-SCANNING ELECTROCHEMICAL MICROSCOPY BASED SENSING PLATFORMS FOR BIOLOGICAL APPLICATIONS

A Thesis
Presented to
The Academic Faculty

By

Justyna Wiedemair

In Partial Fulfillment
Of the Requirements for the Degree
Doctor of Philosophy in Chemistry

Georgia Institute of Technology

May 2009

ADVANCING ATOMIC FORCE MICROSCOPY-SCANNING ELECTROCHEMICAL MICROSCOPY BASED SENSING PLATFORMS FOR BIOLOGICAL APPLICATIONS

Approved by:

Dr. Boris Mizaikoff, Advisor
School of Chemistry and Biochemistry
Georgia Institute of Technology

Dr. Facundo M. Fernandez
School of Chemistry and Biochemistry
Georgia Institute of Technology

Dr. Christine Kranz, Co-advisor
School of Chemistry and Biochemistry
Georgia Institute of Technology

Dr. Frank E. Loeffler
School of Civil and Environmental Engineering
Georgia Institute of Technology

Dr. Douglas C. Eaton
Department of Physiology
Emory University

Dr. L. Andrew Lyon
School of Chemistry and Biochemistry
Georgia Institute of Technology

Date Approved: March 13, 2009

ACKNOWLEDGEMENTS

I would like to thank Dr. Boris Mizaikoff and Dr. Christine Kranz for giving me the opportunity to work with them during my graduate studies. I deeply appreciate their guidance, encouragements and a highly creative environment. I also wish to thank present and past members of the Applied Sensors Laboratory for support and friendship during the last years. Particularly I am indebted to Dr. Heungjoo Shin and Jong-Seok Moon for their much appreciated assistance in the cleanroom. Moreover I would like to extend my thanks to Dr. James Bradshaw, former member of the School of Chemistry and Biochemistry, for constructing the furnace used throughout the annealing studies.

I am appreciative of Dr. Douglas Eaton, Dr. Facundo Fernandez, Dr. Frank Loeffler and Dr. Andrew Lyon for serving as committee members and for providing critical feedback and input. Additionally I wish to thank Dr. Douglas Eaton and Billie Jeanne Duke from Emory University for providing and culturing the cell samples utilized throughout this work. Dr. Karl Booksh and Dr. Nicola Menegazzo from the University of Delaware are gratefully acknowledged for collaborative work on the Raman spectroscopic studies and many supportive discussions. Also I would like to thank Dr. Dennis Hess and Balamurali Balu from the School of Chemical and Biomolecular Engineering for collaborating on the PFE portion of this work. Moreover I am grateful for financial support from the National Institute of Health (NIH grant R01 EB000508).

At last, special thanks go to my family and friends. All of this work would never have been possible without their unconditional support during my studies, endless encouragements and a lot of patience.

TABLE OF CONTENTS

LIST OF TABLES

LIST OF FIGURES

LIST OF ABBREVIATONS

AD/DA	Analog digital/digital analog
AFM	Atomic force microscopy/microscope
AFM-SECM	Atomic force microscopy-scanning electrochemical microscopy
AgQRE	Silver quasi reference electrode
AM	Amplitude modulation
ATP	Adenosine triphosphate
cAMP	Cyclic adenosine monophosphate
CE	Counter electrode
CF	Cystic fibrosis
CFTR	Cystic fibrosis transmembrane regulator
CM	Contact mode
CV	Cyclic voltammetry/voltammogram
CVD	Chemical vapor deposition
DC	Direct current
EBID	Electron beam induced deposition
EDP(s)	Electrodeposition paint(s)
EDX	Energy dispersive X-ray spectroscopy
FIB	Focused ion beam
FPP	Four-point probe
FWHM	Full width at half maximum
GC	Generation-collection

GDH	Glucose dehydrogenase
GOx	Glucose oxidase
HEX	Hexokinase
HOPG	Highly-oriented pyrolytic graphite
IBID	Ion beam induced deposition
NSOM	Near field scanning optical microscopy/microscope
PBS	Phosphate buffered saline
PECVD	Plasma-enhanced CVD
PFE	Pentafluoroethane (CF_3CHF_2)
PTFE	Polytetrafluoroethylene
PtC	Platinum carbon
RE	Reference electrode
RF	Radio frequency
SCE	Saturated calomel electrode
SECM	Scanning electrochemical microscopy/microscope
SEM	Scanning electron microscopy/microscope
SG/TC	Sample generation/tip collection
SHE	Standard hydrogen electrode
SPM	Scanning probe microscopy
STM	Scanning tunneling microscopy/microscope
TEM	Transmission electron microscopy/microscope
TG/SC	Tip generation/sample collection
UME(s)	Ultramicroelectrodes(s)

UV	Ultraviolet
WE	Working electrode

SUMMARY

Combined atomic force microscopy-scanning electrochemical microscopy (AFM-SECM) is a powerful emerging technology capable of providing simultaneous topographical and electrochemical imaging at the sample surface. Specifically, AFM-SECM based on tip-integrated electrodes that are recessed from the apex of the AFM tip provides miniaturized electrodes that can be positioned at a constant distance to the sample surface. Surface modification of the tip-integrated electrode area (e.g., with biosensors) further enhances the versatility of such bifunctional probes. The integration of amperometric biosensors into AFM-SECM probes facilitates obtaining enhanced information during measurements of relevant molecular processes at live biological specimen. Of particular interest to this work was the detection of adenosine triphosphate (ATP) at a cellular level, as ATP is involved in many biologically relevant processes. However, there are several challenges concerning the integration of biosensors into bifunctional AFM-SECM probes. This thesis focuses on addressing and advancing several of these limitations.

The first part of the thesis describes novel thin film insulation materials for combined AFM-SECM probes. Insulation materials for microelectrochemical experiments are of crucial importance, since they need to be temporally stable, pinhole free, and sufficiently thin. The latter aspect is of particular importance for AFM-SECM based applications to decrease possible interactions of the probes during scanning of sample surfaces with the sample topology along with improved SECM performance. Plasma-polymerization is introduced as an attractive alternative to current state-of-the-art insulation techniques.

Insulation layers with a thickness of < 300 nm were found to exhibit excellent insulating properties and satisfying temporal stability for successful application in AFM-SECM approach/imaging experiments.

The second focus of this work was the implementation of novel approaches for increasing the AFM tip-integrated electrode area. Particularly in conjunction with biosensing experiments, the electrode areas in conventionally focused ion beam (FIB) fabricated AFM-SECM probes are too small for generating a detectable current response during scanning experiments. However, while increasing the tip-integrated electrode area, sufficient electrochemical resolution during the SECM experiment should be maintained. Ion beam induced deposition (IBID) was used to generate platinum carbon (PtC) composite materials at AFM-SECM probes, thereby successfully increasing the tip-integrated electrode area, as determined by cyclic voltammetry. Moreover, PtC materials fabricated via IBID were thoroughly characterized in terms of their physical and electrochemical properties. Studies at PtC-based ultramicroelectrodes (UMEs) revealed that the carbon fraction in the composite was inhibiting the charge transfer kinetics at the electrode surface for certain analytes. Therefore, several pre-treatment strategies were investigated including annealing, UV/ozone treatment, and post-deposition FIB milling. It was found that annealing lead to the desired electrode properties, as obtained from PtC UMEs, however, was of limited applicability to AFM cantilevers. FIB milling proved to be the most promising alternative treatment procedure improving charge transfer properties at the electrode along with fabrication compatibility at AFM-SECM probes.

The third part of this thesis aimed at providing fundamental studies on AFM-SECM application at live epithelial cell monolayers. Due to the soft and dynamic nature of the

samples along with the variability of the cell surface, thorough characterization of the cell surface was mandatory prior to AFM-SECM experiments. Therefore, AFM was used in different imaging modes to characterize the surface structures of epithelial cells. It was found that epithelial cell monolayers are amenable to extended AFM imaging; however, the force applied to the sample surfaces has to be carefully optimized, which was accentuated by results obtained during AFM-SECM based feedback mode experiments. Prior to the incorporation of ATP biosensors into batch-fabricated AFM-SECM probes, SECM-based experiments were performed, and have confirmed the presence of ATP at the surface of live epithelial cell monolayers. Moreover, imaging experiments conducted by AFM-SECM have enabled laterally resolved detection of ATP at live epithelial cell monolayers for the first time. Additionally, PtC composite materials introduced in the second part of this thesis were evaluated for applicability as transducer platforms for enzymatic biosensors. It was shown that pristine PtC did not exhibit adequate charge transfer characteristics for the electrooxidation of H_2O_2, whereas post-treated composites revealed strongly increased oxidation currents approaching the behavior of pure platinum electrodes. Glucose biosensors were deposited at PtC-based UMEs, and satisfying sensitivities and saturation currents were observed. The response time at this point was insufficient for imaging applications consequently further improvement of the biosensor immobilization procedure at PtC materials is required. It is anticipated that combination of all advancements obtained throughout this thesis along with an enhanced immobilization procedure will lead to optimized and miniaturized tip-integrated ATP biosensors for the localized detection of ATP at the surface of live epithelial cell monolayers.

1 INTRODUCTION

1.1 Thesis objective

The aim of this thesis was the advancement of combined atomic force microscopy-scanning electrochemical microscopy (AFM-SECM) probes toward biosensing platforms for life science applications. Besides improvement of current fabrication procedures, a novel insulation material for tip-integrated electrodes was implemented. Based on the requirements of the targeted application, a novel electrode material was integrated into AFM-SECM probes next to a thorough physical and electrochemical characterization. Finally, characterization of live epithelial cell monolayers with atomic force microscopy and application of miniaturized adenosine triphosphate (ATP) biosensors was performed.

1.2 Original contributions of this thesis

- Application of plasma-polymerized membranes as insulation layers for AFM-SECM probes and ultramicroelectrodes (UMEs), and their characterization (*Chapter 3*).

- Characterization of ion beam induced deposition (IBID) of platinum carbon (PtC) composites as electrode materials, and evaluation of strategies to improve electron transfer characteristics (*Chapter 4*).

- AFM investigations of live epithelial cell monolayers and detection of ATP release by SECM and AFM-SECM based ATP biosensors (*Chapter 5*).

1.3 Motivation

Cellular systems are highly complex biological entities consisting of well known individual components. Biological processes require interaction of these components within single cells, and cell communication with the extracellular environment. Intercellular communication mostly leads to the secretion of chemical agents into the extracellular environment that can influence both secreting and surrounding cells (*Figure 1.1*). Diseases often alter these chemical communication events, and consequently induce changes of cell signaling pathways. Distinguishing diseased from healthy conditions requires a thorough understanding of these processes.

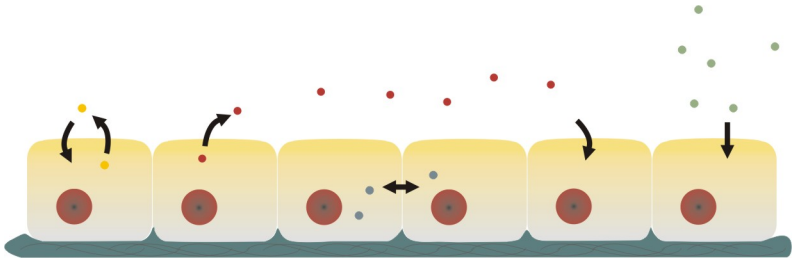

Figure 1.1. Schematic of cellular communication pathways.

Molecular processes at the cellular level are frequently investigated by analytical techniques providing bulk information during sequential data acquisition. Current state-of-the-art techniques for analyzing biological systems include invasive methods such as liquid chromatography, gel electrophoresis, X-ray crystallography, mass spectrometry or spectrophotometry, and non/semi-invasive methods such as different types of microscopy (optical, fluorescence, confocal or scanning probe microscopy) or patch clamp recordings[1]. Miniaturized sensors were identified as promising devices for real-time

monitoring of biological signals related to therapy of cardiovascular, pulmonary and hematologic diseases[2], along with direct measurements of neurotransmitter release[3]. Thus, a general goal in bioanalytics is to establish techniques for monitoring (investigating) biological systems at the cellular level that may provide localized real time sensing of analytes at the surface of live biological specimen, while simultaneously imaging the sample to correlate signaling events with e.g., topographical features/changes. There are several challenges involved with this approach. Miniaturized sensors have to be positioned accurately at the surface of the specimen. Usually, secreted chemicals are present at low concentrations in complex and frequently changing matrices implying that high selectivity and sensitivity of the analytical method is mandatory. Ideally, the dynamics of complex biological entities should be accounted for by temporal and spatial correlation of multiple parameters.

The presented contribution to this challenging field is based on the combination of AFM-SECM technology with integrated amperometric biosensors. Combining atomic force microscopy (AFM) and scanning electrochemical microscopy (SECM) is facilitated by integration of electrodes into AFM probes, and has been an emerging field for almost a decade[4, 5]. Specifically, AFM-SECM probe designs that enable modification of the electrode surface comprise electrodes recessed from the apex of the AFM tip[5]. Using the AFM tip as a spacer for the recessed electrode, they can be positioned at a constant distance from the sample surface; due to the close distance and given their geometric dimensions, improved resolution of the electrochemical measurement can be achieved. Furthermore, complementary topographical and electrochemical information is obtained enabling localization of analytes. Many biological relevant analytes such as cholesterol,

glutamate, ATP, glucose etc., cannot be directly detected as electrochemical products might foul the electrode or their oxidation potentials are unfavorably high. However, electrochemical biosensors enable specific detection of an analyte using a biological recognition element in combination with an electrochemical transducer[6]. Miniaturized biosensors have attracted considerable attention within recent years and immobilization schemes for miniaturized sensors can be adapted to be integrated in AFM-SECM probes. Among biological relevant analytes, ATP (*Figure 1.2*) plays a fundamental role.

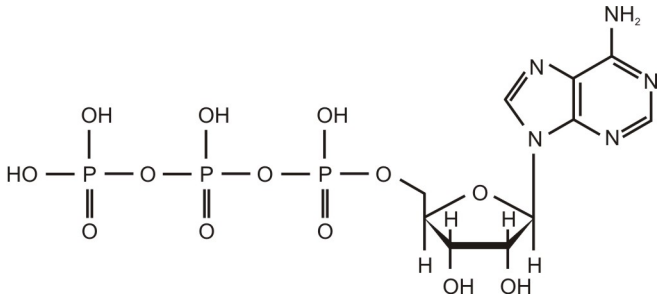

Figure 1.2. Structure of adenosine triphosphate.

Localized determination of ATP at a cellular level is of significant importance: ATP is an energy source for countless metabolic and enzymatic reactions within biological systems. Besides acting as the main intracellular energy source, ATP can be released from cells in response to specific stimuli, after which ATP acts as a transmitter or messenger molecule. Extracellular ATP alters cellular activity by interacting with ATP receptor molecules in the surface membrane of target cells. The receptors for ATP (a purine derivative) are called type 2 purinergic or P2 receptors to distinguish them from the type 1 receptors that recognize adenosine. P2 receptors fall into two major categories: P2X and P2Y receptors[7]. The 7 members of the P2X receptor family are ATP-gated ion channels,

signaling by changing the membrane potential of cells[8]. The 14 members of the P2Y receptor family are metabotropic receptors that signal by altering enzymatic activity within cells, usually by changing intracellular concentrations of cyclic adenosine monophosphate (cAMP) or inositol phospholipids[9]. P2 receptors are found ubiquitously in tissues, and the role of ATP as a signaling molecule is well characterized in sensory transduction in the nervous system[10-12], as a mediator in the immune system[13], and in regulating contractility in the gut[14]. ATP has also been suggested as a regulator of excitatory responses from the carotid body[15, 16] and as a regulator of lung fluid balance[17].

ATP is synthesized inside of cells mainly as the end product of the Krebs cycle in mitochondria. Steady-state cytosolic ATP concentrations are typically in the range of 3 - 10 mM, whereas steady-state concentrations in the extracellular environment are approx. 10 nM under basal conditions[18]. Thus there is a considerable concentration gradient for ATP secretion enabling diffusion into the extracellular environment through activated cellular release pathways.

ATP acts as a signaling molecule upon secretion into the extracellular environment by interaction with P2 receptors on cells adjacent to the site of release. Since the concentration of ATP necessary to activate P2 receptors is typically 1 to 10 μM, very little ATP needs to be released from cells to activate the receptors; thus ATP-based signaling does not interfere with intracellular metabolic/enzymatic reactions[18]. Extracellular ATP is rapidly degraded by ecto-enzymes, which may be secreted from cells or bound to cellular membranes, such as ecto-apyrases or ecto-ATPases[18]. Thus, similar to other transmitter substances, a steady-state balance between the rate of ATP release/receptor binding and the rate of ATP degradation is maintained. ATP is generally

classified as a local mediator. If ATP release slows, extracellular ATP can be rapidly degraded thus returning the cell to quiescent, unstimulated state.

ATP has been implicated in the molecular mechanisms of cystic fibrosis (CF). CF is one of the most common genetic diseases in the Caucasian population affecting approximately 1 in 3300 births[19]. CF results in an altered Cl^- transport through cellular membranes of epithelial cells lining secretory epithelia including the interior surface of the lungs. CF is caused by mutation of a gene, which encodes a membrane protein, the cystic fibrosis transmembrane regulator (CFTR)[20]. Lung epithelia are covered with a thin layer of liquid at a thickness of 7 μm, which is the approximate length of respiratory cilia[21]. Among other species such as Na^+, Cl^- and water, ATP is present in this liquid layer, due to a constant ATP release from the epithelium resulting from breathing-induced physical forces such as mechanical deformation or liquid shear stress[22-25]. Under steady breathing the amount of released ATP is constant, thus ATP concentration depends on the volume of the adjacent liquid layer. A specific ATP receptor subtype, the $P2Y_2$ receptor, has been identified as a crucial receptor in respiratory epithelium[26]. ATP binding to the $P2Y_2$ receptor inhibits Na^+ transporting channels. Since Na^+ transport is coupled to CFTR-mediated Cl^- transport and salt transport determines water transport, ATP-mediated inhibition is a mechanism to regulate the liquid level on the surface of the lung[27]. When CFTR activity is eliminated in CF, ATP release is reduced allowing Na^+ activity to increase. Hyperabsorption of Na^+ decreases the surface liquid volume, which interferes with ciliary movement and mucus removal[28]. So far the connection between altered Cl^- transport induced through the genetic defect and reduced ATP levels is not well understood. Dynamic studies providing localization and time-dependent

determination of ATP concentration changes could provide insight into the molecular processes of CF and represent the main motivation for the studies within this thesis.

Due to this physiological relevance, detection and quantification of ATP has been a field of significant biomedical research. Several analytical approaches have been reported for the measurement of ATP achieving quantification of physiologically relevant ATP concentrations, including bioluminescence[29, 30], chemiluminescence[31, 32], fluorescence[33, 34], or liquid chromatography[35, 36]. However, in many cases these techniques are either invasive or destructive and are often bulk measurement techniques.

Amperometric ATP biosensors are an interesting alternative to these concepts. Our research group has previously demonstrated ATP biosensors based on the immobilization of a competitive dual enzyme assay in electrodeposition paint (EDP) matrices[37]; these sensors have been applied for imaging ATP transport through artificial membranes, and stimulated extracellular ATP release from rat carotid bodies[38, 39]. Based on this concept, further miniaturization and incorporation of such ATP biosensors into combined AFM-SECM probes is anticipated.

However, further miniaturization of amperometric ATP biosensors is challenging, since current levels recorded are in the low pA range already for UMEs with a diameter of 25 µm[39]. Hence implementing the ATP sensing scheme at AFM tip-integrated electrodes, and measurements at live biological systems are challenging. New strategies have to be pursued to ensure reliable routine ATP measurements at live cell samples.

The present thesis focuses on addressing fundamental changes of AFM-SECM probes as transducers for imaging biosensor platforms, and other key considerations required for improved AFM-SECM performance. One important aspect is the insulation layer of the

AFM-SECM probe; besides being uniform, pinhole-free, and long-term stable, a reduced thickness of the insulation layer plays an important role for example to avoid interaction with the sample surface during AFM imaging. Hence, an important aim of this work was the development and evaluation of alternative insulation strategies for combined AFM-SECM probes. A second crucial parameter is the dimension of the electroactive area. Although small electrode dimensions are generally desired for high electrochemical resolution, in the context of tip-integrated amperometric biosensors increased electrode areas are required, since more enzymes can be immobilized. Ideally, an increase in electroactive area should be obtained, while maximizing the electrochemical resolution during imaging. Hence, the second aim of this work revolved around increasing the tip-integrated electrode area. Finally, with the overall goal of measuring localized ATP levels in an imaging mode at live epithelial cell samples, AFM imaging for biostructural analysis has to be optimized.

1.4 Structure of this thesis

Based on the requirements for improved AFM-SECM performance at biological systems, the present thesis is structured as follows:

Chapter 2 describes the background of the electrochemical concepts relevant to this work. Additionally, it introduces scanning probe microcopy, and - more specifically - atomic force microscopy and scanning electrochemical microscopy along with the combination of these techniques.

Chapter 3 discusses plasma-polymerized membranes as novel insulation layers for combined AFM-SECM probes and UMEs.

Chapter 4 introduces ion beam induced deposition of PtC composite materials, and their characterization with respect to their physical and electrochemical properties. Furthermore, electron transfer rates are determined, and concepts are discussed that improve the charge transfer at these novel electrode materials.

Chapter 5 describes topographical AFM studies at live epithelial cell monolayers. Furthermore, ATP biosensing at live epithelial cells is demonstrated for the first time based on non-invasive SECM experiments, and combined AFM-SECM experiments providing localization of ATP at the cell surface. Finally, the applicability of PtC composites (***Chapter 4***) as transducer for enzymatic biosensors is evaluated.

Chapter 6 provides concluding remarks, and an outlook for future work.

1.5 References

(1) Karp, G. *Cell and Molecular Biology: Concepts and Experiments*, 3rd ed.; John Wiley & Sons, Inc.: New York, 2002.

(2) Buxton Denis, B.; Lee Stephen, C.; Wickline Samuel, A.; Ferrari, M. *Recommendations of the National Heart, Lung, and Blood Institute Nanotechnology Working Group*, Circulation **2003**, *108*, 2737-2742.

(3) Dale, N.; Hatz, S.; Tian, F.; Llaudet, E. *Listening to the brain: microelectrode biosensors for neurochemicals*, Trends Biotechnol. **2005**, *23*, 420-428.

(4) Macpherson, J. V.; Unwin, P. R. *Combined Scanning Electrochemical-Atomic Force Microscopy*, Anal. Chem. **2000**, *72*, 276-285.

(5) Kranz, C.; Friedbacher, G.; Mizaikoff, B.; Lugstein, A.; Smoliner, J.; Bertagnolli, E. *Integrating an Ultramicroelectrode in an AFM Cantilever: Combined Technology for Enhanced Information*, Anal. Chem. **2001**, *73*, 2491-2500.

(6) Thevenot, D. R.; Toth, K.; Durst, R. A.; Wilson, G. S. *Electrochemical biosensors: recommended definitions and classification*, Pure Appl. Chem. **1999**, *71*, 2333-2348.

(7) Burnstock, G.; Kennedy, C. *Is there a basis for distinguishing two types of P2-purinoceptor?*, Gen. Pharmacol. **1985**, *16*, 433-440.

(8) North, R. A. *Molecular physiology of P2X receptors*, Physiological Reviews **2002**, *82*, 1013-1067.

(9) von Kuegelgen, I. *Pharmacological profiles of cloned mammalian P2Y-receptor subtypes*, Pharmacol. Ther. **2006**, *110*, 415-432.

(10) Cook, S. P.; Vulchanova, L.; Hargreaves, K. M.; Elde, R.; McCleskey, E. W. *Distinct ATP receptors on pain-sensing and stretch-sensing neurons*, Nature **1997**, *387*, 505-508.

(11) Cockayne, D. A.; Hamilton, S. G.; Zhu, Q.-M.; Dunn, P. M.; Zhong, Y.; Novakovic, S.; Malmberg, A. B.; Cain, G.; Berson, A.; Kassotakls, L.; Hedley, L.; Lachnlt, W. G.; Burnstock, G.; McMahon, S. B.; Ford, A. P. D. W. *Urinary bladder hyporeflexia and reduced pain-related behaviour in P2X3-deficient mice*, Nature **2000**, *407*, 1011-1015.

(12) Souslova, V.; Cesare, P.; Ding, Y.; Akoplan, A. N.; Stanfa, L.; Suzuki, R.; Carpenter, K.; Dickenson, A.; Boyce, S.; Hill, R.; Nebenius-Oosthuizen, D.; Smith, A. J. H.; Kidd, E. J.; Wood, J. N. *Warm-coding deficits and aberrant inflammatory pain in mice lacking P2X3 receptors*, Nature **2000**, *407*, 1015-1017.

(13) Idzko, M.; Hammad, H.; van Nimwegen, M.; Kool, M.; Willart, M. A. M.; Muskens, F.; Hoogsteden, H. C.; Luttmann, W.; Ferrari, D.; Di Virgilio, F.; Virchow, J. C., Jr.; Lambrecht, B. N. *Extracellular ATP triggers and maintains asthmatic airway inflammation by activating dendritic cells*, Nat. Med. **2007**, *13*, 913-919.

(14) Burnstock, G. *Pathophysiology and therapeutic potential of purinergic signaling*, Pharmacol. Rev. **2006**, *58*, 58-86.

(15) Buttigieg, J.; Nurse, C. A. *Detection of hypoxia-evoked ATP release from chemoreceptor cells of the rat carotid body*, Biochem. Biophys. Res. Commun. **2004**, *322*, 82-87.

(16) Rong, W.; Gourine, A. V.; Cockayne, D. A.; Xiang, Z.; Ford, A. P. D. W.; Spyer, K. M.; Burnstock, G. *Pivotal role of nucleotide P2X2 receptor subunit of the ATP-gated ion channel mediating ventilatory responses to hypoxia*, J. Neurosci. **2003**, *23*, 11315-11321.

(17) Button, B.; Boucher Richard, C. *Role of mechanical stress in regulating airway surface hydration and mucus clearance rates*, Respir. Physiol. Neurobiol. **2008**, *163*, 189-201.

(18) Schwiebert, E. M.; Zsembery, A. *Extracellular ATP as a signaling molecule for epithelial cells*, Biochim. Biophys. Acta **2003**, *1615*, 7-32.

(19) Anonymous *Genetic testing for cystic fibrosis*, NIH consensus statement **1997**, *15*, 1-37.

(20) Riordan, J. R.; Rommens, J. M.; Kerem, B. S.; Alon, N.; Rozmahel, R.; Grzelczak, Z.; Zielenski, J.; Lok, S.; Plavsic, N.; et al. *Identification of the cystic fibrosis gene: cloning and characterization of complementary DNA*, Science **1989**, *245*, 1066-1073.

(21) Schwiebert, E. M. *Extracellular autocrine nucleotide signalling in a microenvironment: integrative physiology in a minute volume of airway surface liquid*, J. Physiol. **2007**, *580*, 359-360.

(22) Grygorczyk, R.; Hanrahan, J. W. *CFTR-independent ATP release from epithelial cells triggered by mechanical stimuli*, Am. J. Physiol. **1997**, *272*, C1058-C1066.

(23) Homolya, L.; Steinberg, T. H.; Boucher, R. C. *Cell to cell communication in response to mechanical stress via bilateral release of ATP and UTP in polarized epithelia*, J. Cell Biol. **2000**, *150*, 1349-1359.

(24) Guyot, A.; Hanrahan, J. W. *ATP release from human airway epithelial cells studied using a capillary cell culture system*, J. Physiol. **2002**, *545*, 199-206.

(25) Tarran, R.; Button, B.; Picher, M.; Paradiso, A. M.; Ribeiro, C. M.; Lazarowski, E. R.; Zhang, L.; Collins, P. L.; Pickles, R. J.; Fredberg, J. J.; Boucher, R. C. *Normal and Cystic Fibrosis Airway Surface Liquid Homeostasis: the effects of phasic shear stress and viral infections*, J. Biol. Chem. **2005**, *280*, 35751-35759.

(26) Cressman, V. L.; Lazarowski, E.; Homolya, L.; Boucher, R. C.; Koller, B. H.; Grubb, B. R. *Effect of loss of P2Y2 receptor gene expression on nucleotide regulation of murine epithelial Cl- transport*, J. Biol. Chem. **1999**, *274*, 26461-26468.

(27) Eaton, D. C.; Helms, M. N.; Koval, M.; Bao, H. F.; Jain, L. *The contribution of epithelial sodium channels to alveolar function in health and disease*, Annu. Rev. Physiol. **2009**, *71*, 403-423.

(28) Clunes, M. T.; Boucher Richard, C. *Cystic fibrosis: the mechanisms of pathogenesis of an inherited lung disorder*, Drug Discovery Today: Disease Mechanisms **2007**, *4*, 63-72.

(29) Gamborg, G.; Hansen, E. H. *Flow-injection bioluminescent determination of ATP based on the use of the luciferin-luciferase system*, Anal. Chim. Acta **1994**, *285*, 321-328.

(30) Ishida, A.; Yoshikawa, T.; Nakazawa, T.; Kamidate, T. *Enhanced firefly bioluminescence assay of ATP in the presence of ATP extractants by using diethylaminoethyl-dextran*, Anal. Biochem. **2002**, *305*, 236-241.

(31) Edwards, J.; Sprung, R.; Spence, D.; Sprague, R. *Chemiluminescence detection of ATP release from red blood cells upon passage through microbore tubing*, Analyst **2001**, *126*, 1257-1260.

(32) Perez-Ruiz, T.; Martinez-Lozano, C.; Tomas, V.; Martin, J. *Determination of ATP via the photochemical generation of hydrogen peroxide using flow injection luminol chemiluminescence detection*, Anal. Bioanal. Chem. **2003**, *377*, 189-194.

(33) Foy, G. P.; Pacey, G. E. *Determination of ATP using chelation-enhanced fluorescence*, Talanta **1996**, *43*, 225-232.

(34) Hou, F.; Wang, X.; Jiang, C. *Determination of ATP as a fluorescence probe with europium(III)-doxycycline*, Anal. Sci. **2005**, *21*, 231-234.

(35) Deng, Q.; Kauri, L. M.; Qian, W.-J.; Dahlgren, G. M.; Kennedy, R. T. *Microscale determination of purines in tissue samples by capillary liquid chromatography with electrochemical detection*, Analyst **2003**, *128*, 1013-1018.

(36) Bao, Y.; Everaert, J.; Pietraszkiewicz, M.; Pietraszkiewicz, O.; Bohets, H.; Geise, H. J.; Peng, B. X.; Nagels, L. J. *Behaviour of nucleotides and oligonucleotides in potentiometric HPLC detection*, Anal. Chim. Acta **2005**, *550*, 130-136.

(37) Kueng, A.; Kranz, C.; Mizaikoff, B. *Amperometric ATP biosensor based on polymer entrapped enzymes*, Biosens. Bioelectron. **2004**, *19*, 1301-1307.

(38) Kueng, A.; Kranz, C.; Mizaikoff, B. *Imaging of ATP membrane transport with dual micro-disk electrodes and scanning electrochemical microscopy*, Biosens. Bioelectron. **2005**, *21*, 346-353.

(39) Masson, J.-F.; Kranz, C.; Mizaikoff, B.; Gauda, E. B. *Amperometric ATP microbiosensors for the analysis of chemosensitivity at rat carotid bodies*, Anal. Chem. **2008**, *80*, 3991-3998.

2 BACKGROUND

This chapter introduces the electrochemical concepts relevant to this work including cyclic voltammetry, ultramicroelectrodes, and amperometric biosensors. Atomic force microscopy, scanning electrochemical microscopy, and combined atomic force microscopy-scanning electrochemical microscopy are also discussed.

2.1 Electrochemical concepts

2.1.1 Cyclic voltammetry (CV)

Cyclic voltammetry is a very versatile electroanalytical technique that has been applied to a variety of investigations including evaluation of electron transfer kinetics and elucidation of transfer mechanisms[1], characterization of materials (e.g. catalyst surfaces[2], conducting polymers[3]), and biomedical research (*in-vivo* monitoring of dopamine release in the brain[4]). During a CV experiment, the potential applied to the working electrode is varied with a linear potential sweep starting from an initial potential value (E_i) to a switching potential (E_λ), where the sweep direction is reversed and returned to the initial value (*Figure 2.1A*). The scan rate v of the potential sweep is an important parameter, since it determines the time scale of the experiment[1]. The resulting current is plotted against the applied potential. *Figure 2.1B* shows a CV for a one-electron transfer reaction defined by the following reaction

$$O + e^- \underset{k_b}{\overset{k_f}{\rightleftharpoons}} R, \tag{2.1}$$

where O is the oxidized form of the involved redox species, R is the reduced form, and k_f and k_b are the forward and the backward rate constants, respectively.

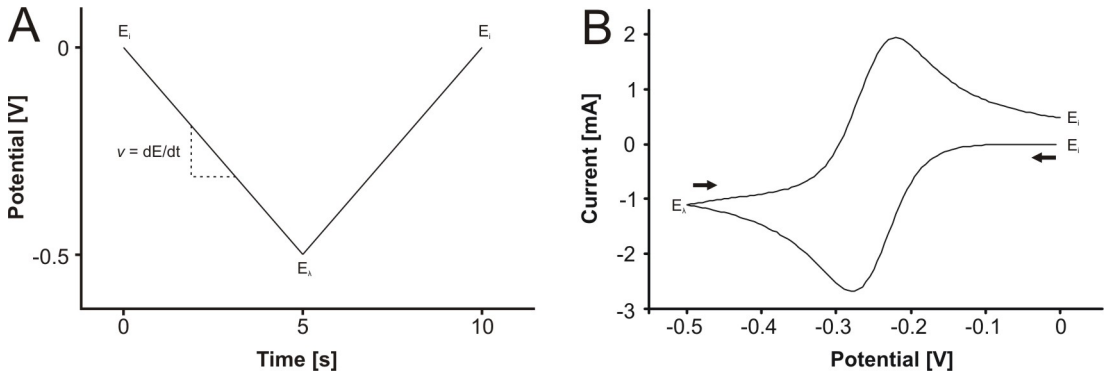

Figure 2.1. (A) Shape of the potential waveform applied during a CV scan. (B) Simulated CV for a reversible reaction at a macroscopic electrode. DigiElch simulation software was used[5].

The shape of the CV is determined by two processes, heterogeneous charge transfer at the interface, and diffusional mass transport. The heterogeneous charge transfer at the interface is described by *Equation (2.2)*[1]

$$i = nFA\left(C_O(0,t)k^o \exp\left[\frac{-\alpha nF(E-E^0)}{RT}\right] - C_R(0,t)k^0 \exp\left[\frac{(1-\alpha)nF(E-E^0)}{RT}\right]\right), \tag{2.2}$$

where n is the number of electrons transferred in the electrode reaction, F is the Faraday constant, A is the electrode area, $C_{O/R}(0,t)$ are the surface concentrations of O or R at time

t, k^0 is the standard heterogeneous rate constant, α is the transfer coefficient, E is the applied potential, E^0 is the standard potential, R is the gas constant, and T is the absolute temperature.

Generally, mass transport may proceed as a result of three effects: convection, migration, and diffusion. However, only diffusional mass transport effects are considered in typical CV theory, since convection may be avoided in unstirred solutions, and migration may be suppressed by addition of an excess of supporting electrolyte. Electrode surface concentrations of the reactive species are dependent upon the applied potential and differ from the bulk concentrations during the electrochemical experiment. Diffusion controlled mass transport occurs via the concentration gradient. Fick's second law of diffusion describes the time-dependent change of the diffusion field, and as a result, the time-dependent current observed at the electrode can be derived as follows[6]

$$i = nFAD_O\left(\frac{\partial C_O(x,t)}{\partial x}\right)_{x=o}, \tag{2.3}$$

where D_O is the diffusion coefficient of O, $\frac{\partial C_O(x,t)}{\partial x}$ is the concentration gradient in distance x at time t, and other parameters are as defined previously. Note that this relationship is only defined for planar diffusion. Solving *Equation (2.3)* leads to the Cottrell equation[7]

$$i = \frac{nFAD_O^{0.5} C_O^{*}}{\pi^{0.5} t^{0.5}}, \tag{2.4}$$

where C_O^* is the bulk concentration of O, while other parameters are defined as before. From *Equations (2.2)* and *(2.3)* it is evident that there are two components contributing to the current measured at the electrode, the heterogeneous charge transfer at the interface, and diffusion. However, depending on the rate of the heterogeneous charge transfer one of the two components can prevail. In case the charge transfer proceeds fast ($k^0 > 10^{-1}$ cm s^{-1}, reversible case), the current measured is limited by mass transport (diffusion controlled process). For this case *Equation (2.2)* reduces to the Nernst equation, and the surface concentrations are dependent on the applied potential. The other boundary is represented by the irreversible case ($k^0 < 10^{-5}$ cm s^{-1}), where the heterogeneous charge transfer is the rate limiting step determining the measured current. Quasi-reversible reactions are in between these two cases (approx. 10^{-1} cm $s^{-1} > k^0 > 10^{-5}$ cm s^{-1}), and are consequently controlled by both the mass transport and the heterogeneous charge transfer[1].

It should also be mentioned that the total current observed in the CV is a sum of the faradaic current resulting from the charge transfer at the interface, and the charging current resulting from the charging of the electrochemical double layer. The charging current will be described in more detail in the next section.

2.1.2 Ultramicroelectrodes

Ultramicroelectrodes are defined as electrodes that have at least one dimension smaller than 25 μm, also called the critical dimension[6]. The small dimensions of UMEs strongly

influence the mass transport characteristics resulting in a series of advantageous properties.

As already indicated earlier, the Cottrell equation is only defined for planar diffusion observed at macroscopic electrodes. During planar diffusion, mass transport occurs perpendicularly to the electrode surface, and may be mathematically described as one-dimensional diffusion (*Figure 2.2A*). Despite diffusion at electrode edges deviating from planarity, edge effects are negligible at large electrode surfaces. At small electrode surfaces (i.e. UMEs), contributions from mass transport parallel to the electrode surface (i.e. electrode edges) are not negligible anymore, and have to be considered.

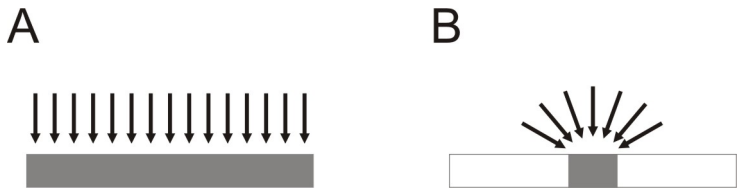

Figure 2.2. Schematic representation of planar (A) and hemispherical (B) diffusion.

In this case, diffusion is referred to as hemispherical diffusion (for a disk electrode), and is mathematically described by two-dimensional diffusion processes (*Figure 2.2B*). Solving the diffusion equation leads to a modified Cottrell equation with a second term as follows[8]

$$i = \frac{nFAD_O^{0.5}C_O^*}{\pi^{0.5}t^{0.5}} + b\frac{nFAD_OC_O^*}{\pi^{0.5}r}, \qquad (2.5)$$

where *b* is a prefactor that is influenced by the transition from the planar to the hemispherical diffusion field, and *r* is the radius of the electrode. Depending on the time scale of the experiment, either the first or the second term of the equation dominates. The first term is equivalent to the unmodified Cottrell equation dominating at short time scales. At longer time scales, the second term dominates and a steady-state current may be observed. Due to hemispherical diffusion towards the electrode surface, smaller electrodes need a shorter time to reach the steady-state. Zoski et al. calculated the time required to reach steady-state currents at disk electrodes with different electrode radii[9]. The authors concluded that at the assumed diffusion coefficient (10^{-9} m^2 s^{-1}) disks with radii of 5 µm and 0.5 µm required 1.3 s and 0.01 s, respectively, to reach steady-state. At macroelectrodes, this time is in the range of hours[8]. Given the small surface area, high current densities are observed during hemispherical diffusion.

As indicated earlier, the shape of a CV depends on the diffusional mass transport. Hemispherical diffusion leads to a sigmoidal shape of the CV. The time scale of the experiment can be directly influenced by the scan rate. Hence, at fast scan rates planar diffusion is observed, whereas at slow scan rates hemispherical diffusion dominates. This effect is visualized in *Figure 2.3A*. Similarly, decreasing the electrode radius at a constant scan rate increases the contribution of hemispherical diffusion (*Figure 2.3B*).

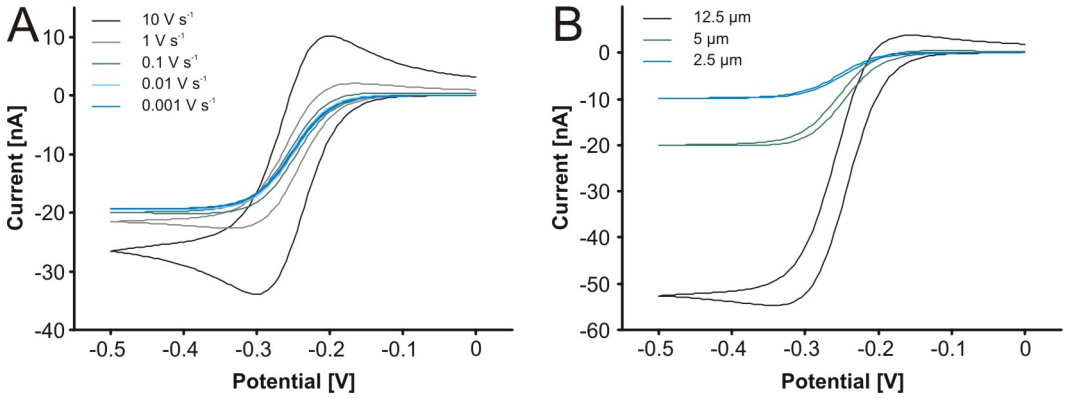

Figure 2.3. Simulated CVs demonstrating the influence of scan rate (A) and electrode radius (B) on the obtained CV. DigiElch simulation software was used[5]. For CVs shown in (A) the electrode radius was kept constant at 5 µm, and in (B) the scan rate was maintained at 0.1 V s^{-1}.

Steady-state currents can be calculated for different UME shapes[8], and may be applied to determine electrode radii, analyte concentrations or diffusion coefficients. The steady-state currents for the two shapes relevant to this work, the disk UME (*Equation (2.6)*)[10] and the ring UME (*Equation (2.7)*)[11, 12], are

$$i_{disk} = 4nFDC^{*}r, \tag{2.6}$$

$$i_{ring} = nFDC^{*}l_0, \tag{2.7}$$

$$\text{with } l_0 = \frac{\pi^2(a+b)}{\ln\left[16\frac{(a+b)}{(b-a)}\right]} \text{ for } \frac{a}{b} > 0.91, \tag{2.8}$$

$$\text{or } l_0 = \frac{\pi^2(a+b)}{\ln\left[\frac{32a}{(b-a)} + \exp\frac{\pi^2}{4}\right]} \text{ for } \frac{a}{b} < 0.91, \tag{2.9}$$

where a is the inner ring radius, and b is the outer ring radius. Other parameters were defined earlier.

Besides the fast onset of steady-state currents, another advantageous property of UMEs is the reduced charging current resulting from the charging of the electrical double layer. It is generally desired to minimize charging contributions, since they convolute with the faradaic current and may even mask faradaic currents. For a potential step experiment, the charging current exponentially decays with a time scale that depends on the size of the electrode. During CV, the constantly changing potential leads to two contributions for the charging current i_c[8]

$$i_c = \left[\left(\frac{E}{R_u} - vC_d\right)\exp\left(-\frac{t}{R_u C_d}\right)\right] + vC_d\,, \tag{2.10}$$

where R_u is the uncompensated solution resistance, and C_d is the double layer capacitance. The second (steady-state) term dominates at small radii over the first (transient) term simplifying the equation to

$$i_c = vC_d\,. \tag{2.11}$$

Thus, the charging current is directly proportional to C_d, which in turn is proportional to the surface area. However, since the faradaic current under steady-state conditions is proportional to the radius, a decreasing electrode radius improves the ratio of faradaic

current to charging current accordingly[13]. This implies that low analyte concentrations may be used and detected with reduced masking effects.

Also the ohmic drop in solution is reduced while using UMEs. Since the solution in an electrochemical experiment displays a finite resistance, current flow through the solution leads to a potential drop according to Ohm's law. As a result, the effective potential (E_{eff}) at the electrode is reduced by iR_u (ohmic drop) with respect to the applied potential (E)

$$E_{eff} = E - iR_u . \tag{2.12}$$

The uncompensated solution resistance R_u depends on several factors including the electrode radius r and the specific resistivity ρ of the solution for a disk microelectrode[13]

$$R_u = \frac{\rho}{4\pi r} . \tag{2.13}$$

Since charging currents are proportional to the electrode area, the induced ohmic drop decreases with decreasing electrode radius, which also holds for faradaic currents under planar diffusion. In the case of hemispherical diffusion, ohmic drop resulting from the faradaic current contribution becomes independent of the electrode radius. These small ohmic drops observed at UMEs enable measurements in highly resistive media[13].

The product of uncompensated solution resistance and double layer capacitance, R_uC_d, is defined as the cell time constant[6]. For disk-shaped UMEs, the cell time constant is directly proportional to the UME radius. Small cell time constants at UMEs were first

demonstrated by McCreery and co-workers[14], and allow applied potential to be adjusted at a very short time scale enabling fast scan CV, and thus, observations of labile species.

2.1.3 Amperometric biosensors

Since Clark and Lyons proposed the first biosensor in 1962 based on a thin layer of glucose oxidase (GOx) entrapped at an oxygen electrode via a semipermeable membrane[15], the biosensing field has significantly grown in both scientific and commercial interest[16, 17]. Although several types of biosensors have been commercialized[17], glucose detection accounts for the majority of the biosensing market[16, 18]. Biosensors are commonly referred to as a specialized subgroup of chemical sensors[19], which are defined as devices that convert chemical information, e.g. the concentration of a specific analyte, into an analytically useful signal[20]. Chemical sensors consist of at least two functional subunits, a recognition element and a transducer. If the recognition element utilizes a biological specimen (such as an enzyme), the device is termed a biosensor[19]. An advantage of biological recognition elements lies in their high molecular selectivity. Different types of transduction principles have been used in conjunction with biosensors including optical, thermal, piezoelectric, and electrochemical transduction[17]; however, due to the focus of this work this section will only cover amperometric biosensors and selected applications thereof.

As already indicated, glucose biosensors are a major field of interest. The main drive for these investigations is the need for diagnosis of blood glucose levels in the context of diabetes mellitus[18]. Amperometric glucose biosensors are mainly based on glucose oxidase, an enzyme which catalyzes the oxidation of glucose to gluconolactone. Glucose dehydrogenase (GDH) is also capable of oxidizing glucose, and has been proposed as an

alternative to GOx, but has found limited application in biosensors due to a limited stability[18]. Glucose biosensing has been of interest to the scientific community for several decades[18, 21, 22]. Hence, particularly GOx is a well characterized and useful model system, which may be applied to complex biosensing schemes involving multi-enzyme systems.

On the cellular level, ATP is an extremely important signaling molecule, as already discussed in *Chapter 1*. Direct electrochemical oxidation of adenosine is feasible at high positive potentials (1.3 V)[23], however it has been shown that oxidation products foul the electrode surface of most common electrode materials[24]. ATP biosensors have been previously applied to measure the release of ATP from spinal cord, brainstem, pigment epithelium, and carotid body preparations[25-29]. Amperometric detection of ATP cannot be achieved with a single enzyme, therefore ATP biosensing is commonly based on the immobilization of multiple enzymes[25, 30-36]. ATP biosensors based on triple enzyme systems, such as glucose-6-phosphate dehydrogenase, pyruvate kinase and hexokinase[30], or glucose-6-phosphate dehydrogenase, hexokinase and salicylate hydroxylase[31] have been reported. Alternatively, dual-enzyme systems have been implemented e.g. based on immobilization of glycerol kinase and glycerol-3-phosphate oxidase in a sol gel matrix[25, 32].

The biosensor used in this thesis is also based on a dual enzyme system, glucose oxidase and hexokinase (HEX)[33-36]. In this approach, GOx and HEX compete for the substrate glucose. During the competitive reaction H_2O_2 is formed as an enzymatic by-product and oxidized at the electrode. Reactions included in this detection scheme are the following

GOx: glucose + O_2 ➔ gluconolactone + H_2O_2 (2.14)

HEX: glucose + ATP ➔ glucose-6-phosphate + ADP (2.15)

UME: H_2O_2 ➔ $2H^+ + 2e^- + O_2$ (2.16)

2.2 Scanning probe microscopy (SPM)

With the invention of the scanning tunneling microscope (STM) in 1982, a new era started in the field of surface analytical techniques[37, 38]. Through this discovery, Binnig and Rohrer not only received the Nobel Prize in physics in 1986, but they also laid out the fundamentals for a family of techniques now grouped as scanning probe microscopies. All SPM techniques have in common that a probe is scanned in close proximity to a sample surface and a specific probe-sample interaction is monitored, which originates from physical/chemical interaction between probe and sample surface. Depending on the exact physical interaction monitored, SPM techniques may be categorized in different sub-groups. The two techniques applied in this work, and combinations thereof, will be described in the following sections.

2.2.1 Atomic force microscopy

Binnig also contributed to the invention of atomic force microscopy in 1986 shortly after the STM was introduced[39]. In atomic force microscopy, a sharp tip located on a soft cantilever arm is scanned across a sample surface in nm-sized increments utilizing piezoelectric positioning elements. Due to force interactions with the sample, the cantilever arm is deflected. If the cantilever deflection is kept at a constant value (constant force mode), information about the topography may be obtained. Different

attractive and repulsive forces contribute to the deflection of the cantilever (e.g. van der Waals forces, electrostatic forces, capillary forces, magnetic forces and interatomic forces), and - depending on the exact measuring conditions - certain forces dominate. The cantilever deflection is mainly monitored with an optical readout system[40]. A laser beam is reflected from the backside of the cantilever arm onto a photodiode, which is usually split into four segments. Consequently, cantilever deflection results in a corresponding movement of the laser spot on the split photodiode. A feedback mechanism then actuates the piezoelectric positioning elements to maintain the cantilever at a constant deflection/force.

There are a variety of different measuring modes in AFM including contact mode, non-contact mode, dynamic mode (frequency/amplitude-modulation), lateral force mode or magnetic force mode; only the modes relevant to this thesis will be introduced. During contact mode (CM) AFM, the tip is scanned while being in continuous contact with the sample surface[39, 41] (*Figure 2.4A*). In this mode, the main source of cantilever deflection arises from short-range repulsion forces resulting from overlapping orbitals of tip and sample atoms. In addition, other forces contribute to the cantilever deflection increasing the force in the contact area. Contact mode is often considered less suitable for investigating soft samples that may be damaged by continuous contact with the tip. Dynamic mode AFM techniques such as amplitude modulation (AM) AFM[42] reduce frictional forces at the sample surface due to the intermittent contact of the tip[43, 44]. Essentially, the cantilever is oscillated at a certain resonant frequency and amplitude damping as a result of repulsive tip-sample interaction is monitored (*Figure 2.4B*).

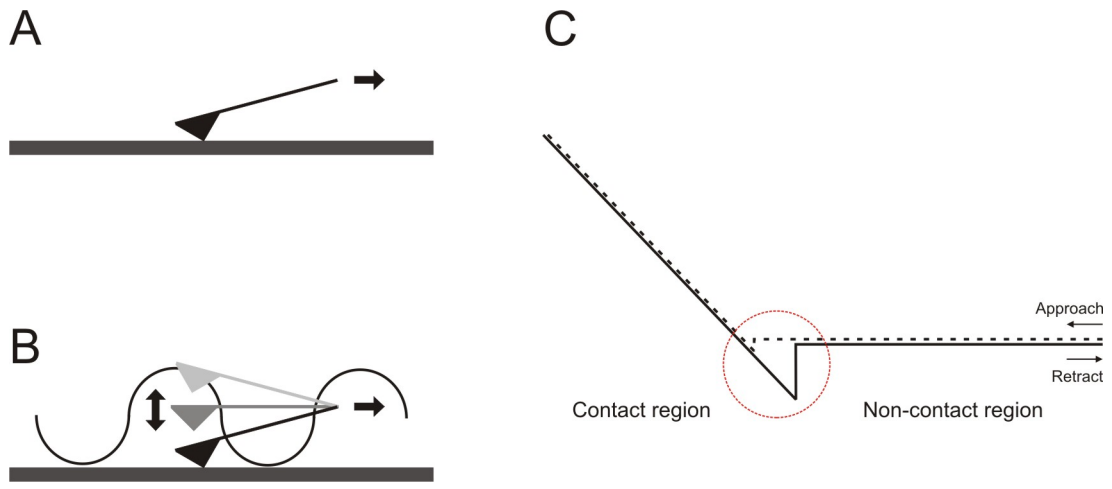

Figure 2.4. Schematic illustration of contact mode AFM (A) and dynamic mode AFM (B). Schematic of an idealized deflection-distance curve (C).

Force interactions between the tip and the sample, and other sample properties such as sample elasticity, may be monitored by recording deflection-distance curves. In this case, the deflection of the cantilever is monitored while the AFM probe is approached and retracted from the sample surface. *Figure 2.4C* shows a scheme of an idealized deflection-distance curve. No deflection is observed if the cantilever is far away from the surface (non-contact region), and correspondingly the cantilever deflects in the contact region. The slope of the curve in the contact region may provide valuable information about elastic properties of the sample. Besides, the area at the contact point between tip and sample (marked with red circle in *Figure 2.4C*) reveals important information about tip-sample forces while approaching and retracting the cantilever. In case AFM tips are chemically modified, specific molecular interaction forces may be monitored by force spectroscopy. Gaub and co-workers[45], as well as Colton and co-workers[46] pioneered this area by reporting single bond rupture events and deriving unbinding forces. Particularly from a bioscientific perspective, single molecule force spectroscopy has been extensively

applied[47-50]. Imaging with modified AFM probes enabling simultaneous detection of topography and biologically relevant rupture events was first accomplished by Hinterdorfer and co-workers[51, 52].

AFM imaging with unmodified probes has also been applied to study biological systems, since AFM displays the capability of imaging surface topography in physiological solutions. Researchers have extensively explored imaging capabilities of AFM in life sciences. For example, single proteins have been imaged and resolved with exceptional resolution revealing structures in the sub-nm range[53], in addition to investigations revolving around DNA condensation and DNA mapping[54-56]. High-speed AFM is an exciting technique used to visualize dynamic biomolecular processes[57]. Additionally, topography or topographical changes of fixed/life cells, viruses and microbes have been investigated by AFM[58-62].

2.2.2 Scanning electrochemical microscopy

The groups of Engstrom and Bard independently reported SECM for the first time in the late 1980's[63-65]. SECM takes advantage of several unique characteristics that are observed at UMEs such as reduced double-layer charging effects, reduced ohmic drop, and well-defined steady-state currents enabling the use of UMEs as scanning probes. In SECM, a biased UME is scanned in close proximity to a sample surface yielding information about electroactive processes and features of species/sample. The faradaic current measured at the UME is dependant on several factors including properties of the sample surface, UME-to-sample distance, and the critical dimension of the UME. Thus, signal generation in SECM is based on surface-induced changes of the faradaic current measured at the UME resulting from the diffusion of the electroactive species to the electrode surface

during scanning[66]. This enables *in-situ* investigations of (electro)chemical surface and interface properties. Different geometries such as disk, conical or ring-shaped UMEs[67-72] may be used in SECM experiments, however, typically disk-shaped geometries are preferred due to their well-defined electrochemical properties and quantitative mathematical description of the involved diffusion processes. Oftentimes UMEs used as scanning probes in SECM are called "tips" independent of the specific UME shape.

The two most important modes for SECM based imaging are the feedback mode[73], and the generation-collection (GC) mode[74]. During feedback mode SECM, one redox form of a quasi-reversible redox couple (R in *Figure 2.5*) is added to the solution and subsequently electrochemically converted at the biased electrode resulting in a faradaic current. The steady-state current, $i_{T\infty}$, recorded at a disk shaped UME in bulk solution is equal to the current obtained from *Equation (2.6)*.

If the UME is approached to the sample surface, the steady-state current changes in close proximity of the surface (within a few UME radii) depending on the surface properties. For conducting surfaces, an increase in current response is observed due to a recycling of the redox mediator at the sample surface leading to locally increased redox mediator concentrations within the UME-sample gap (positive feedback). A decrease in current (negative feedback) is obtained if the UME approaches an insulating surface due to localized depletion of redox mediator as diffusion from the solution bulk is partially blocked. *Figure 2.5* shows representative current-distance relationships (approach curves). These approach curves are typically used to position amperometric UMEs at a close distance to the sample surface based on comparison of experimentally obtained approach curves with theoretically derived curves[75]. Besides surface properties and

electrode dimensions, the RG value defined by *Equation (2.17)* is crucial to the faradaic current measured at close distance to the sample surface and SECM performance

$$RG = \frac{r_g}{r}, \tag{2.17}$$

where r_g is the radius of the insulating sheath, and r the radius of the active electrode surface. RG values in a range of 5 - 20 are mostly regarded as suitable[76], however, it has also been demonstrated that for RG values approaching unity steady-state currents observed at the UME are enhanced via diffusion of redox mediator from behind the plane[72].

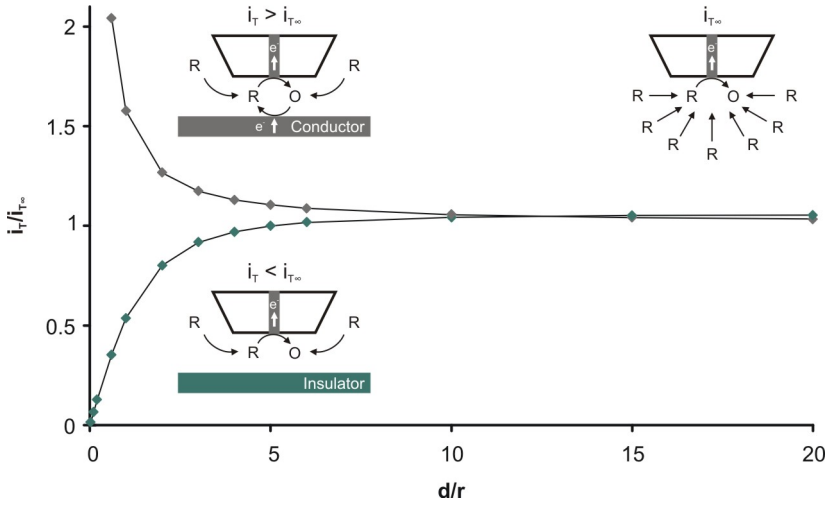

Figure 2.5. SECM approach curves for positive and negative feedback. The distance is normalized to the electrode radius and the steady-state current to the current recorded in bulk.

There are two basic possibilities for the GC mode: sample generation/tip collection (SG/TC) and tip generation/sample collection (TG/SC). Either the sample (SG/TC) or the

tip (TG/SC) is used to generate an electroactive species, which is subsequently collected (detected) at the tip (SG/TC) or the sample (TG/SC), respectively (*Figure 2.6*). An excellent example for the SG/TC mode was reported by Engstrom et al.[63]. The authors used a UME to detect concentration profiles induced by a macroscopic substrate electrode. The TG/SC mode was also demonstrated soon after the introduction of SECM[74] showing images of substrate electrodes acquired via both the tip current and the substrate current.

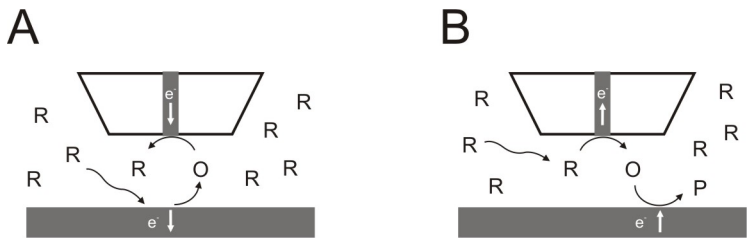

Figure 2.6. Schematic of SG/TC (A) and TG/SC (B) mode.

During conventional SECM imaging, the UME is usually scanned in the (x, y) plane at a constant height above the sample surface. There are several difficulties associated with constant height imaging. As indicated earlier, prior to scanning amperometric UMEs are usually positioned with approach curves. However, this approach is not practical if non-amperometric tips, such as potentiometric sensors or modified UMEs are utilized. Additionally, convolution of topography and electrochemistry may occur during scanning. Faradaic currents are highly dependent on tip-to-sample distance; therefore, rough surfaces will influence the faradaic current observed during the measurement. Finally, sample tilt may lead to tip crashes if large areas are scanned, in particular when

UMEs with smaller dimensions are used for imaging, since those UMEs are positioned particularly close to the sample surfaces. Small UME dimensions are necessary for high electrochemical image resolution. These considerations particularly highlight that improving high-resolution imaging requires not only electrodes of reduced dimensions, but also alternative positioning mechanisms.

Several alternative tip positioning approaches focusing on separation of the current and the topographical information have been reported[77-84]. Ludwig et al.[79] described a concept adapted from distance control in near field scanning optical microscopy (NSOM)[85] that is based on laterally vibrating a fiber-shaped UME during simultaneous SECM operation. The amplitude of the vibration is damped by hydrodynamic forces in the vicinity of the sample, and detected with an optical read-out system. A feedback loop controls the damped amplitude enabling scanning of the UME at a constant distance to the sample surface independent of the faradaic current. In addition to optical shear force detection of the vibration amplitude, tuning fork based detection has been achieved[80-82], likewise adapted from NSOM applications[86], and detection based on piezoelectric elements[83]. Wipf and co-workers have also reported impedance-based distance control[84].

Shear force-based SECM imaging was demonstrated with nanoelectrodes[87], potentiometric tips[88], and microbiosensors[89]. Biological applications moreover included imaging of diaphorase activity, as shown by Matsue and co-workers[82]. Schuhmann and co-workers successfully demonstrated constant distance SECM positioning of UMEs at living cells, and detection of neurotransmitter release from cells[90, 91], along with detection of nitric oxide with electrochemical sensors[92]. SECM-based probing of cell surfaces has also been performed in constant height SECM, and has been discussed in several review

articles[93-96]. However, due to the previously described limitations this approach becomes impractical particularly with decreasing UME size or while scanning surfaces with significant height variations.

2.2.3 AFM-SECM

Both discussed SPM techniques provide useful information about a sample surface. However, there are also several limitations. Although AFM offers the possibility for high resolution topographical imaging, one of the main drawbacks is that chemical information about sample surfaces is not accessible with unmodified tips. In contrast, SECM yields electrochemical information, but with decreased spatial resolution, in addition to the limitations discussed for constant height imaging. Combination of these complementary techniques can overcome the limitations of each individual technique, and is a field of substantial interest recently resulting in the commercialization of an AFM-SECM instrument by Windsor Scientific[97]. Also, Nanonics Imaging provides SECM probes with force sensing capabilities[98].

The primary requirement for combining AFM and SECM technologies is the fabrication of combined probes. So far, two basic approaches for combined probe design have been described in literature. The electrode integrated into the AFM probe can be located either at the very apex of the AFM tip, or at a defined distance recessed from the apex of the tip. The first approach was pioneered by Macpherson and Unwin based on bending of an etched micro-wire and subsequent insulation[99]. The electrode was exposed at the apex of the etched micro-wire by recessing of the insulation layer during a thermal curing process. Similarly, Demaille and co-workers demonstrated that sub-µm sized electrodes were formed at AFM-SECM tip apices by application of high potential pulses[100].

Macpherson and co-workers also used single wall carbon nanotubes attached to an AFM tip as templates for combined AFM-SECM probes[101]. After attachment of the carbon nanotubes to the AFM tips, the assemblies are electrically coated, insulated, and modified by focused ion beam (FIB) milling to expose a nanoelectrode at the apex of the tip. Additionally, several batch fabrication processes have been developed[102-106]. All these approaches have in common that at certain conditions such as electrically conducting samples, topographical and electrochemical information cannot be simultaneously obtained. This typically requires that the sample is scanned twice in lift mode[107], posing a limitation on the real-time combination of topographical and electrochemical information that may be required for example during investigations of dynamic biological systems. Additionally, this approach prevents further chemical modification of the electrode surface with e.g. a biosensing layer. However, these techniques are usually characterized by an excellent electrochemical resolution.

The second approach was pioneered by Kranz et al. utilizing AFM tip-integrated electrodes that are recessed from the apex of the AFM tip[108]. The original AFM tip is reshaped via focused ion beam milling, and acts as a spacer between the electrode and the sample surface. Consequently, the electrode is scanned at a constant distance to the sample surface allowing deconvolution of the electrochemical and the topographical information, if moderate topologies are scanned. The length of the AFM tip can be deliberately adjusted, and is usually linked to the size of the tip-integrated electrode. This combination enables simultaneous AFM-SECM imaging independent of sample properties for *in-situ* correlation of structural information and surface activity; in addition, electrode surface modification is not limited, and tip-integrated sensors may be

applied for simultaneous imaging. The detailed fabrication process is described in *Section 3.2.1*, as recessed AFM-SECM probes were used throughout this thesis. Davoodi et al. have described recessed AFM-SECM probes also based on FIB milling[109]. Additionally, a batch fabrication approach has been reported by our research group (Shin et al.[110, 111]) integrating platinum ring electrodes at silicon wafer level. In general, AFM-SECM experiments have been demonstrated in contact and dynamic mode AFM, as well as feedback and GC mode SECM.

One major advantage of SECM is that quantitative theoretical descriptions and correlation with experimental data is feasible. Mass transport characteristics in SECM have been described for a variety of different UME geometries and conditions[67, 112]. This advantage has also been exploited for bifunctional AFM-SECM techniques. Sklyar et al. performed numerical simulations based on the boundary element method to characterize AFM-SECM probes with recessed electrodes in collaboration with our research group[113]. Experimentally acquired AFM-SECM images were compared with theoretically obtained data, and showed excellent quantitative agreement. Kottke and Fedorov have additionally described advective and transient effects at the same tip-integrated frame electrodes[114]. Similarly, Davoodi et al. performed simulations investigating influences of scan velocity on SECM performance[115]. Finally, Unwin and co-workers published theoretical descriptions of electrically-coated non-insulated AFM probes[116].

Since combined AFM-SECM is a fairly novel development, applications thereof mainly focus on investigations of model substrates. Examples of these substrates include conducting lines[105, 108, 117], conducting rings[118], microelectrodes[101, 106, 107, 111], highly oriented pyrolytic graphite (HOPG)[119], and transport of redox active species through

pores of track etched membranes[99, 120]. Similar membranes were used as model substrates for AFM tip-integrated glucose biosensors[121]. Additionally, electrochemically-induced crystal dissolution was monitored[99, 122]. Other investigations included studies of enzymatic activity at immobilized enzymes such as glucose oxidase[105, 123] and horseradish peroxidase[124], or localized corrosion studies[109, 125-127].

2.3 References

(1) Heinze, J. *Cyclic voltammetry - "Electrochemical Spectroscopy"*, Angew. Chem., Int. Ed. Engl. **1984**, *23*, 831-918.

(2) Lowde, D. R.; Williams, J. O.; McNicol, B. D. *The characterisation of catalyst surfaces by cyclic voltammetry*, Applications of Surface Science **1978**, *1*, 215-240.

(3) Heinze, J.; Dietrich, M. *Cyclic voltammetry as a tool for characterizing conducting polymers*, Mater. Sci. Forum **1989**, *42*, 63-78.

(4) Robinson Donita, L.; Venton, B. J.; Heien Michael, L. A. V.; Wightman, R. M. *Detecting subsecond dopamine release with fast-scan cyclic voltammetry in vivo*, Clin Chem **2003**, *49*, 1763-1773.

(5) http://www.elchsoft.com/; **03/2009**.

(6) Bard, A. J.; Faulkner, L. R. *Electrochemical Methods: Fundamentals and Applications*, 2nd ed.; John Wiley & Sons, Inc.: New York, 2001.

(7) Cottrell, F. G. *Steady current ("reststrom") in galvanic polarisation regarded as a diffusion problem*, Zeit. physikal. Chem. **1903**, *42*, 385-431.

(8) Heinze, J. *Ultramicroelectrodes in Electrochemistry*, Angew. Chem., Int. Ed. Engl. **1993**, *32*, 1268-1288

(9) Zoski, C. G.; Bond, A. M.; Allinson, E. T.; Oldham, K. B. *How long does it take a microelectrode to reach a voltammetric steady state?*, Anal. Chem. **1990**, *62*, 37-45.

(10) Saito, Y. *Theoretical study on the diffusion current at the stationary electrodes of circular and narrow band types*, Rev. Polarogr. **1968**, *15*, 177-187.

(11) Smythe, W. R. *The Capacitance of a Circular Annulus*, J. Appl. Phys. **1951**, *22*, 1499-1501.

(12) Szabo, A. *Theory of the current at microelectrodes: application to ring electrodes*, J. Phys. Chem. **1987**, *91*, 3108-3111.

(13) Wightman, R. M.; Wipf, D. O. *Voltammetry at Ultramicroelectrodes*, In *Electroanal. Chem.*; Bard, A. J., Ed.; Marcel Dekker, Inc.: New York, 1989; Vol. 15, pp 267-353.

(14) Robinson, R. S.; McCreery, R. L. *Absorption spectroelectrochemistry with microelectrodes*, Anal. Chem. **1981**, *53*, 997-1001.

(15) Clark, L. C., Jr.; Lyons, C. *Electrode systems for continuous monitoring in cardiovascular surgery*, Ann. N. Y. Acad. Sci. **1962**, *102*, 29-45.

(16) Harsanyi, G. *Sensors in biomedical applications. May they change the quality of life?*, Sens. Rev. **2001**, *21*, 259-267.

(17) Scheller, F.; Schubert, F. *Biosensors*; Elsevier: Amsterdam, **1992**.

(18) Wang, J. *Electrochemical Glucose Biosensors*, Chem. Rev. **2008**, *108*, 814-825.

(19) Thevenot, D. R.; Toth, K.; Durst, R. A.; Wilson, G. S. *Electrochemical biosensors: recommended definitions and classification*, Pure Appl. Chem. **1999**, *71*, 2333-2348.

(20) Hulanicki, A.; Glab, S.; Ingman, F. *Chemical Sensors. Definitions and Classifications*, Pure Appl. Chem. **1991**, *83*, 1247-1250.

(21) Wang, J. *Glucose biosensors: 40 years of advances and challenges*, Electroanalysis **2001**, *13*, 983-988.

(22) Reach, G.; Wilson, G. S. *Can continuous glucose monitoring be used for the treatment of diabetes?*, Anal. Chem. **1992**, *64*, 381A-386A.

(23) Swamy, B. E. K.; Venton, B. J. *Subsecond detection of physiology adenosine concentrations using fast-scan cyclic voltammetry*, Anal. Chem. **2007**, *79*, 744-750.

(24) Pang, D.-W.; Qi, Y.-P.; Wang, Z.-L.; Cheng, J.-K.; Wang, J.-W. *Electrochemical oxidation of DNA at a gold microelectrode*, Electroanalysis **1995**, *7*, 774-777.

(25) Llaudet, E.; Hatz, S.; Droniou, M.; Dale, N. *Microelectrode biosensor for real-time measurement of ATP in biological tissue*, Anal. Chem. **2005**, *77*, 3267-3273.

(26) Pearson, R. A.; Dale, N.; Llaudet, E.; Mobbs, P. *ATP released via gap junction hemichannels from the pigment epithelium regulates neural retinal progenitor proliferation*, Neuron **2005**, *46*, 731-744.

(27) Gourine, A. V.; Llaudet, E.; Dale, N.; Spyer, K. M. *Release of ATP in the ventral medulla during hypoxia in rats: role in hypoxic ventilatory response*, J. Neurosci. **2005**, *25*, 1211-1218.

(28) Masson, J.-F.; Kranz, C.; Mizaikoff, B.; Gauda, E. B. *Amperometric ATP microbiosensors for the analysis of chemosensitivity at rat carotid bodies*, Anal. Chem. **2008**, *80*, 3991-3998.

(29) Gourine, A. V.; Llaudet, E.; Dale, N.; Spyer, K. M. *ATP is a mediator of chemosensory transduction in the central nervous system*, Nature **2005**, *436*, 108-111.

(30) Yang, X.; Johansson, G.; Pfeiffer, D.; Scheller, F. *Enzyme electrodes for ADP/ATP with enhanced sensitivity due to chemical amplification and intermediate accumulation*, Electroanalysis **1991**, *3*, 659-663.

(31) Cui, Y.; Barford, J. P.; Renneberg, R. *Amperometric trienzyme ATP biosensors based on the coimmobilization of salicylate hydroxylase, glucose-6-phosphate dehydrogenase, and hexokinase*, Sens. Actuators, B **2008**, *B132*, 1-4.

(32) Ghica, M. E.; Brett, C. M. A. *Development and applications of a bienzymatic amperometric glycerol biosensor based on a poly(neutral red) modified carbon film electrode*, Anal. Lett. **2006**, *39*, 1527-1542.

(33) Scheller, F.; Pfeiffer, D. *Glucose oxidase-hexokinase bienzyme electrode sensor for adenosine triphosphate*, Anal. Chim. Acta **1980**, *117*, 383-386.

(34) Compagnone, D.; Guilbault, G. G. *Glucose oxidase/hexokinase electrode for the determination of ATP*, Anal. Chim. Acta **1997**, *340*, 109-113.

(35) Liu, S.; Sun, Y. *Co-immobilization of glucose oxidase and hexokinase on silicate hybrid sol-gel membrane for glucose and ATP detections*, Biosens. Bioelectron. **2007**, *22*, 905-911.

(36) Kueng, A.; Kranz, C.; Mizaikoff, B. *Amperometric ATP biosensor based on polymer entrapped enzymes*, Biosens. Bioelectron. **2004**, *19*, 1301-1307.

(37) Binnig, G.; Rohrer, H.; Gerber, C.; Weibel, E. *Tunneling through a controllable vacuum gap*, Appl. Phys. Lett. **1982**, *40*, 178-180.

(38) Binnig, G.; Rohrer, H.; Gerber, C.; Weibel, E. *Surface studies by Scanning Tunneling Microscopy*, Phys. Rev. Lett. **1982**, *49*, 57-61.

(39) Binnig, G.; Quate, C. F.; Gerber, C. *Atomic Force Microscope*, Phys. Rev. Lett. **1986**, *56*, 930-933.

(40) Meyer, G.; Amer, N. M. *Novel optical approach to atomic force mircoscopy*, Appl. Phys. Lett. **1988**, *53*, 1045-1047.

(41) Duerig, U.; Zueger, O.; Stalder, A. *Interaction force detection in scanning probe microscopy: methods and applications*, J. Appl. Phys. **1992**, *72*, 1778-1798.

(42) Martin, Y.; Williams, C. C.; Wickramasinghe, H. K. *Atomic force microscope-force mapping and profiling on a sub 100-.ANG. scale*, J. Appl. Phys. **1987**, *61*, 4723-4729.

(43) Putman, C. A. J.; van der Werf, K. O.; De Grooth, B. G.; Van Hulst, N. F.; Greve, J. *Tapping mode atomic force microscopy in liquid*, Appl. Phys. Lett. **1994**, *64*, 2454-2456.

(44) Le Grimellec, C.; Giocondi, M.-C.; Pujol, R.; Lesniewska, E. *Tapping mode atomic force microscopy allows the in situ imaging of fragile membrane structures and of intact cells surface at high resolution*, Single Molecules **2000**, *1*, 105-107.

(45) Florin, E. L.; Moy, V. T.; Gaub, H. E. *Adhesion forces between individual ligand-receptor pairs*, Science **1994**, *264*, 415-417.

(46) Lee, G. U.; Kidwell, D. A.; Colton, R. J. *Sensing Discrete Streptavidin-Biotin Interactions with Atomic Force Microscopy*, Langmuir **1994**, *10*, 354-357.

(47) Janshoff, A.; Neitzert, M.; Oberdorfer, Y.; Fuchs, H. *Force spectroscopy of molecular systems - single molecule spectroscopy of polymers and biomolecules*, Angew. Chem., Int. Ed. **2000**, *39*, 3212-3237.

(48) Willemsen, O. H.; Snel, M. M.; Cambi, A.; Greve, J.; De Grooth, B. G.; Figdor, C. G. *Biomolecular interactions measured by atomic force microscopy*, Biophys. J. **2000**, *79*, 3267-3281.

(49) Carrion-Vazquez, M.; Oberhauser, A. F.; Fisher, T. E.; Marszalek, P. E.; Li, H.; Fernandez, J. M. *Mechanical design of proteins studied by single-molecule force spectroscopy and protein engineering*, Prog. Biophys. Molec. Biol. **2000**, *74*, 63-91.

(50) Zlatanova, J.; Lindsay, S. M.; Leuba, S. H. *Single molecule force spectroscopy in biology using the atomic force microscope*, Progress in Biophysics & Molecular Biology **2000**, *74*, 37-61.

(51) Hinterdorfer, P.; Baumgartner, W.; Gruber, H. J.; Schilcher, K.; Schindler, H. *Detection and localization of individual antibody-antigen recognition events by atomic force microscopy*, Proc. Natl. Acad. Sci. U. S. A. **1996**, *93*, 3477-3481.

(52) Raab, A.; Han, W.; Badt, D.; Smith-Gill, S. J.; Lindsay, S. M.; Schindler, H.; Hinterdorfer, P. *Antibody recognition imaging by force microscopy*, Nat. Biotechnol. **1999**, *17*, 902-905.

(53) Scheuring, S.; Fotiadis, D.; Moller, C.; Muller, S. A.; Engel, A.; Muller, D. J. *Single proteins observed by atomic force microscopy*, Single Molecules **2001**, *2*, 59-67.

(54) Hansma, H. G. *Surface biology of DNA by atomic force microscopy*, Annu. Rev. Phys. Chem. **2001**, *52*, 71-92.

(55) Hansma, H. G.; Kasuya, K.; Oroudjev, E. *Atomic force microscopy imaging and pulling of nucleic acids*, Curr. Opin. Struct. Biol. **2004**, *14*, 380-385.

(56) Fotiadis, D.; Scheuring, S.; Muller, S. A.; Engel, A.; Muller, D. J. *Imaging and manipulation of biological structures with the AFM*, Micron **2002**, *33*, 385-397.

(57) Ando, T.; Uchihashi, T.; Fukuma, T. *High-speed atomic force microscopy for nano-visualization of dynamic biomolecular processes*, Prog. Surf. Sci. **2008**, *83*, 337-437.

(58) Radmacher, M.; Tillamnn, R. W.; Fritz, M.; Gaub, H. E. *From molecules to cells: imaging soft samples with the atomic force microscope*, Science **1992**, *257*, 1900-1905.

(59) Henderson, E. *Imaging of living cells by atomic force microscopy*, Prog. Surf. Sci. **1994**, *46*, 39-60.

(60) Ohnesorge, F. M.; Horber, J. K.; Haberle, W.; Czerny, C. P.; Smith, D. P.; Binnig, G. *AFM review study on pox viruses and living cells*, Biophys. J. **1997**, *73*, 2183-2194.

(61) You, H. X.; Yu, L. *Atomic force microscopy imaging of living cells: progress, problems and prospects*, Methods Cell Sci **1999**, *21*, 1-17.

(62) Dufrene, Y. F. *AFM for nanoscale microbe analysis*, Analyst **2008**, *133*, 297-301.

(63) Engstrom, R. C.; Weber, M.; Wunder, D. J.; Burgess, R.; Winquist, S. *Measurements within the diffusion layer using a microelectrode probe*, Anal. Chem. **1986**, *58*, 844-848.

(64) Liu, H. Y.; Fan, F. R. F.; Lin, C. W.; Bard, A. J. *Scanning electrochemical and tunneling ultramicroelectrode microscope for high-resolution examination of electrode surfaces in solution*, J. Am. Chem. Soc. **1986**, *108*, 3838-3839.

(65) Bard, A. J.; Fan, F. R. F.; Kwak, J.; Lev, O. *Scanning electrochemical microscopy. Introduction and principles*, Anal. Chem. **1989**, *61*, 132-138.

(66) Bard, A. J.; Fan, F. R. F.; Pierce, D. T.; Unwin, P. R.; Wipf, D. O.; Zhou, F. *Chemical imaging of surfaces with the scanning electrochemical microscope*, Science **1991**, *254*, 68-74.

(67) Bard, A. J.; Fan, F. R. F.; Mirkin Michael, V. *Scanning electrochemical microscopy*, In *Electroanalytical chemistry: a series of advances*; Bard, A. J., Ed.; Marcel Dekker: New York, 1994; Vol. 18, pp 243-373.

(68) Lee, Y.; Amemiya, S.; Bard, A. J. *Scanning Electrochemical Microscopy. 41. Theory and Characterization of Ring Electrodes*, Anal. Chem. **2001**, *73*, 2261-2267.

(69) Liljeroth, P.; Johans, C.; Slevin, C. J.; Quinn, B. M.; Kontturi, K. *Micro ring-disk electrode probes for scanning electrochemical microscopy*, Electrochem. Commun. **2002**, *4*, 67-71.

(70) Liljeroth, P.; Johans, C.; Slevin, C. J.; Quinn, B. M.; Kontturi, K. *Disk-Generation/Ring-Collection Scanning Electrochemical Microscopy: Theory and Application*, Anal. Chem. **2002**, *74*, 1972-1978.

(71) Mirkin, M. V.; Fan, F. R. F.; Bard, A. J. *Scanning electrochemical microscopy. Part 13. Evaluation of the tip shapes of nanometer size microelectrodes*, J. Electroanal. Chem. **1992**, *328*, 47-62.

(72) Zoski, C. G.; Mirkin, M. V. *Steady-State Limiting Currents at Finite Conical Microelectrodes*, Anal. Chem. **2002**, *74*, 1986-1992.

(73) Kwak, J.; Bard, A. J. *Scanning electrochemical microscopy. Theory of the feedback mode*, Anal. Chem. **1989**, *61*, 1221-1227.

(74) Lee, C.; Kwak, J.; Anson, F. C. *Application of scanning electrochemical microscopy to generation/collection experiments with high collection efficiency*, Anal. Chem. **1991**, *63*, 1501-1504.

(75) Shao, Y.; Mirkin, M. V.; Fish, G.; Kokotov, S.; Palanker, D.; Lewis, A. *Nanometer-Sized Electrochemical Sensors*, Anal. Chem. **1997**, *69*, 1627-1634.

(76) Wittstock, G.; Burchardt, M.; Pust, S. E.; Shen, Y.; Zhao, C. *Scanning electrochemical microscopy for direct imaging of reaction rates*, Angew. Chem., Int. Ed. **2007**, *46*, 1584-1617.

(77) Wipf, D. O.; Bard, A. J.; Tallman, D. E. *Scanning electrochemical microscopy. 21. Constant-current imaging with an autoswitching controller*, Anal. Chem. **1993**, *65*, 1373-1377.

(78) Borgwarth, K.; Ebling, D. G.; Heinze, J. *Scanning electrochemical microscopy: a new scanning mode based on convective effects*, Berichte der Bunsen-Gesellschaft **1994**, *98*, 1317-1321.

(79) Ludwig, M.; Kranz, C.; Schuhmann, W.; Gaub, H. E. *Topography feedback mechanism for the scanning electrochemical microscope based on hydrodynamic forces between tip and sample*, Rev. Sci. Instrum. **1995**, *66*, 2857-2860.

(80) James, P. I.; Garfias-Mesias, L. F.; Moyer, P. J.; Smyrl, W. H. *Scanning electrochemical microscopy with simultaneous independent topography*, J. Electrochem. Soc. **1998**, *145*, L64-L66.

(81) Buechler, M.; Kelley, S. C.; Smyrl, W. H. *Scanning electrochemical microscopy with shear force feedback. Investigation of the lateral resolution of different experimental configurations*, Electrochem. Solid-State Lett. **2000**, *3*, 35-38.

(82) Oyamatsu, D.; Hirano, Y.; Kanaya, N.; Mase, Y.; Nishizawa, M.; Matsue, T. *Imaging of enzyme activity by scanning electrochemical microscope equipped*

with a feedback control for substrate-probe distance, Bioelectrochemistry **2003**, *60*, 115-121.

(83) Katemann, B. B.; Schulte, A.; Schuhmann, W. *Constant-distance mode scanning electrochemical microscopy (SECM)-part I: Adaptation of a non-optical shear-force-based positioning mode for SECM tips*, Chem.--Eur. J. **2003**, *9*, 2025-2033.

(84) Alpuche-Aviles, M. A.; Wipf, D. O. *Impedance Feedback Control for Scanning Electrochemical Microscopy*, Anal. Chem. **2001**, *73*, 4873-4881.

(85) Betzig, E.; Finn, P. L.; Weiner, J. S. *Combined shear force and near-field scanning optical microscopy*, Appl. Phys. Lett. **1992**, *60*, 2484-2486.

(86) Karrai, K.; Grober, R. D. *Piezoelectric tip-sample distance control for near field optical microscopes*, Appl. Phys. Lett. **1995**, *66*, 1842-1844.

(87) Katemann, B. B.; Schulte, A.; Schuhmann, W. *Constant-distance mode scanning electrochemical microscopy. Part II: High-resolution SECM imaging employing Pt nanoelectrodes as miniaturized scanning probes*, Electroanalysis **2004**, *16*, 60-65.

(88) Etienne, M.; Schulte, A.; Mann, S.; Jordan, G.; Dietzel, I. D.; Schuhmann, W. *Constant-Distance Mode Scanning Potentiometry. 1. Visualization of Calcium Carbonate Dissolution in Aqueous Solution*, Anal. Chem. **2004**, *76*, 3682-3688.

(89) Hengstenberg, A.; Kranz, C.; Schuhmann, W. *Facilitated tip-positioning and applications of non-electrode tips in scanning electrochemical microscopy using a shear force based constant-distance mode*, Chem.--Eur. J. **2000**, *6*, 1547-1554.

(90) Hengstenberg, A.; Blochl, A.; Dietzel, I. D.; Schuhmann, W. *Spatially resolved detection of neurotransmitter secretion from individual cells by means of scanning electrochemical microscopy*, Angew. Chem., Int. Ed. **2001**, *40*, 905-908.

(91) Bauermann, L. P.; Schuhmann, W.; Schulte, A. *An advanced biological scanning electrochemical microscope (Bio-SECM) for studying individual living cells*, Phys. Chem. Chem. Phys. **2004**, *6*, 4003-4008.

(92) Isik, S.; Schuhmann, W. *Detection of nitric oxide release from single cells by using constant-distance-mode scanning electrochemical microscopy*, Angew. Chem., Int. Ed. **2006**, *45*, 7451-7454.

(93) Yasukawa, T.; Kaya, T.; Matsue, T. *Characterization and imaging of single cells with scanning electrochemical microscopy*, Electroanalysis **2000**, *12*, 653-659.

(94) Amemiya, S.; Guo, J.; Xiong, H.; Gross, D. A. *Biological applications of scanning electrochemical microscopy: chemical imaging of single living cells and beyond*, Anal. Bioanal. Chem. **2006**, *386*, 458-471.

(95) Bard, A. J.; Li, X.; Zhan, W. *Chemically imaging living cells by scanning electrochemical microscopy*, Biosens. Bioelectron. **2006**, *22*, 461-472.

(96) Schulte, A.; Schuhmann, W. *Single-cell microelectrochemistry*, Angew. Chem., Int. Ed. **2007**, *46*, 8760-8777.

(97) Windsor Scientific *http://www.windsorscientific.co.uk/*; **03/2009**.

(98) Nanonics Imaging *http://www.nanonics.co.il/*; **03/2009**.

(99) Macpherson, J. V.; Unwin, P. R. *Combined Scanning Electrochemical-Atomic Force Microscopy*, Anal. Chem. **2000**, *72*, 276-285.

(100) Abbou, J.; Demaille, C.; Druet, M.; Moiroux, J. *Fabrication of Submicrometer-Sized Gold Electrodes of Controlled Geometry for Scanning Electrochemical-Atomic Force Microscopy*, Anal. Chem. **2002**, *74*, 6355-6363.

(101) Burt, D. P.; Wilson, N. R.; Weaver, J. M. R.; Dobson, P. S.; Macpherson, J. V. *Nanowire Probes for High Resolution Combined Scanning Electrochemical Microscopy - Atomic Force Microscopy*, Nano Lett. **2005**, *5*, 639-643.

(102) Akiyama, T.; Gullo, M. R.; De Rooij, N. F.; Tonin, A.; Hidber, H.-R.; Frederix, P. L. T. M.; Engel, A.; Staufer, U. *Development of insulated conductive probes with platinum silicide tips for atomic force microscopy in cell biology*, Jpn. J. Appl. Phys., Part 1 **2004**, *43*, 3865-3867.

(103) Fasching, R. J.; Tao, Y.; Prinz, F. B. *Fabrication of an electrochemical tip-probe system embedded in SiNx cantilevers for simultaneous SECM and AFM analysis*, Proceedings of SPIE-The International Society for Optical Engineering **2004**, *5342*, 53-64.

(104) Fasching, R. J.; Tao, Y.; Prinz, F. B. *Cantilever tip probe arrays for simultaneous SECM and AFM analysis*, Sens. Actuators, B **2005**, *B108*, 964-972.

(105) Hirata, Y.; Yabuki, S.; Mizutani, F. *Application of integrated SECM ultra-micro-electrode and AFM force probe to biosensor surfaces*, Bioelectrochemistry **2004**, *63*, 217-224.

(106) Dobson, P. S.; Weaver, J. M. R.; Holder, M. N.; Unwin, P. R.; Macpherson, J. V. *Characterization of Batch-Microfabricated Scanning Electrochemical-Atomic Force Microscopy Probes*, Anal. Chem. **2005**, *77*, 424-434.

(107) Macpherson, J. V.; Unwin, P. R. *Noncontact electrochemical imaging with combined scanning electrochemical atomic force microscopy*, Anal. Chem. **2001**, *73*, 550-557.

(108) Kranz, C.; Friedbacher, G.; Mizaikoff, B.; Lugstein, A.; Smoliner, J.; Bertagnolli, E. *Integrating an Ultramicroelectrode in an AFM Cantilever: Combined Technology for Enhanced Information*, Anal. Chem. **2001**, *73*, 2491-2500.

(109) Davoodi, A.; Pan, J.; Leygraf, C.; Norgren, S. *In Situ Investigation of Localized Corrosion of Aluminum Alloys in Chloride Solution Using Integrated EC-AFM/SECM Techniques*, Electrochem. Solid-State Lett. **2005**, *8*, B21-B24.

(110) Shin, H.; Hesketh, P. J.; Mizaikoff, B.; Kranz, C. *Batch Fabrication of Atomic Force Microscopy Probes with Recessed Integrated Ring Microelectrodes at a Wafer Level*, Anal. Chem. **2007**, *79*, 4769-4777.

(111) Shin, H.; Hesketh, P. J.; Mizaikoff, B.; Kranz, C. *Development of wafer-level batch fabrication for combined atomic force-scanning electrochemical microscopy (AFM-SECM) probes*, Sens. Actuators, B **2008**, *B134*, 488-495.

(112) Mirkin, M. V.; Horrocks, B. R. *Electroanalytical measurements using the scanning electrochemical microscope*, Anal. Chim. Acta **2000**, *406*, 119-146.

(113) Sklyar, O.; Kueng, A.; Kranz, C.; Mizaikoff, B.; Lugstein, A.; Bertagnolli, E.; Wittstock, G. *Numerical Simulation of Scanning Electrochemical Microscopy Experiments with Frame-Shaped Integrated Atomic Force Microscopy-SECM Probes Using the Boundary Element Method*, Anal. Chem. **2005**, *77*, 764-771.

(114) Kottke, P. A.; Fedorov, A. G. *Advective and transient effects in combined AFM/SECM operation*, J. Electroanal. Chem. **2005**, *583*, 221-231.

(115) Davoodi, A.; Farzadi, A.; Pan, J.; Leygraf, C.; Zhu, Y. *Developing an AFM-Based SECM System; Instrumental Setup, SECM Simulation, Characterization, and Calibration*, J. Electrochem. Soc. **2008**, *155*, C474-C485.

(116) Holder, M. N.; Gardner, C. E.; Macpherson, J. V.; Unwin, P. R. *Combined scanning electrochemical-atomic force microscopy (SECM-AFM): Simulation and experiment for flux-generation at un-insulated metal-coated probes*, J. Electroanal. Chem. **2005**, *585*, 8-18.

(117) Gullo, M. R.; Frederix, P. L. T. M.; Akiyama, T.; Engel, A.; de Rooij, N. F.; Staufer, U. *Characterization of Microfabricated Probes for Combined Atomic Force and High-Resolution Scanning Electrochemical Microscopy*, Anal. Chem. **2006**, *78*, 5436-5442.

(118) Kueng, A.; Kranz, C.; Mizaikoff, B.; Lugstein, A.; Bertagnolli, E. *Combined scanning electrochemical atomic force microscopy for tapping mode imaging*, Appl. Phys. Lett. **2003**, *82*, 1592-1594.

(119) Frederix, P. L. T. M.; Bosshart, P. D.; Akiyama, T.; Chami, M.; Gullo, M. R.; Blackstock, J. J.; Dooleweerdt, K.; de Rooij, N. F.; Staufer, U.; Engel, A.

Conductive supports for combined AFM-SECM on biological membranes, Nanotechnology **2008**, *19*, 384004/384001-384004/384010.

(120) Gardner, C. E.; Unwin, P. R.; Macpherson, J. V. *Correlation of membrane structure and transport activity using combined scanning electrochemical-atomic force microscopy*, Electrochem. Commun. **2005**, *7*, 612-618.

(121) Kueng, A.; Kranz, C.; Lugstein, A.; Bertagnolli, E.; Mizaikoff, B. *AFM-tip-integrated amperometric microbiosensors: High-resolution imaging of membrane transport*, Angew. Chem., Int. Ed. **2005**, *44*, 3419-3422.

(122) Jones, C. E.; Unwin, P. R.; Macpherson, J. V. *In situ observation of the surface processes involved in dissolution from the cleavage surface of calcite in aqueous solution using combined scanning electrochemical - atomic force microscopy (SECM-AFM)*, ChemPhysChem **2003**, *4*, 139-146.

(123) Kueng, A.; Kranz, C.; Lugstein, A.; Bertagnolli, E.; Mizaikoff, B. *Integrated AFM-SECM in tapping mode: Simultaneous topographical and electrochemical imaging of enzyme activity*, Angew. Chem., Int. Ed. **2003**, *42*, 3238-3240.

(124) Kranz, C.; Kueng, A.; Lugstein, A.; Bertagnolli, E.; Mizaikoff, B. *Mapping of enzyme activity by detection of enzymatic products during AFM imaging with integrated SECM-AFM probes*, Ultramicroscopy **2004**, *100*, 127-134.

(125) Davoodi, A.; Pan, J.; Leygraf, C.; Norgren, S. *Probing of local dissolution of Al alloys in chloride solutions by AFM and SECM*, Appl. Surf. Sci. **2006**, *252*, 5499-5503.

(126) Davoodi, A.; Pan, J.; Leygraf, C.; Norgren, S. *Integrated AFM and SECM for in situ studies of localized corrosion of Al alloys*, Electrochim. Acta **2007**, *52*, 7697-7705.

(127) Davoodi, A.; Pan, J.; Leygraf, C.; Norgren, S. *The role of intermetallic particles in localized corrosion of an aluminum alloy studied by SKPFM and integrated AFM/SECM*, J. Electrochem. Soc. **2008**, *155*, C211-C218.

3 PLASMA-DEPOSITED FLUOROCARBON FILMS AS INSULATION MATERIAL FOR AFM-SECM PROBES AND UMES

In this chapter plasma-deposited fluorocarbon films are presented as alternative insulation materials for AFM-SECM probes and UMEs. Electrochemical characterization of the insulation layer quality is performed. Additionally, combined AFM-SECM approach and imaging studies are described.

3.1 Motivation

One of the key requirements for successful AFM-SECM experiments is sufficient quality of the electrical insulation of combined AFM-SECM probes. It is crucial that this insulation layer is pinhole-free, uniform, well-adherent, and stable, and that all parts immersed in solution including the chip are well-insulated. Additionally, the thickness of the layer is particularly important for imaging a wide range of samples including high-aspect ratio topographical features. The electrode-to-insulation ratio, defined as RG value and described by *Equation (2.17)*, plays an important role in the diffusion behavior towards the electrode surface[1]. RG values approaching unity are desirable for electrochemical scanning probe experiments, since the flux to the electrode can be considerably enhanced via diffusion from behind the electrode plane. Moreover, a thin insulation layer leads to a lower interference probability by the probe to the sample

surface during AFM imaging, as demonstrated in *Figure 3.1* for a sample surface with significant topographical feature changes such as cells.

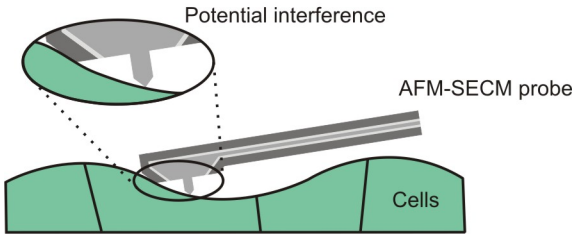

Figure 3.1. Scheme of potential interference between AFM-SECM probes with thick insulation and a cell layer with changing topographical features in the low µm range.

Typical insulation materials applied for the insulation of recessed AFM-SECM probes are silicon nitride, silicon nitride-silicon oxide sandwich layers, and Parylene C[2-5]. Probes insulated with these materials exhibit adequate imaging characteristic, however, the thickness of the insulation layer is usually in the range of 0.7 – 1 µm. Depending on the surface topography of the sample investigated, a thickness of the insulation layer up to 1 µm may not be applicable. Therefore, alternative insulation strategies leading to improved insulating properties with thinner coatings (< 0.7 µm) are necessary. In this thesis, plasma-polymerized fluorocarbon layers are evaluated as a novel approach for the insulation of UMEs, and of combined AFM-SECM probes.

3.1.1 General insulation techniques

Quantitative analysis of analytes during electroanalytical experiments at the micro- and nanoscale requires pinhole-free and uniform electrical insulation. Commonly, UMEs are insulated by encapsulation in glass. Detailed reviews on this procedure can be found in

literature[6-9]. Although encapsulation in glass is useful for sealing microwires, this approach is not applicable for specialized UMEs such as AFM-SECM tip-integrated electrodes or for specialized applications such as *in-vivo* experiments.

Alternative techniques for the insulation of microwires or etched nanoelectrodes have been reported in literature[10-25]. Early approaches include dipping of a microwire into varnish[26, 27] or molten apiezon wax[10, 28], as well as translating a microwire through molten paraffin[20]. The most popular approach among electrodeposited insulation layers for sub-µm sized electrodes involves the use of electrodeposition paints (EDPs)[17, 18, 21, 23, 29-35]. Typically, an EDP layer is formed by an electrochemically-induced pH shift, which leads to a solubility change of the polymer and its precipitation at the electrode surface. Subsequently, the deposited film is cross-linked in a curing step to achieve electrically insulating properties. Other electropolymerization techniques involving polyphenyleneoxide[12, 24] or photoresist[25] have been applied towards insulating carbon fiber electrodes. Carbon fibers have also been insulated with polytetrafluoroethylene (PTFE) by pulling and melting a PTFE capillary around the fiber[13]. Vacuum-based deposition techniques such as chemical vapor deposition (CVD) of silica[36] or polyimide[37], and plasma-enhanced CVD (PECVD) of perfluoro-octane[38] have been applied. The group of vacuum-based techniques also includes chemical vapor polymerization of Parylene C, which is commercially used for the insulation of UMEs[11, 39, 40].

Common for all different types of AFM-SECM probes, which have been applied in imaging experiments as discussed in *Section 2.2.3*, is the necessity of a superior insulation layer. Silicon nitride, silicon oxide or Parylene C are usually employed in

AFM-SECM probes fabricated by standard microfabrication processes; nanoelectrodes bent into the shape of an AFM cantilever have been insulated with anodic and cathodic EDPs, as described above[31, 33]. Conical nanoelectrodes were obtained due to recessing of the paint from the apex of the wire during the curing process in the case of anodic paint insulation[33]. Cathodic paints were deposited at cantilever-shaped spherical gold electrodes by scanning the potential between 0 V and 5 V[31]. After thermal curing, the insulation layer at the apex of the tip was locally removed by application of a high voltage pulse in the 1.5 -6 kV range leading to the exposure of the spherical electrode geometry. However, microfabrication processes generally lead to more reproducible insulation layers.

3.1.2 Plasma polymerization

Plasma polymerization has been frequently employed for the fabrication of thin polymer films from a variety of organic precursors[41-44]. The organic precursor is excited in an electrical discharge, which leads to the deposition of a highly cross-linked film at the exposed substrate surface. Since plasma-deposited films have many desirable properties including mechanical and thermal stability, chemical inertness, and insolubility, they have been used in a variety of applications[45]. Furthermore, the composition and chemical structure of these films can be readily modified by variation of process conditions, including substrate temperature, frequency of the discharge, radio frequency (RF) power level, reactor pressure, selection of monomer(s), and flow rate(s)[46]. By tuning these parameters, plasma-polymerized layers may be optimized for different properties.

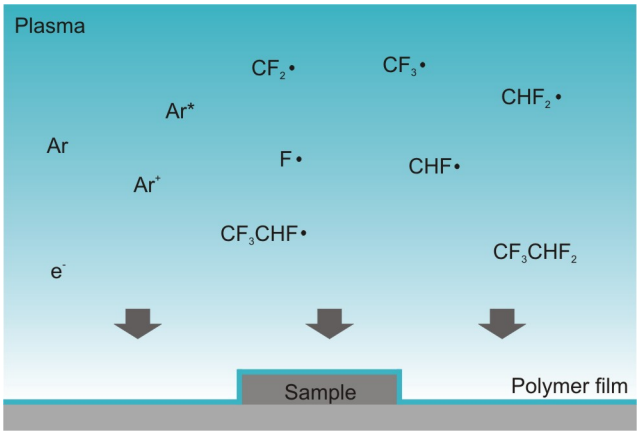

Figure 3.2. Schematic of plasma polymerization process and involved pentafluoroethane precursor fragments.

Plasma-polymerized insulation layers presented in this thesis were deposited in a parallel plate radio frequency plasma reactor using pentafluoroethane (PFE, CF_3CHF_2) as a precursor gas[47]. A schematic of the polymerization process and the involved precursor fragments is depicted in *Figure 3.2*. Thermal stability and electrical properties of fluorocarbon layers prepared from PFE vapor along with plasma chemistry involved in their deposition have been previously studied[48-50]. Fluorocarbon layers are an attractive choice for thin film insulation strategies, since they are highly resistive, chemically inert, biocompatible, and provide in addition the advantage of conformal step coverage with thin and uniform layers[51]. Besides the improved SECM and AFM imaging quality due to reduced insulation thicknesses, fast PFE milling rates also imply decreased focused ion beam milling time resulting in a reduced overall processing time, and hence, reduced costs. Moreover, the described insulation process can be performed at a batch-level, which ensures uniform and reproducible coatings.

3.2 Experimental

3.2.1 AFM-SECM probe fabrication

AFM-SECM probes were prepared in a multi-step procedure involving several coating and microstructuring techniques[2]. Commercially available gold-coated triangular silicon nitride AFM probes (Veeco, Woodbury, NY) were used as basis for the combined probes. Prior to the coating procedure, the reflecting gold and underlying adhesive chromium layer were removed with gold (GE-8110, Transene, Danvers, MA) and chromium etchant solutions (CR7-S, Cyantek, Fremont, CA). Subsequently, a titanium adhesion layer (approx. 10 nm), and a gold electrode layer (100 – 150 nm) were sputtered onto the AFM probes using a mask defining a conductive line-shaped pattern onto the glass chip. For both metallizations, a DC sputterer (CVC, Rochester, NY) equipped with an 8'' titanium target and a 3'' gold target was utilized. Power settings were at 2500 W and 350 W, respectively.

Besides deposition of PFE insulation layers described in *Section 3.2.2*, standard AFM-SECM probe modification involving commonly used insulation materials will be discussed here. Silicon nitride-silicon oxide sandwich insulation layers were deposited in a PECVD system (Unaxis, CH). Typical parameters used for the deposition were a bottom electrode temperature of 150 ºC, a pressure of 1100 mTorr (silicon nitride) or 900 mTorr (silicon oxide), a power of 50 W (silicon nitride) or 25 W (silicon oxide), and gas flow rates extracted from *Table 3.1*. Typically three alternating layers (nitride-oxide-nitride) were deposited at cantilevers to ensure pinhole-free insulation. Cantilevers were placed perpendicular to the deposition plasma during the deposition to reduce stress.

Deposition times were adjusted depending on the deposited thickness from respective calibrations. After deposition of the insulation layer, the quality of the electrical insulation was tested by recording cyclic voltammograms.

Table 3.1. Summary of flow rates used in the PECVD deposition process of silicon nitride and silicon oxide insulation layers.

Material	Gas	Flow rate [sccm]
Si_xN_y	SiH_4	4
	NH_3	5
	N_2	1100
SiO_2	SiH_4	400
	N_2O	900

After coating the cantilevers, focused ion beam milling was used to expose the tip-integrated electroactive area, and to reshape the AFM tip. Two different FIB instruments were utilized during this work for milling and scanning electron microscopy (SEM) imaging purposes (Quanta^{TM} 200 3D and Nova^{TM} 200 NanoLab DualBeam^{TM} systems, FEI Company, Hillsboro, OR). *Figure 3.3* shows the involved milling steps, and the corresponding SEM images. A bitmap with a user-defined shape may be uploaded into the instrumental software, and may be used as a digital mask for the milling procedure. FIB milling is performed in two steps: in the first cut, the modified probe is mounted such that the front view of the cantilever is exposed to the ion beam (*Figure 3.3A*), whereas for the second cut the cantilever is rotated by 90º in respect to the first cut (*Figure 3.3B*). Following each milling step, a cross-sectional FIB cleaning step is applied to remove possibly re-deposited material from the electrode surface. *Figure 3.3C* shows a

final view of the FIB-milled AFM-SECM probe. For some applications, AFM-SECM probes without reshaped AFM tips were fabricated. In this case, the FIB processing time is considerably shorter, as only one milling step is performed.

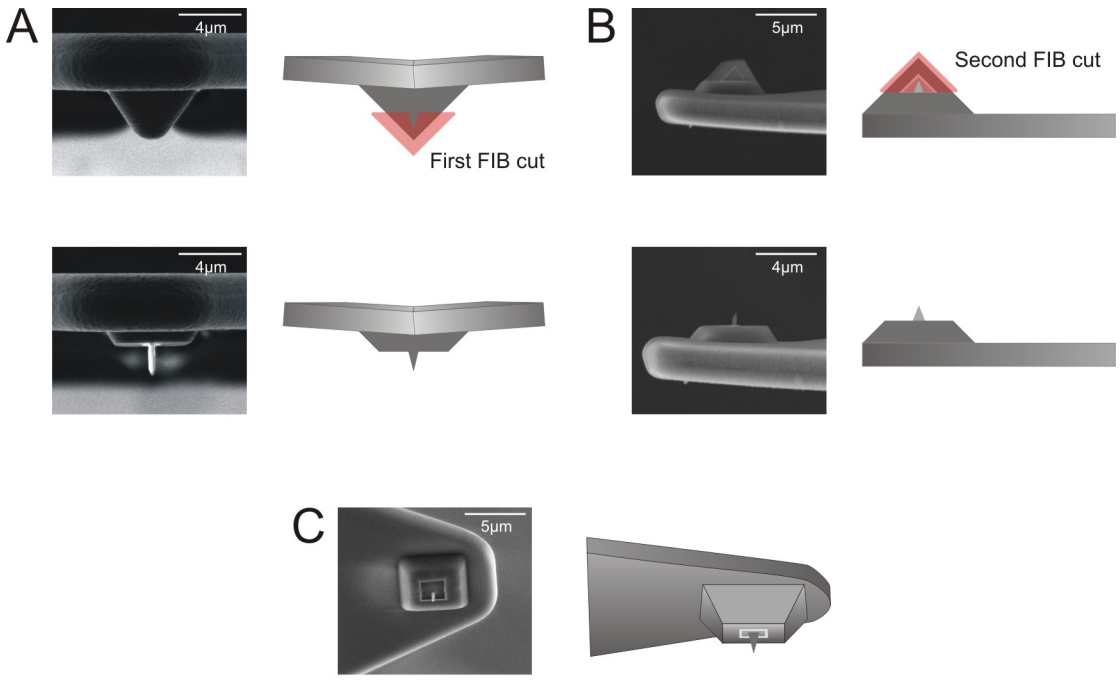

Figure 3.3. Schemes and SEM images of FIB milling steps involved in the fabrication of AFM-SECM probes. Bitmap masks used to mill the probes are shaded red. (A) Front view used for the first FIB cut, (B) side view (rotation by 90º) used for the second FIB cut and (C) final view showing an AFM-SECM probe after FIB processing.

3.2.2 Plasma depositions of PFE films

Plasma depositions of PFE films were performed in collaboration with Dr. Dennis W. Hess at the School of Chemical and Biomolecular Engineering (Georgia Institute of Technology).

3.2.2.1 Samples

AFM-SECM probes were cleaned after titanium and gold metallization in an UV/ozone chamber (BioForce Nanosciences, Ames, IA) for 20 min prior to the PFE insulation procedure. Other preparation conditions including the FIB milling steps after the insulation were the same as already described in *Section 3.2.1*.

Gold microwires with a diameter of 25 µm (Goodfellow, U.K.) were used to further evaluate the applicability of PFE insulation layers in microelectrochemistry. Similarly to modified AFM probes, gold microwires were cleaned for 20 min in an UV/ozone chamber prior to PFE deposition. Additionally, PFE-coated gold UMEs were prepared by sealing microwires into glass capillaries. Microwires were sealed in the glass with a small section protruding from the end of the capillary, which was subsequently insulated with a PFE layer. To expose the electroactive cross-section of the microwire, FIB milling was performed.

For each AFM-SECM probe and gold microwire deposition run, blank silicon wafer chips were used as control samples for monitoring of the layer thicknesses with a planar reference sample.

3.2.2.2 Plasma reactor reagents

Pentafluoroethane monomer gas (N4 grade, 99.99 %) was donated by Dupont (Wilmington, DE). Argon carrier gas (Ultra High Purity, 99.99 %) was obtained from Air Products and Chemicals Inc. (Allentown, PA), whereas nitrogen (Ultra High Purity, 99.999 %) and oxygen (Ultra Pure Carrier, 99.996 %) were purchased from Airgas Inc. (Radnor, PA).

3.2.2.3 Experimental setup and deposition conditions

PFE films were deposited in a six-inch parallel plate radio frequency plasma reactor previously described[47]. *Figure 3.4* shows a schematic of the experimental setup. Omegalux CIR 2015 cartridge heaters (Omega Engineering Inc., Stamford, CT) were used to heat the grounded bottom electrode of the reactor to a temperature of 112 °C. The heating process was monitored with a type K thermocouple controlled by a Syskon RKC temperature controller (RKC Instrument Inc., Southbend, IN). A RF power supply (HF-300, 13.56 MHz, 120 W; ENI Power Systems, Rochester, NY) was used to power the top electrode. This electrode and the power supply were connected with a matching network (Heathkit SA-2060A, Heath Company, Benton Harbor, MI) to minimize reflected power in the plasma system. The pressure in the reactor was controlled with a pressure gauge (Varian Inc., Lexington, MA), and an Alcatel 2063 C rotary vacuum pump (Alcatel, Annecy, France).

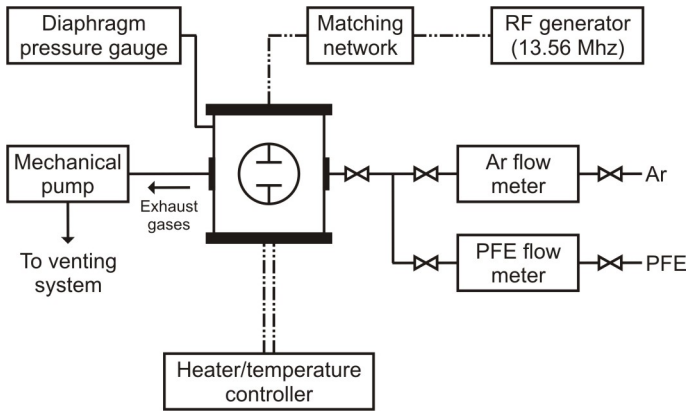

Figure 3.4. Schematic of parallel plate plasma reactor (adapted from[47]).

After placing the sample within the chamber, the plasma reactor was evacuated to a pressure of approx. 20 mTorr. Then oxygen gas was introduced into the chamber (flow rate: 75 standard cm^3 min^{-1}), and the pressure was stabilized to approx. 1 Torr. In order to clean the reactor and sample surface, the oxygen plasma was ignited for 1 min. Following this cleaning procedure, the reactor was re-evacuated to a base pressure of approx. 20 mTorr. For the film deposition, PFE monomer and argon gas were introduced into the reactor (flow rates: 20 and 75 standard cm^3 min^{-1}). The RF generator was activated after the chamber reached a stable pressure of approx. 1 Torr.

3.2.3 Combined AFM-SECM

All atomic force microscopy experiments presented in this thesis were performed with a model 5500 AFM from Agilent Technologies (Chandler, AZ). The 5500 AFM operates in a "top-down" configuration with the AFM probe mounted on the piezo-scanner for imaging of the sample surface. The AFM was placed in a vibration isolation chamber (Agilent Technologies, Chandler, AZ), and additionally in a Faraday cage (home-built) in order to reduce environmental vibration and electromagnetic noise. AFM images were post-processed with the PicoScan 5.3.3 software (Agilent Technologies, Chandler, AZ) for tilt correction or flattening of the image background.

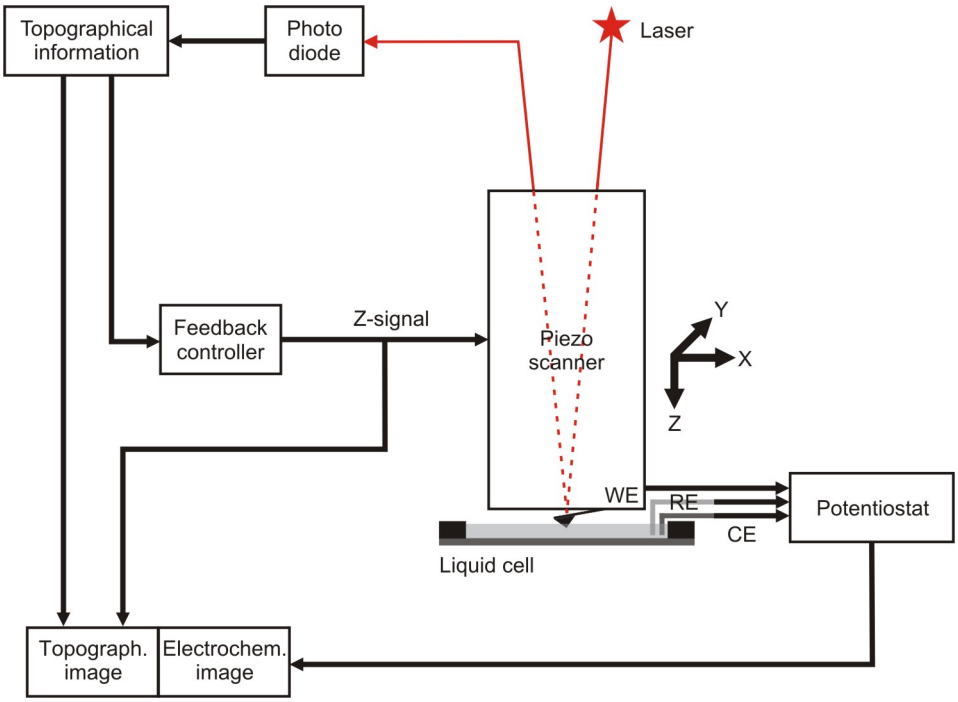

Figure 3.5. Schematic of the combined AFM-SECM set-up based on the 5500 AFM.

Combined AFM-SECM measurements were performed in a liquid cell equipped with a three electrode system. The AFM tip-integrated electrode was serving as the working electrode (WE), a platinum wire was used as a counter electrode (CE), and a freshly chloridized silver wire (Goodfellow, U.K.) served as a reference electrode (RE) (silver quasi-reference electrode, AgQRE). The AgQRE was fabricated by oxidation of the silver wire in 1 M HCl (Aldrich, St. Louis, MO), thereby forming a layer of AgCl. A CHI832A bipotentiostat (CH Instruments Inc., Austin, TX) was utilized for electrochemical measurements. The output signal of the potentiostat was directed into an AD channel of the AFM controller, thereby enabling real-time correlation of the electrochemical data and the topographical image. *Figure 3.5* shows a schematic of the AFM-SECM setup, and *Figure 3.6* a photograph of the system.

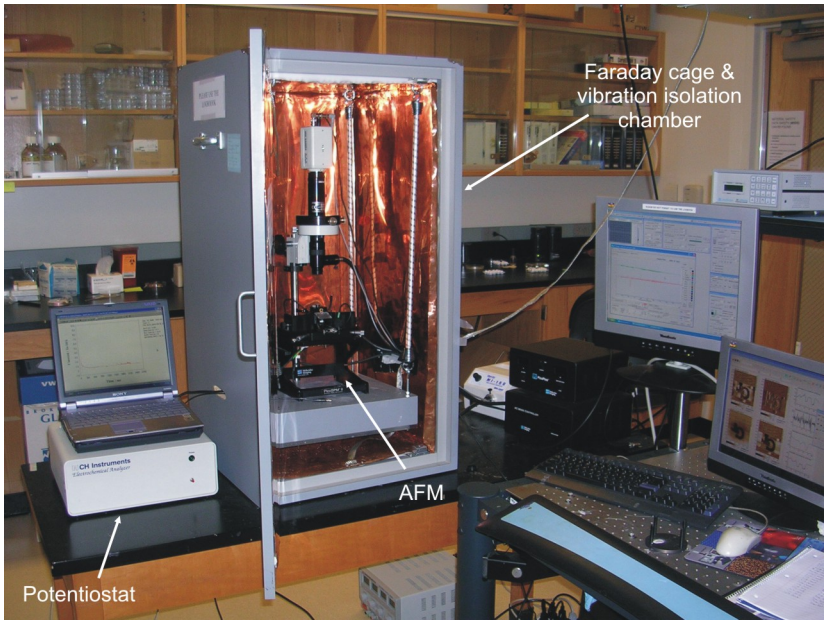

Figure 3.6. Photograph of the AFM-SECM system.

AFM-SECM probes were mounted into modified nose cone assemblies (Agilent Technologies, Chandler, AZ) by either placing or gluing the AFM chip onto the nose cones removing the mounting spring as source for additional electromagnetic interferences. Throughout this thesis, a new approach for contacting AFM-SECM probes in the nose cone was implemented. *Figure 3.7* shows an AFM-SECM probe in a nose cone mounted with the previous approach, and the new approach. It was found that the new approach replacing the spring contacts with direct contacts to the cable and shielded cables (New England Wire Technologies, Lisbon, NH) with SMA connectors (Pasternack, Irvine, CA) yielded a substantial improvement of the experiments. An electrical connection was established between the conducting lines on the AFM-SECM probes and the respective contacts by using two component silver conductive epoxy (H20E Epo-Tek, Tedpella, Redding, CA). Subsequently, the probes and contacts were insulated with insulation varnish (Electrolube, UK).

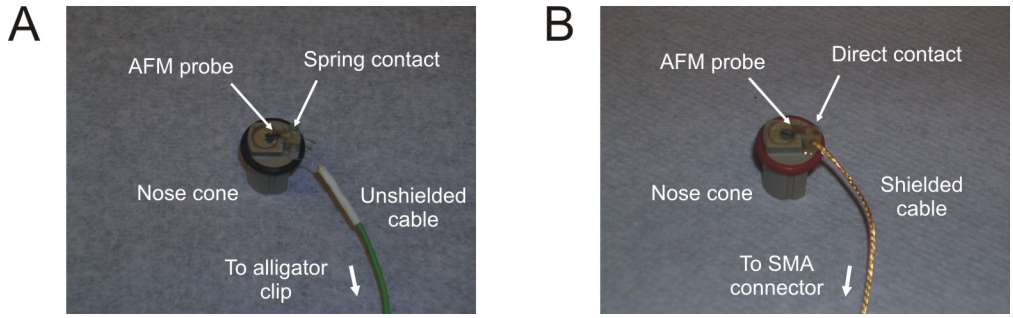

Figure 3.7. Nose cone assemblies showing previous (A) and new approach (B) for mounting AFM-SECM probes.

Alternating conducting/insulating patterned features generated by bitmap-assisted FIB milling served as model samples during AFM-SECM imaging with PFE-coated AFM-SECM probes. Gold-coated (approx. 100 nm) glass slides (VWR, West Chester, PA) with a titanium adhesion layer of approx. 10 nm were used as substrates. *Figure 3.8* shows an exemplary SEM image of FIB-milled patterns representing the Georgia Institute of Technology (GT) logo. After uploading a bitmap of the logo to the FEI software, the gold layer was selectively milled to expose the insulating glass surface (letters of the logo).

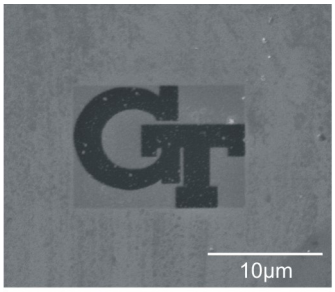

Figure 3.8. SEM image of model substrate generated by bitmap-assisted FIB milling.

3.2.4 Electrochemical characterization

(Bi)potentiostats used throughout this thesis included models CHI660A, CHI842B and CHI832A from CH instruments (Austin, TX). Models CHI660A and CHI842B were both equipped with a Faraday cage and a preamplifier (CH instruments, Austin, TX).

PFE-insulated AFM-SECM probes and gold UMEs were characterized by means of cyclic voltammetry. CVs were recorded in aqueous solutions containing 10 mM potassium ferrocyanide(II) trihydrate ($Fe(CN)_6^{3-/4-}$, Sigma-Aldrich, St. Louis, MO), and 0.5 M potassium chloride (KCl, Sigma-Aldrich, St. Louis, MO) as a supporting electrolyte. The diffusion coefficient for $Fe(CN)_6^{3-/4-}$ in 0.5 M KCl was calculated from limiting steady-state currents obtained from CVs at platinum UMEs (5 µm diameter; Goodfellow, UK). A value of $6.3 \times 10^{-6} \pm 0.1 \times 10^{-6}$ cm^2 s^{-1} was retrieved (n = 3). PFE film stability at AFM-SECM probes was evaluated in long-term studies by measuring CVs in 2 mM ferrocenemethanol ($FeOC_{11}H_{12}$, Sigma-Aldrich, St. Louis, MO) and 0.5 M KCl in increments of 1 - 1.5 hrs for a total time period of 6 hrs. Ethanol (5 % v/v) was added to aqueous $FeOC_{11}H_{12}$ solutions to enhance dissolution. The reference electrode used for general electrochemical studies was a saturated calomel electrode (SCE); potentials are reported vs. this reference electrode.

Simultaneously recorded cantilever deflection and electrochemical approach curves were performed in aqueous 10 mM $Fe(CN)_6^{3-/4-}$ and 0.5 M KCl solutions. The same solutions were used during AFM-SECM imaging experiments recorded in AFM contact mode. The cantilever sensitivity was determined from deflection-distance curves at gold surfaces prior to recording approach curves. All solutions were prepared using deionized water

with a resistance of 18.2 MΩ cm at 25 °C, as provided by a water purification system (Millipore, Billerica, MA).

3.3 Results and discussion

3.3.1 Scanning electron microscopy

Figure 3.9 shows SEM images of PFE-coated AFM-SECM probes and gold microwires after FIB milling. The AFM-SECM probe depicted in *Figure 3.9A* has a PFE layer thickness of approx. 300 nm. *Figure 3.9B* shows the cross-section of a PFE-coated gold microwire. As can be seen from the inset, a smooth microwire cross-section is obtained by FIB milling without affecting the surrounding PFE film. Interestingly, the high resolution SEM image also reveals single crystallites in the polycrystalline gold matrix.

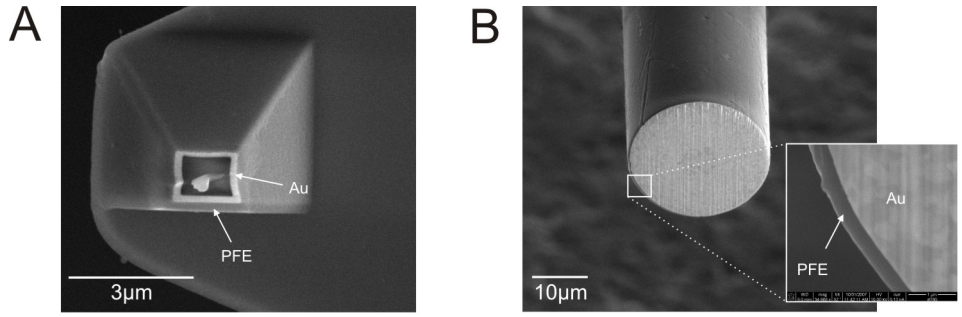

Figure 3.9. SEM images of PFE-coated AFM-SECM probe (A) and gold microwire (B) after exposure of the electroactive area via FIB milling.

The PFE layer thickness at the wire is approx. 400 nm, which is slightly higher than the thickness obtained at the AFM-SECM probes, as the plasma polymerization process is sensitive to minor changes in the process parameters. One of the crucial parameters is the

temperature of the sample during the deposition. Since there is a temperature gradient in the chamber due to the sample distance from the heated electrode, different relative sample positions in the chamber lead to different sample temperatures. Additionally, the curvature of the substrate and orientation of the surface with respect to the ion bombardment direction induce concentration gradients of the neutral species in diffusion-controlled plasma processes. These factors indicate that samples of different shapes and materials have dissimilar exposure to the plasma polymerization, which leads to the observed variations in PFE layer thickness at different samples coated in the same deposition run.

3.3.2 Electrochemical characterization

Cyclic voltammetry was used for electrochemical characterization of PFE-coated AFM-SECM probes and UMEs, since the dimensions of the electroactive area may be retrieved from the magnitude of the limiting steady-state current. Additionally, the shape of the CV and magnitude of the charging current contribution may reveal information about the quality of the insulation layer.

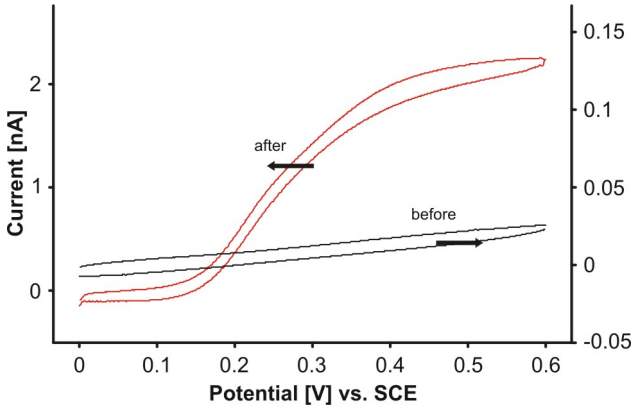

Figure 3.10. CVs obtained at PFE-coated AFM-SECM probe before and after FIB milling in 10 mM $Fe(CN)_6^{3-/4-}$ solution containing 0.5 M KCl (scan rates 0.05 and 0.1 V s^{-1}). The frame edge length was approx. 1.28 µm.

Figure 3.10 shows CVs obtained at a PFE-coated AFM-SECM probe before and after the exposure of the tip-integrated electrode by FIB milling. No faradaic contributions in the CV prior to the FIB modification are measured, and only minor charging currents (approx. 8 pA) are observed indicating excellent insulating properties of the PFE layer. Although the steady-state current response at frame electrodes was previously described with numerical simulations[52], no simple equations are available for predicting the response unlike for other conventional electrode designs. Faradaic currents at AFM tip-integrated frame electrodes have been previously approximated utilizing analytical expressions derived for ring electrodes[2], which are described in *Section 2.1.2*. Using *Equations (2.7) - (2.9)*, and the electrode dimensions obtained from SEM images (frame edge length approx. 1.28 µm, frame thickness approx. 0.15 µm) a theoretical current value of 1.4 nA was obtained, which is close to the experimentally obtained value of 2.3 nA. The discrepancy observed may be attributed to the fact that the assumed ring geometry does not consider high current density effects, which may originate from sharp corners at frame electrodes.

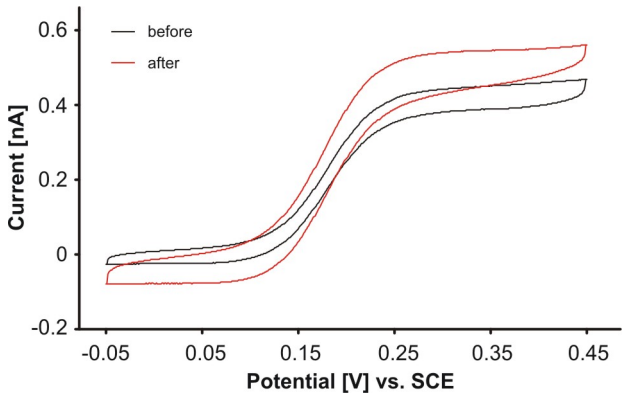

Figure 3.11. CVs obtained before and after the time study in 2 mM $FeOC_{11}H_{12}$ solution containing 0.5 M KCl as supporting electrolyte (scan rate 0.02 V s^{-1}). The length of the electrode frame was approx. 1.4 µm.

Cyclic voltammetry over extended exposure periods was utilized to evaluate the long-term stability of PFE insulation layers in solution, since it is known from electrochemical STM probes that insulation materials other than glass frequently do not exhibit ideal temporal stability. PFE-insulated AFM-SECM probes were soaked in $FeOC_{11}H_{12}$ solution, and CVs were recorded in increments of 1-1.5 hrs over a total time period of 6 hrs. Exemplary CVs obtained before starting the study and after this time period are shown in *Figure 3.11*. Although there is a minor increase in steady-state current of approx. 20 %, the overall shape of the CV remains essentially unaltered. Given that standard AFM-SECM imaging experiments usually last approx. 2 - 3 hrs, the long-term stability of the probes is sufficient for such experiments. Hence, PFE layers present an attractive approach to thin film insulation membranes for AFM tip-integrated electrodes.

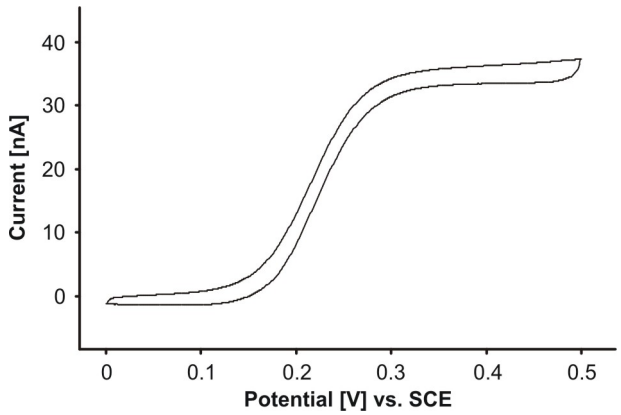

Figure 3.12. CV of a PFE-insulated gold UME after exposure of the electroactive area by FIB milling recorded in 10 mM $Fe(CN)_6^{3-/4-}$ solution containing 0.5 M KCl (scan rate 0.02 V s^{-1}).

Additionally, it could be demonstrated that plasma-polymerized PFE layers are a versatile insulation method since they can be applied to gold microwires and gold UMEs. This is of potential interest, as UMEs with thin and flexible insulation layers are relevant to physiological applications. As demonstrated in *Figure 3.9B*, the electroactive cross-section of the microwires was exposed using FIB milling. *Figure 3.12* shows a CV obtained at such a PFE-coated UME. The observed steady-state current (36.0 nA) matches in magnitude with the predicted value of 32.2 nA corresponding to an electrode diameter of 25 µm.

3.3.3 Approach curves

Deflection and current approach curves were simultaneously recorded with PFE-insulated AFM-SECM probes at conducting (gold) and insulating (glass) surface features. *Figure 3.13* shows representative results obtained during these experiments. The current is plotted as normalized current corresponding to the steady-state current recorded at the electrode while approaching to the substrate surface normalized by the current measured

in bulk solution. Since the AFM operates in a "top-down" configuration, the AFM sample stage has to be approached to the tip in discrete steps (step-size: 400 nm) to engage the AFM probe at the surface prior to imaging. In order to probe the distance to the surface, the piezo-scanner is moved in z-direction after every step. If there is a cantilever deflection detected, the AFM feedback mechanism is activated; otherwise, the stage is further approached. Due to the short periodicity of these steps, the tip-sample distance plotted in *Figure 3.13* is an approximation derived from a time-signal curve, and the total traveled distance. To convert the cantilever deflection signal from volts into nm, the cantilever sensitivity was determined by recording deflection-distance curves at the gold surface directly prior to the measurement of the approach curves. The slope of the deflection-distance curve in the contact region was used for calibration of the cantilever sensitivity.

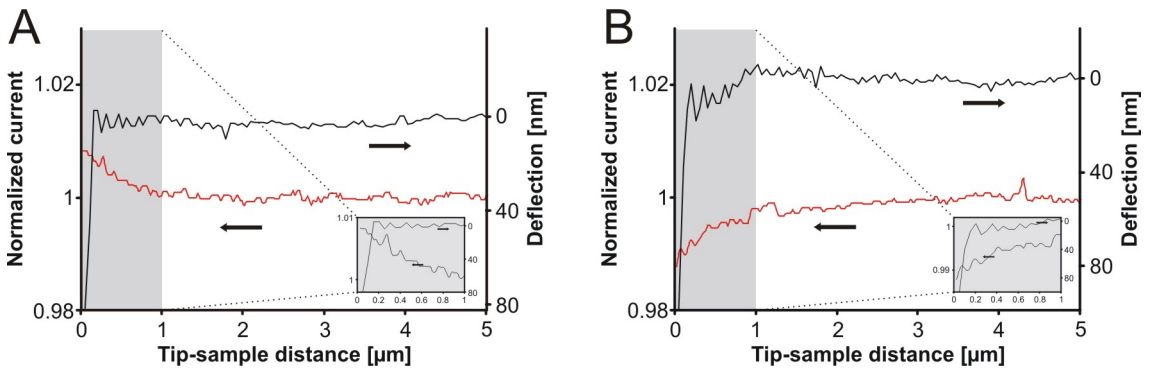

Figure 3.13. Simultaneously recorded approach-cantilever deflection curves measured with a PFE-coated AFM-SECM probe. Positive feedback (A) is observed at a gold surface and negative feedback (B) at a glass surface. Curve sections close to the sample surface are magnified in the insets shown in (A) and (B). The tip-integrated electrode was biased at 0.6 V (vs. AgQRE) in 10 mM $Fe(CN)_6^{3-/4-}$ and 0.5 M KCl. The tip-integrated frame electrode had an edge length of approx. 1.6 µm and the tip height was approx. 0.54 µm.

The AFM tip-integrated electrode was biased at 0.6 V for oxidation of the redox mediator. The normalized current recorded while approaching conducting and insulating surfaces shows the behavior expected from SECM theory. Conducting surface features lead to a recycling of the redox mediator, as it is locally reduced at the gold surface, which is detectable as a current increase (positive feedback, *Figure 3.13A*). Accordingly, a decreased current (negative feedback) is observed in the vicinity of the insulating features due to hindered diffusion of the mediator to the tip-integrated electrode, and a lack of this recycling effect (*Figure 3.13B*). Additionally, rapid cantilever deflection is observed for both cases at the surface coinciding with the detected current changes.

3.3.4 AFM-SECM imaging

Simultaneous AFM-SECM images were obtained with PFE-coated AFM-SECM probes at a FIB-patterned substrate. The sample was patterned from a gold-coated glass slide such that insulating (glass) and conducting (gold) features were exposed (see *Section 3.2.3*).

Similar to results obtained during combined approach-deflection curves (*Figure 3.13*), the AFM tip-integrated electrode was biased at 0.6 V, and scanned across the surface of the FIB-milled pattern. The topography was recorded in AFM contact mode, while monitoring the anodic steady-state current at the electrode in SECM feedback mode. *Figure 3.14* shows an exemplary set of images obtained during such an experiment. Positive feedback was observed at the elevated conducting gold features of the surface resulting in a current increase, whereas negative feedback was detected at the milled sections exposing the insulating glass as a decreased current. Again, the SECM feedback experiment revealed the expected behavior. Moreover, conducting and insulating current

features coincide well with the simultaneously recorded topography. *Figure 3.14C* shows a cross-sectional view of the line scan marked with an asterisk in *Figure 3.14A* and *B*. The topographical cross-section reveals a thin strip of gold (approx. 400 nm wide) between the letters "G" and "T", which is clearly evident in the corresponding current image as an elevated current feature. This observation demonstrates excellent electrochemical resolution obtained with such AFM-SECM probes.

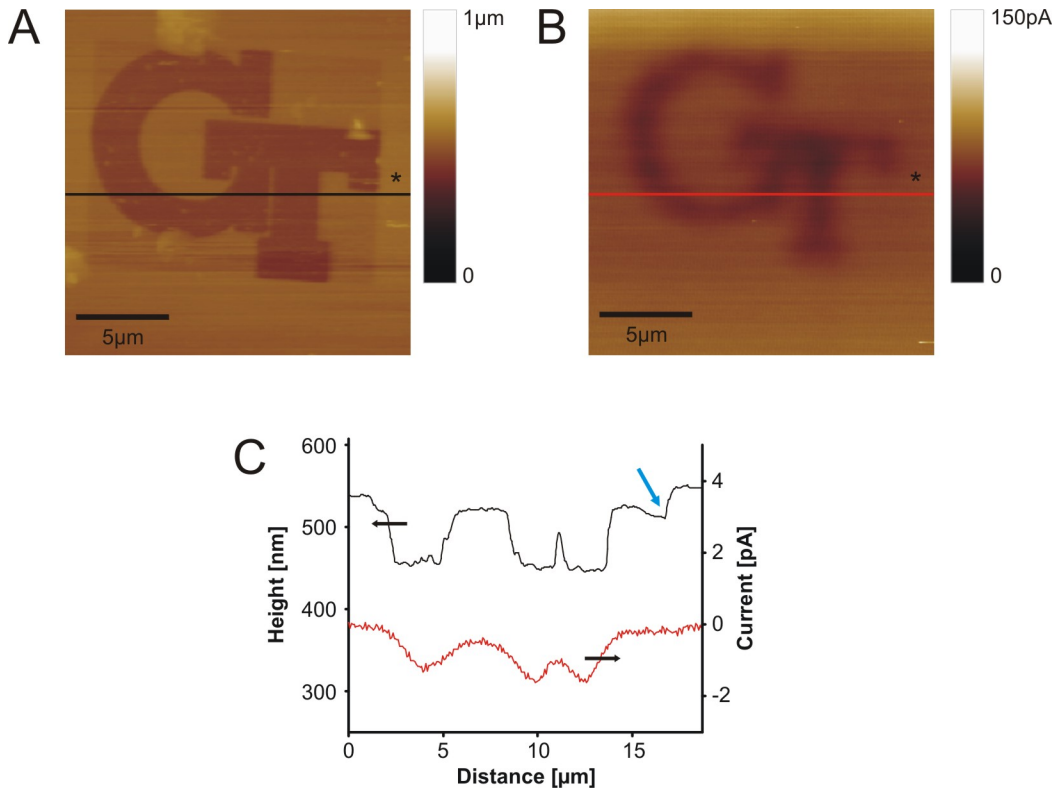

Figure 3.14. Simultaneous AFM-SECM imaging at FIB-patterned substrate showing topography (A), and current (B) images. The lines in (A) and (B) mark the line scan presented in the cross-sectional views (C). The bifunctional AFM-SECM probe was scanned in contact mode at a rate of 0.36 lines s^{-1} (original scan size: 25 × 25 µm^2), and biased at 0.6 V (vs. AgQRE) to oxidize $Fe(CN)_6^{3-/4-}$ (10 mM in 0.5 M KCl). The tip-integrated frame electrode had an edge length of approx. 1.6 µm and the tip height was approx. 0.54 µm.

One of the strengths of combined AFM-SECM imaging with tip-integrated electrodes, which are recessed from the apex of the tip, is the deconvolution of the electrochemical and the topographical signal due to the constant tip-sample distance. In conventional constant-height SECM, the distance between the electrode and the surface may be altered due to morphological features leading to current changes, which cannot be exclusively attributed to a change in electrochemical activity[53]. This behavior may also be observed in the conducted experiment. It can be noted in *Figure 3.14A* that patterning of the GT logo resulted in a slight rectangular recess around the two letters due to milling of the gold surface. Consequently, a step is observed in the cross-sectional view of the height profile (marked with a blue arrow in *Figure 3.14C*). Deconvolution of current and topography is confirmed, since the corresponding cross-section of the current image does not show any evident current change.

3.4 Final remarks

Plasma-polymerized PFE layers were evaluated for applicability as novel thin film insulation membranes at bifunctional AFM-SECM probes and UMEs. Electrochemical characterization of bifunctional AFM-SECM probes revealed excellent insulating properties of the PFE membrane. After exposure of tip-integrated electrodes, well-defined CVs and appropriate steady-state current levels were obtained. Although the long-term performance study revealed an increase of 20 % in steady-state current after a time period of 6 hrs, the PFE layer time stability proves sufficient due to a 2 – 3 hrs time period required for conventional AFM-SECM imaging experiments. Plasma-polymerized insulation layers are also applicable for the insulation of microwires leading to flexible

gold UMEs. Simultaneously recorded SECM approach-cantilever deflection curves were obtained demonstrating positive/negative feedback effects depending on surface sample properties. Additionally, successful AFM-SECM imaging was performed at a FIB-patterned substrate leading to current variations expected from SECM feedback theory while revealing excellent electrochemical resolution.

By using the strategy proposed in this chapter, insulating films with a thickness of < 300 nm could be achieved. When compared to silicon nitride/silicon oxide or Parylene C insulation layers, this corresponds to a 2 – 3 x decrease in thickness of the insulation layer. Future work to enhance the long-term stability of the PFE-insulated probes should focus on an improvement of PFE layer adhesion by optimization of the oxygen plasma cleaning step prior to the deposition. Since the charging current revealed an increase after the time study indicating enhanced partitioning of the electrolyte into the insulation layer, further optimization should also focus on increasing the cross-linking density of the layer.

3.5 References

(1) Zoski, C. G.; Mirkin, M. V. *Steady-State Limiting Currents at Finite Conical Microelectrodes*, Anal. Chem. **2002**, *74*, 1986-1992.

(2) Kranz, C.; Friedbacher, G.; Mizaikoff, B.; Lugstein, A.; Smoliner, J.; Bertagnolli, E. *Integrating an Ultramicroelectrode in an AFM Cantilever: Combined Technology for Enhanced Information*, Anal. Chem. **2001**, *73*, 2491-2500.

(3) Lugstein, A.; Bertagnolli, E.; Kranz, C.; Kueng, A.; Mizaikoff, B. *Integrating micro- and nanoelectrodes into atomic force microscopy cantilevers using focused ion beam techniques*, Appl. Phys. Lett. **2002**, *81*, 349-351.

(4) Kueng, A.; Kranz, C.; Mizaikoff, B.; Lugstein, A.; Bertagnolli, E. *Combined scanning electrochemical atomic force microscopy for tapping mode imaging*, Appl. Phys. Lett. **2003**, *82*, 1592-1594.

(5) Heintz, E. L. H.; Kranz, C.; Mizaikoff, B.; Noh, H.-S.; Hesketz, P.; Lugstein, A.; Bertagnolli, E. *Proceedings of the 2001 1st IEEE Conference on Nanotechnology. IEEE-NANO 2001 (Cat. No.01EX516)*, Maui, HI, USA, 2001// 2001; IEEE; 346-351.

(6) Fan, F. R. F.; Demaille, C. *The preparation of tips for Scanning Electrochemical Microscopy*, In *Scanning Electrochemical Microscopy*; Bard, A. J., Mirkin, M. V., Eds.; Marcel Dekker, Inc.: New York, 2001, pp 75-110.

(7) Zoski, C. G. *Ultramicroelectrodes: design, fabrication, and characterization*, Electroanalysis **2002**, *14*, 1041-1051.

(8) Wightman, R. M.; Wipf, D. O. *Voltammetry at Ultramicroelectrodes*, In *Electroanal. Chem.*; Bard, A. J., Ed.; Marcel Dekker, Inc.: New York, 1989; Vol. 15, pp 267-353.

(9) Fleischmann, M.; Pons, S.; Rolison, D. R.; Schmidt, P. P. *Ultramicroelectrodes*, Datatech Systems: Inc. , S., 226-238.

(10) Nagahara, L. A.; Thundat, T.; Lindsay, S. M. *Preparation and characterization of STM tips for electrochemical studies*, Rev. Sci. Instrum. **1989**, *60*, 3128-3130.

(11) Loeb, G. E.; Peck, R. A.; Martyniuk, J. *Toward the ultimate metal microelectrode*, J. Neurosci. Meth. **1995**, *63*, 175-183.

(12) Potje-Kamloth, K.; Janata, J.; Josowicz, M. *Electrochemically prepared insulation for carbon fiber microelectrodes*, Ber. Bunsen-Ges. Phys. Chem. **1989**, *93*, 1480-1485.

(13) Zhang, X.; Ogorevc, B. *Poly(tetrafluoroethylene) Film Housing of Carbon Fibers Using Capillary-Pull Technology for One-Stage Fabrication of Carbon Disk Ultramicroelectrodes and Their Characterization*, Anal. Chem. **1998**, *70*, 1646-1651.

(14) Koh, D.-S.; Hille, B. *Rapid fabrication of plastic-insulated carbon-fiber electrodes for micro-amperometry*, J. Neurosci. Meth. **1999**, *88*, 83-91.

(15) Liu, B.; Rolland, J. P.; DeSimone, J. M.; Bard, A. J. *Fabrication of Ultramicroelectrodes Using A "Teflon-like" Coating Material*, Anal. Chem. **2005**, *77*, 3013-3017.

(16) El-Deen, E.; El-Giar, M.; Wipf, D. O. *Preparation of tip-protected poly(oxyphenylene) coated carbon-fiber ultramicroelectrodes*, Electroanalysis **2006**, *18*, 2281-2289.

(17) Schulte, A.; Chow, R. H. *A Simple Method for Insulating Disk-Shaped Carbon-Fiber Microelectrodes Using Anodic Electrophoretic Deposition of Paint*, Anal. Chem. **1996**, *68*, 3054-3058.

(18) Slevin, C. J.; Gray, N. J.; Macpherson, J. V.; Webb, M. A.; Unwin, P. R. *Fabrication and characterization of nanometer-sized platinum electrodes for voltammetric analysis and imaging*, Electrochem. Commun. **1999**, *1*, 282-288.

(19) Penner, R. M.; Heben, M. J.; Lewis, N. S. *Preparation and electrochemical characterization of conical and hemispherical ultramicroelectrodes*, Anal. Chem. **1989**, *61*, 1630-1636.

(20) Zhang, B.; Wang, E. *Fabrication of STM tips with controlled geometry by electrochemical etching and ECSTM tips coated with paraffin*, Electrochim. Acta **1994**, *39*, 103-106.

(21) Qiao, Y.; Chen, J.; Guo, X.; Cantrell, D.; Ruoff, R.; Troy, J. *Fabrication of nanoelectrodes for neurophysiology: cathodic electrophoretic paint insulation and focused ion beam milling*, Nanotechnology **2005**, *16*, 1598-1602.

(22) Schwank, M.; Muller, U.; Hauert, R.; Rossi, R.; Volkert, M.; Wintermantel, E. *Production of a microelectrode for intracellular potential measurements based on a Pt/Ir needle insulated with amorphous hydrogenated carbon*, Sens. Actuators, B **1999**, *B56*, 6-14.

(23) Bach, C. E.; Nichols, R. J.; Beckmann, W.; Meyer, H.; Schulte, A.; Besenhard, J. O.; Jannakoudakis, P. D. *Effective insulation of scanning tunneling microscopy tips for electrochemical studies using an electropainting method*, J. Electrochem. Soc. **1993**, *140*, 1281-1284.

(24) Strein, T. G.; Ewing, A. G. *Characterization of submicron-sized carbon electrodes insulated with a phenol-allylphenol copolymer*, Anal. Chem. **1992**, *64*, 1368-1373.

(25) Lambie, B. A.; Orwar, O.; Weber, S. G. *Controlling the Electrochemically Active Area of Carbon Fiber Microelectrodes by the Electrodeposition and Selective Removal of an Insulating Photoresist*, Anal. Chem. **2006**, *78*, 5165-5171.

(26) Vitus, C. M.; Chang, S. C.; Schardt, B. C.; Weaver, M. J. *In situ scanning tunneling microscopy as a probe of adsorbate-induced reconstruction at ordered monocrystalline electrodes: carbon monoxide on platinum(100)*, J. Phys. Chem. **1991**, *95*, 7559-7563.

(27) Gewirth, A. A.; Craston, D. H.; Bard, A. J. *Fabrication and characterization of microtips for in situ scanning tunneling microscopy*, J. Electroanal. Chem. **1989**, *261*, 477-482.

(28) Mirkin, M. V.; Fan, F. R. F.; Bard, A. J. *Scanning electrochemical microscopy. Part 13. Evaluation of the tip shapes of nanometer size microelectrodes*, J. Electroanal. Chem. **1992**, *328*, 47-62.

(29) Gray, N. J.; Unwin, P. R. *Simple procedure for the fabrication of silver/silver chloride potentiometric electrodes with micrometer and smaller dimensions: application to scanning electrochemical microscopy*, Analyst **2000**, *125*, 889-893.

(30) Chen, S.; Kucernak, A. *The Voltammetric Response of Nanometer-Sized Carbon Electrodes*, J. Phys. Chem. B **2002**, *106*, 9396-9404.

(31) Abbou, J.; Demaille, C.; Druet, M.; Moiroux, J. *Fabrication of Submicrometer-Sized Gold Electrodes of Controlled Geometry for Scanning Electrochemical-Atomic Force Microscopy*, Anal. Chem. **2002**, *74*, 6355-6363.

(32) Chen, S.; Kucernak, A. *Fabrication of carbon microelectrodes with an effective radius of 1 nm*, Electrochem. Commun. **2002**, *4*, 80-85.

(33) Macpherson, J. V.; Unwin, P. R. *Combined Scanning Electrochemical-Atomic Force Microscopy*, Anal. Chem. **2000**, *72*, 276-285.

(34) Conyers, J. L., Jr.; White, H. S. *Electrochemical Characterization of Electrodes with Submicrometer Dimensions*, Anal. Chem. **2000**, *72*, 4441-4446.

(35) Lee, Y.; Bard, A. J. *Fabrication and Characterization of Probes for Combined Scanning Electrochemical/Optical Microscopy Experiments*, Anal. Chem. **2002**, *74*, 3626-3633.

(36) Abe, T.; Itaya, K.; Uchida, I. *An electrochemical fabrication method for gold and carbon ultramicroelectrode*, Chem. Lett. **1988**, 399-402.

(37) Lee, B.-J.; Kim, H.-G.; Lee, D.-C. *Electrical properties of polyimide thin films formed by the vapor deposition polymerization method*, Surf. Coat. Technol. **2002**, *150*, 182-187.

(38) Biloiu, C.; Biloiu, I. A.; Sakai, Y.; Sugawara, H.; Ohta, A. *Amorphous fluorocarbon polymer (a-C:F) films obtained by plasma enhanced chemical vapor deposition from perfluoro-octane (C8F18) vapor. II. Dielectric and insulating properties*, J. Vac. Sci. Technol., A **2004**, *22*, 1158-1165.

(39) Loeb, G. E.; Bak, M. J.; Salcman, M.; Schmidt, E. M. *Parylene as a chronically stable, reproducible microelectrode insulator*, IEEE Trans. Biomed. Eng. **1977**, *BME-24*, 121-128.

(40) Noordegraaf, J. *Conformal coating using parylene polymers*, Med. Device Technol. **1997**, *8*, 14-20.

(41) Takahashi, Y.; Iijima, M.; Inagawa, K.; Itoh, A. *Synthesis of aromatic polyimide film by vacuum deposition polymerization*, J. Vac. Sci. Technol., A **1987**, *5*, 2253-2256.

(42) Kagami, Y.; Yamauchi, T.; Osada, Y.; Yoshizawa, I. *Preparation, structure, and electric properties of plasma-polymerized titanium-containing organic thin films*, J. Appl. Phys. **1990**, *68*, 610-616.

(43) Vaswani, S.; Koskinen, J.; Hess, D. W. *Surface modification of paper and cellulose by plasma-assisted deposition of fluorocarbon films*, Surf. Coat. Technol. **2005**, *195*, 121-129.

(44) Tamirisa, P. A.; Koskinen, J.; Hess, D. W. *Plasma polymerized hydrogel thin films*, Thin Solid Films **2006**, *515*, 2618-2624.

(45) Shi, F. F. *Recent advances in polymer thin films prepared by plasma polymerization. Synthesis, structural characterization, properties and applications*, Surf. Coat. Technol. **1996**, *82*, 1-15.

(46) Biederman, H., Ed. *Plasma polymer films*; Imperial College Press: London, 2004.

(47) Dobbs, G. T.; Balu, B.; Young, C.; Kranz, C.; Hess, D. W.; Mizaikoff, B. *Mid-Infrared Chemical Sensors Utilizing Plasma-Deposited Fluorocarbon Membranes*, Anal. Chem. **2007**, *79*, 9566-9571.

(48) Agraharam, S.; Hess, D. W.; Kohl, P. A.; Bidstrup Allen, S. A. *Thermal stability of fluorocarbon films deposited from pentafluoroethane/argon plasmas*, J. Electrochem. Soc. **2000**, *147*, 2665-2670.

(49) Agraharam, S.; Hess, D. W.; Kohl, P. A.; Bidstrup Allen, S. A. *Electrical properties and temperature-humidity studies of fluorocarbon films deposited from pentafluoroethane/argon plasmas*, J. Electrochem. Soc. **2001**, *148*, F102-F107.

(50) Agraharam, S.; Hess, D. W.; Kohl, P. A.; Bidstrup Allen, S. A. *Plasma chemistry in fluorocarbon film deposition from pentafluoroethane/argon mixtures*, J. Vac. Sci. Technol., A **1999**, *17*, 3265-3271.

(51) Jansen, H. V.; Gardeniers, J. G. E.; Elders, J.; Tilmans, H. A. C.; Elwenspoek, M. *Applications of fluorocarbon polymers in micromechanics and micromachining*, Sens. Actuators, A **1994**, *41*, 136-140.

(52) Sklyar, O.; Kueng, A.; Kranz, C.; Mizaikoff, B.; Lugstein, A.; Bertagnolli, E.; Wittstock, G. *Numerical Simulation of Scanning Electrochemical Microscopy Experiments with Frame-Shaped Integrated Atomic Force Microscopy-SECM Probes Using the Boundary Element Method*, Anal. Chem. **2005**, *77*, 764-771.

(53) Hengstenberg, A.; Kranz, C.; Schuhmann, W. *Facilitated tip-positioning and applications of non-electrode tips in scanning electrochemical microscopy using a shear force based constant-distance mode*, Chem.--Eur. J. **2000**, *6*, 1547-1554.

4 ION BEAM INDUCED DEPOSITION OF PLATINUM CARBON COMPOSITE MATERIALS FOR LOCALIZED PATTERNING OF UMES

Platinum carbon composite materials obtained by ion beam induced deposition for the localized patterning of electrodes at UMEs and AFM-SECM probes are introduced in this chapter. Physical and electrochemical properties of pristine composites are evaluated. In addition, treatment procedures are described focusing on the decrease of the carbon content within the deposits.

4.1 Motivation

The geometric dimension of the integrated electrode in AFM-SECM technology is a critical requirement, as it predominantly determines the resolution in electrochemical imaging. From that perspective, small electrode dimensions are an attractive feature. However, measurements with small electrodes in the nm dimension typically result in signals in the low pA to fA region, which are frequently accompanied by undesirable signal-to-noise ratios. In addition, if these small electrodes are employed as transducer for the design of tip-integrated biosensors, only a small amount of biomolecules may be immobilized. From a biosensing perspective, electrodes with larger surface area are thus preferable requiring a balance between the electrochemical resolution and the electrode dimensions.

In case of recessed electrodes integrated in AFM-SECM probes based on commercial AFM probes, the thickness of sputtered gold electrodes is limited due to resulting bending of the cantilevers at metal thicknesses exceeding 150 - 200 nm. Hence, other strategies have to be pursued in order to increase the electroactive area for integrated biosensors. One approach, which was initially pursued, involved electroplating gold onto AFM-SECM probes (*Figure 4.1*). However, electroplating of gold led to thick electrode layers that would interfere with the sample surface during AFM imaging. Furthermore, the resulting electrode geometry and dimensions were irreproducible between individual depositions.

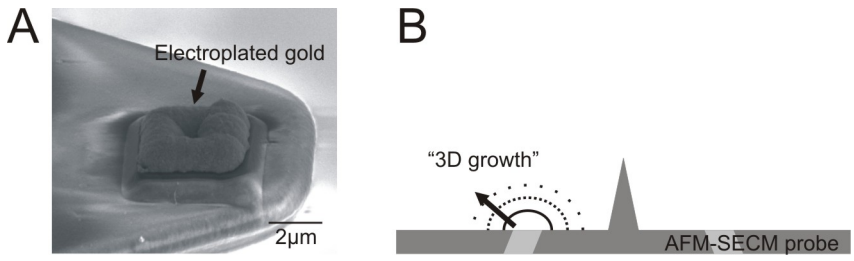

Figure 4.1. (A) SEM image of Au layer electroplated on AFM-SECM probe. (B) Schematic 3D growth process showing cross-section of AFM-SECM probe.

Another possibility is ion beam induced deposition, which offers the capability to pattern thin conducting layers with high spatial resolution, and with a user-defined shape. One focus of this thesis was to evaluate IBID as a possibility for increasing the tip-integrated electrode area by localized patterning of electrode materials without significantly decreasing the localization power of the SECM measurement.

4.1.1 Ion beam induced deposition

IBID of materials is a mask-less micro-fabrication technique that can be used for a variety of applications in micro- and nanoengineering including nanowire growth[1-3], fabrication of miniature electrical contacts[4-7], formation of three-dimensional structures[8-10], and repair of X-ray masks and microelectronic circuits[8, 11]. During the deposition process, a precursor is vaporized into a high vacuum environment in the vicinity of a substrate. Precursor molecules adsorbed to the sample surface are dissociated into smaller chemical structures and individual elemental constituents by exposing the surface to a focused ion beam. The IBID process can be understood as a localized chemical vapor deposition process, whereby the interaction of incident ions, sputtered material, and secondary electrons with the precursor causes fragmentation and formation of volatile and non-volatile species (*Figure 4.2*). The volatile fragments leave the surface, and are eventually removed by the vacuum, whereas non-volatile fragments form three-dimensional structures at the sample surface with a geometry controlled by the selected pattern. Besides fabrication of conducting materials, materials with electrically insulating properties may be deposited leading to a wide range of applications[12, 13].

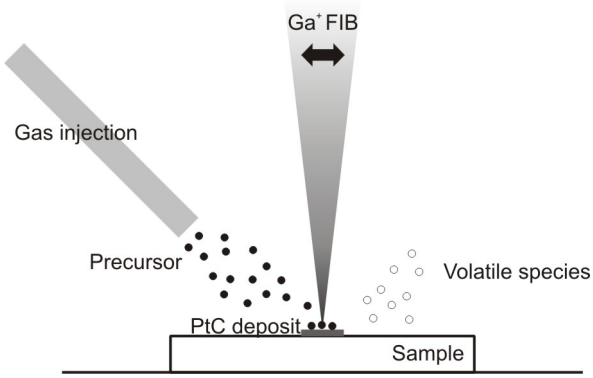

Figure 4.2. Schematic of the IBID process.

Alternatively, electron beam induced deposition (EBID), where an electron beam fragments the precursor, has been used to generate microstructures similar to those attained with IBID[14-16]. The main advantages of EBID over IBID are that no damage is imparted to the sample induced by heavy ions incident at the surface, and that no material incorporation occurs, as evident with the ion beam. However, IBID generally yields higher metal content due to a larger dissociation cross-section, higher ionic mass, sputtering yield of light atoms, shorter penetration depths, and beam-induced self-heating effects[17].

Since the initial studies by Tao et al., the most frequently used organometallic precursor for the deposition of platinum composites has been methylcyclopentadienyl [trimethyl] platinum ($C_9H_{16}Pt$)[11, 18]. The material formed during the decomposition process includes a substantial amount of carbon impurities due to the organometallic nature of the precursor. Additionally, gallium ions are implanted in the matrix as a second contaminant, since a focused gallium ion beam is used during IBID. Platinum fractions varying from 15 atomic% (at%) to 50 at% are reported in literature depending upon the deposition conditions[7, 19, 20]. Generally, gallium is present at lower concentration (5 at%

to 18 at%), and considered to improve the conductivity of the deposit[7, 20]. Applications requiring high electrical conductivity have focused on removal of the incorporated carbon to improve the electrical properties of the composite material. Several strategies for carbon removal in metal composites have been described in literature for both IBID and EBID techniques. These include in-situ annealing[21, 22], post-deposition annealing[23], depositions in reactive environments[14, 24], and the utilization of carbon-free precursor species[25, 26]. Alternatively, post-treatment steps have been reported, where a change of the microstructure leads to a reduction of the resistivity[27].

4.2 Experimental

4.2.1 Ion beam induced deposition

Ion beam induced structured depositions of platinum carbon composites, and SEM analyses were performed with a FEI Quanta™ 200 3D DualBeam™ (FIB/SEM) system (FEI Company, Hillsboro, OR). The organic precursor (methylcyclopentadienyl [trimethyl] platinum, $C_9H_{16}Pt$) used for depositions was heated to 39 °C, and evaporated into the vacuum chamber through a gas injection system. Ion beam parameters applied for depositions were a dwell time of 200 ns and a relative interaction diameter of 150 % (beam overlap of 0 %). Deposits used to calibrate the growth rate by AFM analysis were prepared on silicon wafers (CZ, <100>, pp+, epitaxial wafers; Siltronic, Germany) at varying deposition times and beam currents with the targeted pattern size for the respective samples.

The targeted dimension for all patterns analyzed by energy dispersive X-ray spectroscopy (EDX) was a square-shaped cuboid with a height of 1.1 µm and a base of 8 μm^2

($2.83 \times 2.83\ \mu m^2$) deposited on silicon wafers. PtC deposits for initial EDX studies were deposited at varying ion beam currents (from 10 - 500 pA), or at a fixed ion beam current (100 pA) for EDX studies at different pattern thicknesses, respectively. An ion beam current of 100 pA was also used for fabrication of IBID patterns used in EDX annealing studies. The same samples were additionally characterized in high-resolution dynamic mode AFM imaging.

Two types of PtC patterns were analyzed by Raman spectroscopy. One set of samples involved the ion beam current variation studies (from 10 - 500 pA), and had a targeted dimension of $5.66 \times 5.66\ \mu m^2$ with a thickness of 100 nm consisting of four square shaped sub-patterns of approx. $8\ \mu m^2$ each. Samples used for annealing studies were prepared at identical conditions as the samples used during EDX studies (square-shaped cuboid: targeted height 1.1 µm, base $8\ \mu m^2$; ion beam current: 100 pA).

Four-point probe (FPP) measurements were performed at PtC deposits with rectangular cuboid shapes (targeted height 200 nm, base $8 \times 1\ \mu m^2$) deposited at varying ion beam currents (from 10 - 500 pA). Patterned PtC lines were used to connect these deposits to micro-fabricated platinum contacts, which were sputtered at a thickness of approx. 400 nm on a silicon oxide passivated silicon wafer (approx. 1.2 µm silicon oxide, and a sputtered chromium adhesion layer of approx. 30 nm prior to platinum deposition).

All AFM-SECM probes used throughout this chapter were fabricated by FIB milling as described in *Section 3.2.1*. PtC electrodes deposited at AFM-SECM probes were frame-shaped (total target area of $8\ \mu m^2$; consisting of two sub-patterns with $1 \times 1\ \mu m^2$ and two sub-patterns with $3 \times 1\ \mu m^2$, respectively) with a target thickness of 100 nm (ion beam current: 30 pA). For electrochemical characterization and annealing studies, circular PtC

layers were deposited at 5 µm platinum UMEs with a targeted diameter of 8 µm and a targeted thickness of 100 nm (ion beam current: 100 pA). A larger diameter of PtC deposits was used in order to ensure full coverage of the platinum wire cross-section.

4.2.2 PtC treatment procedures

Three different types of post-treatments for PtC patterns were evaluated for purification of the composite material, since it was found that an increased amount of platinum in the layer is desired for improved electrochemical behavior of the electrode. Annealing of the samples was performed in a home build aluminum furnace (*Figure 4.3*). The furnace consists of two cartridge heaters (model CIR-20207, Chromalox, Pittsburgh, PA) connected to a variable transformer (Staco Energy Products Co., Dayton, OH). The temperature inside the furnace was monitored with a type k thermocouple before and after each annealing step, and typically showed constant values with a variation of ± 2 °C. The furnace was heated to the required temperatures in the range of 100 to 550 ºC depending on the respective experiment and each annealing step was performed for 11 min. The first minute involved placement and equilibration of the samples, and the following 10 min was the annealing time adapted from Botman et al.[23].

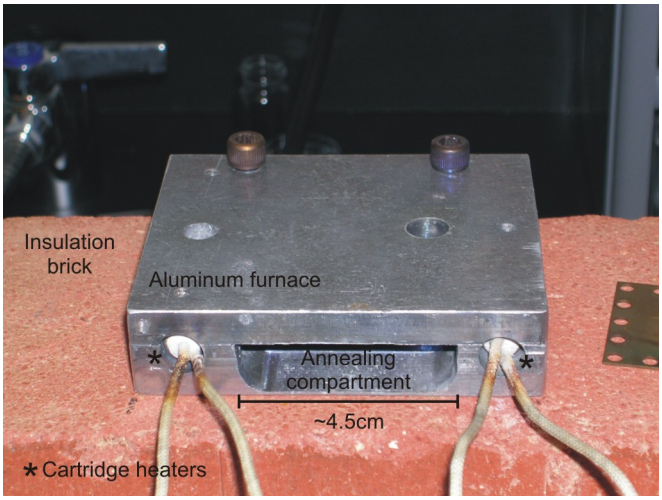

Figure 4.3. Photograph of the home-built aluminum furnace.

UV/ozone treatments were performed in the same UV/ozone chamber described in *Section 3.2.2*. Different types of UV/ozone treatments were used including repetitive 30 min treatment intervals for total treatment times of 3 – 4 hrs, and 3 hrs uninterrupted exposure times. For post-deposition FIB milling, the PtC deposits and surrounding areas were exposed to the ion beam (10 pA) at a magnification of approx. 8,800 x. The exposure time was varied for initial studies from 4 to 20 min, and then kept constant at 16 min and 20 min for PtC deposited at UMEs, and tip-integrated electrodes, respectively.

4.2.3 Physical characterization

EDX measurements were performed with an INCAx-sight detector (Oxford Instruments, U.K.) mounted on a Zeiss SEM Ultra60 (Thornwood, NY). The acceleration voltage of the primary electron beam was fixed at 6 keV in order to minimize contributions from the underlying silicon substrate. A 120 µm aperture was selected at high current mode, and a

100 s life time for data acquisition. Peak positions and peak intensities have to be optimized prior to EDX measurements. This is performed by using an element with an X-ray emission line in the spectrum range of interest as a reference point; for the present experiments silicon was used. EDX measurements were performed on three separate PtC patterns deposited at identical conditions.

Raman spectroscopy was performed in collaboration with Dr. Karl S. Booksh at the University of Delaware (Newark, DE). Raman spectra were acquired with a Bruker Senterra (Billerica, MA) Raman microscope operating with a frequency-doubled Nd:YAG ($\lambda = 532$ nm) laser as the excitation source, and equipped with a 50 x microscope objective yielding a probed spot size of approx. 2 µm in diameter. The incident laser power was maintained below 2 mW to avoid thermal damage of the sample. Variance in spectral values presented in this study corresponds to spectra acquired at three individual PtC patterns deposited at identical conditions. Spectral fitting was performed with the software package accompanying the instrument (OPUS, Bruker Optics, Billerica, MA). The 2050 - 750 cm^{-1} range of the spectrum was initially adjusted by fitting a straight baseline; then, the sp^2-hybridized carbon band was deconvoluted into two Gaussian shaped curves.

FPP measurements were performed using an Agilent DC power supply (Agilent 6612C; Santa Clara, CA), and two Hewlett Packard multimeters (HP 34401A; Palo Alto, CA) to measure current and voltage.

The same AFM instrument and configuration described in *Section 3.2.3* was used to acquire topographical images of PtC deposits before and after the annealing steps. Furthermore, pattern heights used to calibrate growth rates of IBID and pattern

dimensions used for FPP studies were determined by AFM. Triangular silicon nitride probes from Veeco (Woodbury, NY) were used for growth rate studies performed in contact mode, and silicon probes (Nanosensors, Switzerland) for dynamic mode AFM measurements. Topographical images presented were flattened with a second order function by the instrumental AFM software package (PicoScan 5.3.3; Agilent Technologies, Chandler, AZ). Simultaneous AFM-SECM imaging was performed in the arrangement introduced in *Section 3.2.3*.

4.2.4 Electrochemical characterization

The same potentiostats described in *Section 3.2.4* were used for all performed electrochemical analyses. Initial gold electroplating was performed via chronopotentiometry using Orotemp gold plating solution (Technic, Cranston, RI). The current was fixed at 1 nA for 3 min. Platinum UMEs were fabricated by sealing 5 µm diameter platinum microwires (Goodfellow, U.K.) into soda-lime glass capillaries (Hilgenberg, Germany), and subsequent grinding/polishing. Grinding was performed with diamond lapping films (9, 6, 1, and 0.5 µm) and water, and polishing using polishing cloths with colloidal alumina suspension (0.03 µm); all materials were obtained from Allied High Tech Products Inc. (Rancho Dominguez, CA). Electrical contacts were established using copper magnet wires (Belden, Richmond, IN), and a high temperature silver paste (Pyro-Duct 597-A, Aremco, Valley Cottage, NY). Prior to contacting, the insulation on the copper wires was stripped with a flame treatment and a piranha solution dip (H_2SO_4 from Fisher Scientific, Pittsburgh, PA; H_2O_2 from JT Baker, Phillipsburg, NJ; ratio 7:3) (Warning: Piranha solution is hazardous and highly reactive; extreme care and precaution must be taken at all times). Subsequently, the wires were sputtered with a

10 nm layer of titanium followed by a 190 nm layer of platinum to minimize effects from copper oxidation at the contact point during the annealing process. PtC UMEs were recycled after each experiment by polishing with 0.03 μm alumina suspension, 15 min exposure to Piranha solution, cleaning in 0.5 M H_2SO_4 with a sequence of different steps (one CV from -0.81 V to 2 V, at least twenty CVs from -0.61 V to 1 V, polarization for 2 min at 0.21 V; vs. saturated $Hg/HgSO_4$), and characterization by CV prior to deposition of a fresh PtC layer. Potentials are reported versus a saturated calomel electrode (SCE) for cyclic voltammetry using redox mediators and all studies to determine the charging currents, whereas a saturated $Hg/HgSO_4$ reference electrode was used to determine the working potential windows in 0.5 M H_2SO_4. In all experiments, a platinum wire was used as a counter electrode. CVs were acquired in aqueous solutions containing 5 mM hexaammineruthenium(III) trichloride ($Ru(NH_3)_6^{3+/2+}$, Sigma-Aldrich, St. Louis, MO) or 5 mM/10 mM $Fe(CN)_6^{3-/4-}$, and 0.5 M KCl as a supporting electrolyte. Solutions containing only 0.5 M KCl were used to evaluate charging currents. For comparative purposes, the determinations of the potential windows in H_2SO_4 were normalized to an average electrode area obtained from limiting steady-state currents at CVs in $Ru(NH_3)_6^{3+/2+}$ before and after treatments, respectively (n = 3 - 5). Deionized water obtained from a water purification system was used as described earlier. All solutions were sparged with argon (Airgas, Marietta, GA) for at least 15 min prior to electrochemical analysis.

Digital simulations to determine kinetic parameters of the heterogeneous electron transfer behavior (standard heterogeneous rate constant, k^0, and transfer coefficient, α) at PtC electrodes were performed using the DigiElch simulation software package[28]. Two-

dimensional semi-infinite diffusion at a disk electrode was selected as the best approximation for the used geometry. Electrode radii used in simulations were obtained from the limiting steady-state current of each CV under the assumption of a disk electrode geometry. For cases where the limiting steady-state current was not readily available (e.g. CVs recorded at pristine or ozone-treated PtC UMEs in $Fe(CN)_6^{3-/4-}$), average radii determined from the corresponding $Ru(NH_3)_6^{3+/2+}$ studies were used (n = 3 - 5, r = 4.5 - 4.7 µm). Diffusion coefficients were measured at platinum UMEs, and calculated from limiting steady-state currents. Values of $6.3 \times 10^{-6} \pm 0.1 \times 10^{-6}$ cm^2 s^{-1} and $7.5 \times 10^{-6} \pm 0.2 \times 10^{-6}$ cm^2 s^{-1} were obtained for $Fe(CN)_6^{3-/4-}$ and $Ru(NH_3)_6^{3+/2+}$ in 0.5 M KCl, respectively (n = 3). Other parameters used for simulations were E^0 ($Ru(NH_3)_6^{3+/2+}$) = -0.2013 V, and E^0 ($Fe(CN)_6^{3-/4-}$) = 0.2133 V (vs. SCE) at scan rates as applied in the conducted experiments.

4.3 Results and discussion

4.3.1 PtC deposited on AFM-SECM probes via IBID

Focused ion beam milling was used to expose frame electrodes at AFM-SECM probes according to the previously described procedure. Protruding PtC frames were deposited at AFM tip-integrated Au frame electrodes via IBID. *Figure 4.4A* shows representative CVs recorded in $Ru(NH_3)_6^{3+/2+}$ solution before and after the deposition of the PtC frame; the corresponding SEM images are shown in *Figure 4.4B*. The limiting steady-state current observed increases approx. 4-fold after the deposition of the PtC composite material. Considering the well-defined sigmoidal shape of the CV, which indicates fast electron

transfer at the heterogeneous interface this is very encouraging meaning that IBID has the capability to enable increasing the tip-integrated electrode area.

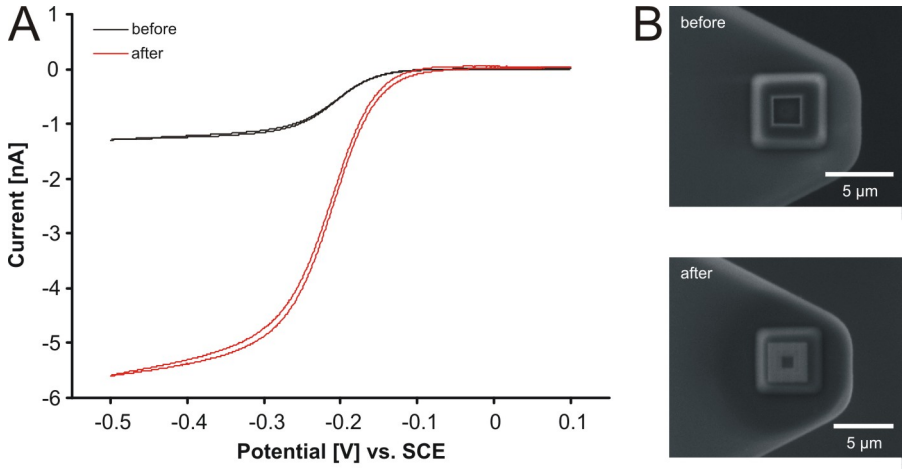

Figure 4.4. (A) CVs recorded at tip-integrated AFM-SECM probe before and after the deposition of PtC layer via IBID in 5 mM $Ru(NH_3)_6^{3+/2+}$ containing 0.5 M KCl supporting electrolyte (scan rate 0.1 V s^{-1}). (B) Corresponding top-view SEM images showing the PtC frame.

Combined AFM-SECM imaging was performed to evaluate the capability of tip-integrated PtC electrodes for simultaneously recording topographical and electrochemical surface properties. *Figure 4.5* shows topography and current images at two different electrode biases. The electrode was biased at -0.45 V vs. AgQRE (*A* and *B*) for the reduction of $Ru(NH_3)_6^{3+/2+}$. It should be noted that the elevated platinum grid leads to a positive feedback effect resulting in a localized current increase. As expected, the insulating silicon nitride substrate results in a negative feedback effect as evident by the decreased current. As a control experiment, the tip was biased at 0 V, where no considerable reduction of $Ru(NH_3)_6^{3+/2+}$ occurs. Correspondingly, the current image (*D*) shows no differences in current level depending on the electrical properties of the surface,

although the AFM tip was still scanned across the step of the grid (step height approx. 300 nm) as shown in the topography (*C*). This result demonstrates that AFM-SECM imaging is possible with AFM tip-integrated PtC electrodes, while maintaining sufficient electrochemical spatial resolution to clearly resolve the step matching the topography (*Figure 4.6*). Starting and end points of the grid step are marked and overlap for both the current and the topography.

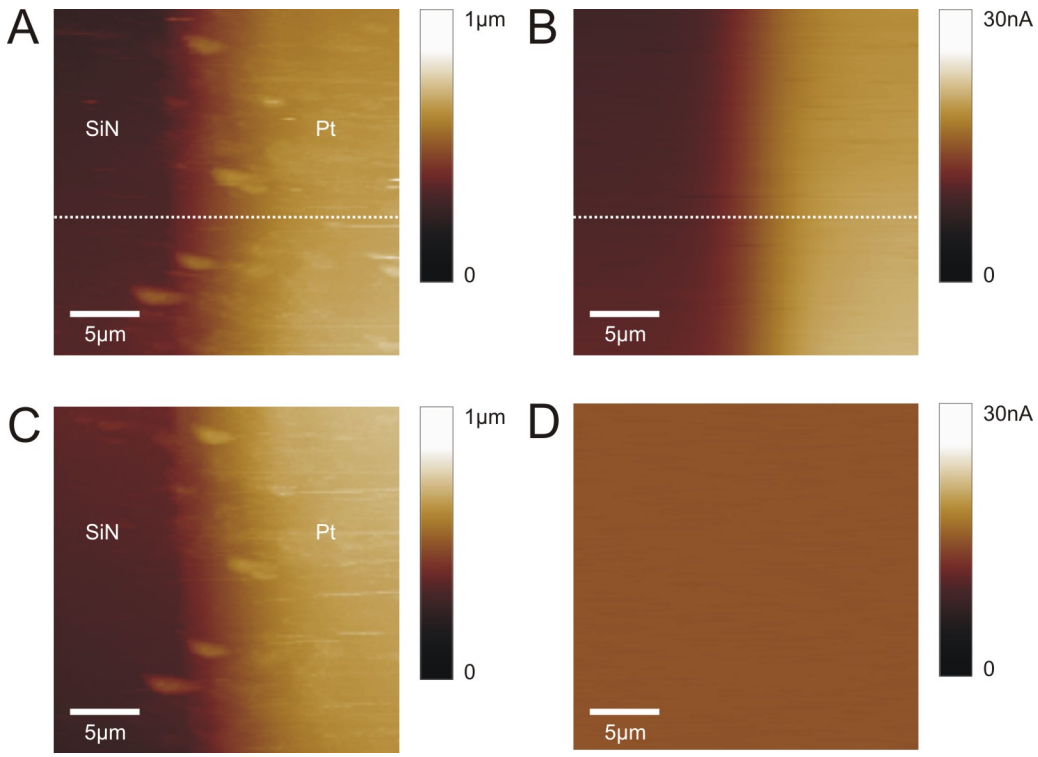

Figure 4.5. Simultaneous AFM-SECM imaging of elevated platinum features on a silicon nitride substrate. Topography (A and C), and current (B and D) images are shown. The tip-integrated PtC electrode was biased at -0.45 V (A and B) and 0 V (C and D) vs. AgQRE, respectively, in a 5 mM $Ru(NH_3)_6^{3+/2+}$ solution containing 0.5 M KCl. The tip was scanned in contact mode AFM with a scan rate of 0.72 lines s^{-1} (original scan size: 45 × 45 µm^2). The edge length of the PtC frame electrode was 3.3 µm, the width of the frame was 1.1 µm and the tip length 1.2 µm. Horizontal lines marked in (A) and (B) correspond to cross-sections shown in Figure 4.6.

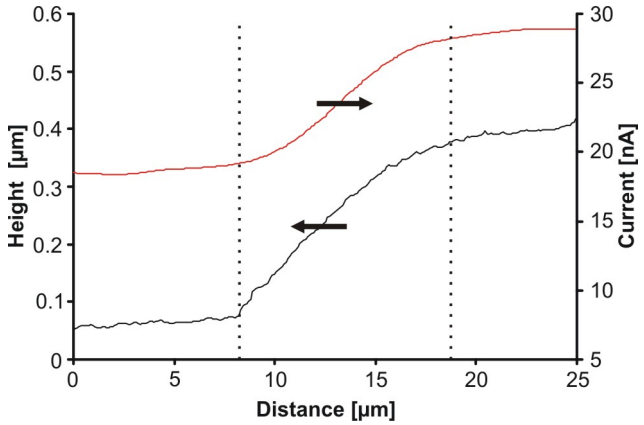

Figure 4.6. Cross-section of topography (black) and current (red) image shown in Figure 4.5 (A) and (B) at the location marked with the white horizontal line.

To further evaluate the electrochemical behavior of PtC electrode material in the anodic potential range, $Fe(CN)_6^{3-/4-}$ was selected as a redox active species. Additionally, the $Fe(CN)_6^{3-/4-}$ couple has been frequently used as a benchmark redox system to evaluate condition and reactivity of electrode surfaces, particularly in the case of carbonaceous materials[29]. In contrast to CVs obtained in $Ru(NH_3)_6^{3+/2+}$ (see *Figure 4.4*), CVs at AFM-SECM tip-integrated PtC electrodes in $Fe(CN)_6^{3-/4-}$ (*Figure 4.7*) lack the typical sigmoidal response indicating a slow electron transfer reaction at the electrode interface.

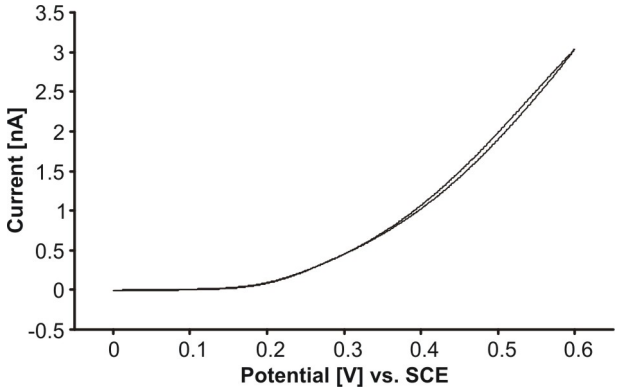

Figure 4.7. CV recorded at tip-integrated AFM-SECM probe modified with a PtC layer in 10 mM $Fe(CN)_6^{3-/4-}$ containing 0.5 M KCl supporting electrolyte (scan rate 0.1 V s^{-1}).

Despite the very encouraging initial results in $Ru(NH_3)_6^{3+/2+}$ solutions, the second set of studies performed in $Fe(CN)_6^{3-/4-}$ demonstrates that a thorough characterization of PtC composites deposited via IBID is necessary, in order to understand the observed behavior and for applying these novel materials as transducers for tip-integrated biosensors.

4.3.2 Physical and electrochemical characterization of pristine PtC deposits

4.3.2.1 Calibration of IBID growth rate via AFM

AFM measurements were performed to determine the thickness of the IBID patterns, and to calibrate the growth rate. The thickness of the deposits linearly increases with deposition time, and the growth rate increases with increasing ion beam currents (*Figure 4.8A*). It was found that for the selected pattern size and conditions the highest usable ion beam current was 500 pA. The IBID process can be viewed as equilibrium between material ablation and deposition; ion beam currents higher than 500 pA shift this equilibrium towards material ablation (*Figure 4.8B*), resulting in milling of the substrate instead of PtC deposition.

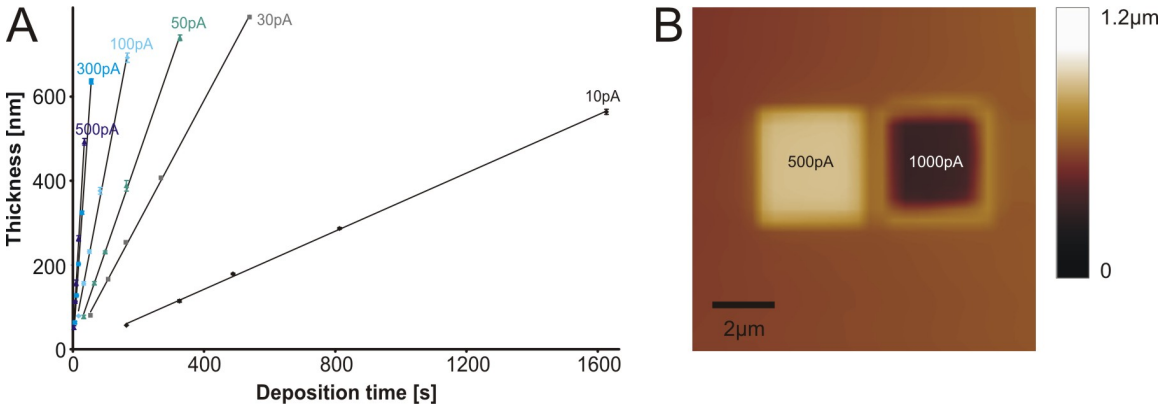

Figure 4.8. (A) Thickness of PtC patterns deposited at varying deposition times and ion beam currents (10 - 500 pA; n = 3). (B) CM AFM topography image of PtC deposits at 500 pA and 1000 pA demonstrating the shift of equilibrium from deposition to milling. Besides the ion beam current, all deposition parameters were kept the same.

4.3.2.2 EDX analysis

Literature reports for IBID of PtC deposits show a large difference in material composition with platinum concentrations ranging from 15 at% to 50 at% for pristine layers[19, 20]. At first glance, this appears to result from the use of different FIB systems and deposition parameters; however, it is difficult to establish a direct correlation between deposition parameters and composition, since frequently not all required information is provided to reproduce the reported results.

The composition of the material deposited within this study was evaluated via EDX, which provides a measurement of bulk concentrations, as incident primary electrons from the electron beam excite X-rays from a large excitation volume with a penetration depth dependent on parameters such as material composition, density and primary electron energy. Deposits used for EDX analysis were fabricated at varying ion beam currents at a thickness of approx. 1.1 µm in an effort to minimize contributions from the substrate during measurements. *Figure 4.9A* shows a typical EDX spectrum indicating mainly

contributions from carbon, platinum, and gallium. Contributions from the silicon substrate were typically < 0.5 at%, and also minor contributions from oxygen were observed (< 1.5 at%).

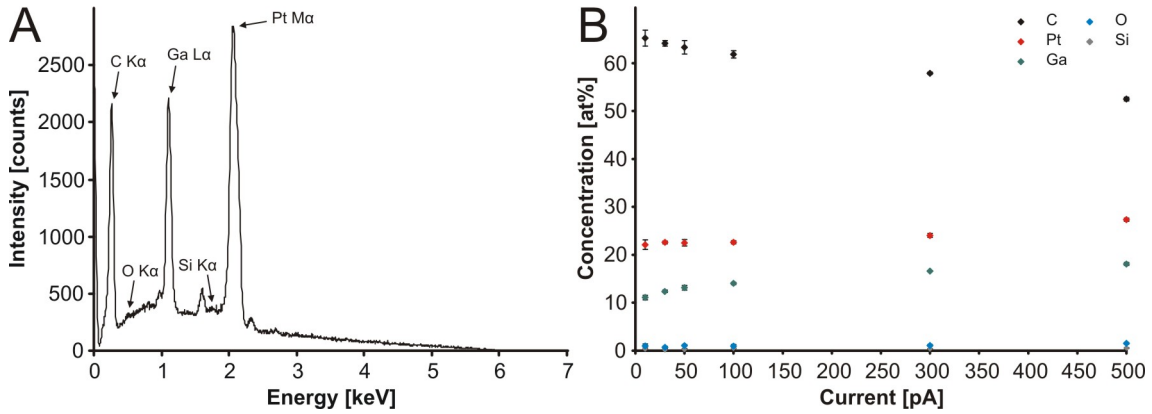

Figure 4.9. (A) Typical EDX spectrum observed at PtC deposits. (B) Atomic composition of PtC deposits after varying the ion beam current during IBID. Error bars correspond to the standard deviation retrieved from measurements at three different deposits fabricated at the same conditions.

As shown in *Figure 4.9B*, the concentration of carbon decreases with increasing ion beam current from 65.2 ± 1.7 at% to 52.5 ± 0.4 at%, whereas both platinum and gallium concentrations increase (from 22.1 ± 1.0 at% to 27.3 ± 0.3 at%, and 11.1 ± 0.5 at% to 18.1 ± 0.3 at%, respectively). The increase in gallium concentration can be attributed to the higher gallium ion density present during the deposition when comparing a 10 pA and 500 pA ion beam current in proportion to the beam diameter (*Figure 4.10*). Additionally, the higher ion density at the surface presumably also leads to preferential sputtering of lighter elements (carbon versus gallium and platinum), which has been suggested as one of the reasons for the higher metal content observed in IBID versus EBID[17]. However, the obtained results suggest that even at the highest beam current used in this study, the

platinum concentration did not exceed approx. 27 at%. Compared to platinum values reported in literature, these results tend towards the lower range[7, 19]. Telari et al. observed similar trends for the individual elements while varying the flux of incident ions[19].

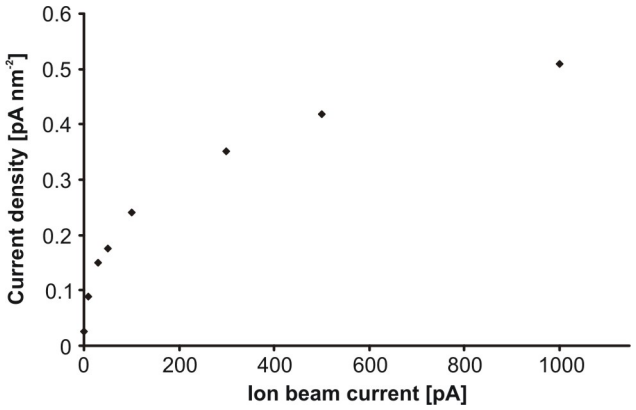

Figure 4.10. Correlation between ion beam current and current density, which was obtained by dividing the current by the beam diameter.

Since there is only a minor contribution from the Si substrate in the EDX spectra recorded at PtC patterns at a thickness of approx. 1.1 µm, thinner PtC layers were additionally evaluated in order to investigate, whether there is a correlation between material composition and thickness of the deposits. This aspect is of relevance, as thinner layers are used for increasing the electroactive area at AFM-SECM probes. *Figure 4.11* shows the composition of IBID PtC layers as a function of pattern thickness. Reducing the pattern thickness from approx. 1.1 µm to approx. 0.2 µm does not considerably change the composition besides a minor increase in silicon (from 0.2 ± 0.1 at% to 1.2 ± 0.1 at%), whereas the change for all other components is negligible. However, at a thickness of approx. 0.1 µm there is a much stronger contribution from the silicon substrate (12.2 ± 0.6 at%), thereby decreasing the relative amount of carbon, platinum,

and gallium detected by 10 – 20 at% compared to the 1.1 µm thick deposits. At this layer thickness, the substrate significantly interferes with the deposited sample, and it is difficult to reliably quantify the material composition; although it is likely that the true material composition is not considerably altered at thicknesses of approx. 0.1 µm, since only a small shift is detected. This hypothesis is supported by Iliadis et al., where Auger electron spectroscopic depth profiles recorded at similar patterns did not show considerable changes in the composition depending on the depth[30]. Therefore, it may safely be assumed that material compositions obtained from thick layers can be extrapolated to thin layers, which are proposed and used in this thesis.

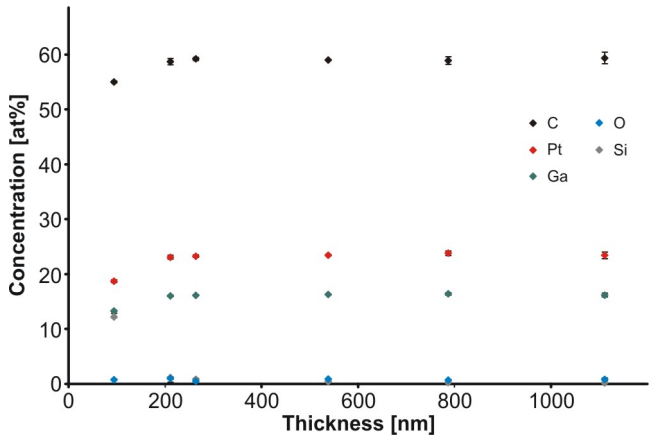

Figure 4.11. Atomic composition of PtC deposits with varying deposit thickness.

4.3.2.3 Raman spectroscopic studies

Visible Raman spectra of samples containing amorphous carbon are frequently characterized by two peaks (both pertaining to sp^2-hybridized carbon) convoluted into one broad band. The two features are labeled as the G- and the D-band, and are

associated with the E_{2g} stretching mode for all sp^2-carbon forms (chains and rings), and the A_{1g} ring breathing mode of graphitic carbon rings, respectively[31]. *Figure 4.12* shows an exemplary Raman spectrum recorded at a PtC sample locating these two bands after deconvolution from the fitted spectrum.

Trends in the G-band position, the full width at half maximum (FWHM), and the intensity ratio of the D- and G-band (I_D/I_G) are indicative of the molecular ordering within the sp^2 carbon phase, and under certain circumstances even provide access to indirect quantification of sp^3-hybridized carbon content[32]. The recorded Raman spectra of the deposits indicate the presence of graphitic rings in the matrix, and reveal a carbonaceous phase, which is overall amorphous in nature.

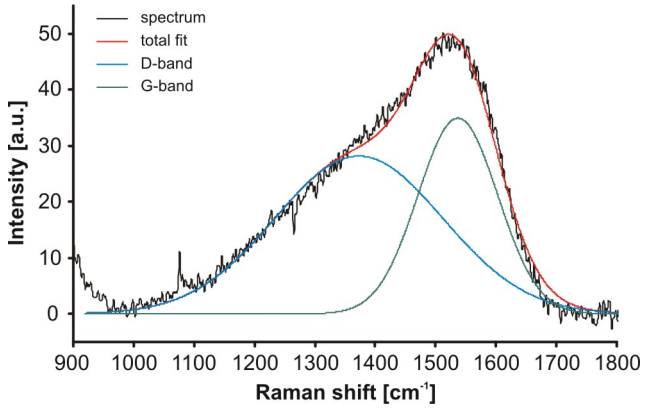

Figure 4.12. Raman spectrum recorded at pristine PtC deposit showing the spectral fitting and resulting deconvolution into D- and G-band.

PtC patterns deposited at different ion beam currents were investigated, and do not show any deviation in peak shape or peak position for the G-band, as summarized in *Table 4.1*. However, it can be clearly seen that depositions obtained at lower beam currents exhibit peaks with a stronger scattering intensity compared to samples obtained at higher beam

currents. This suggests that although the ordering in the carbonaceous phase is not influenced by the current density during the deposition, lower ion beam currents facilitate carbon incorporation, as expected. Although the Raman spectra collected with a visible excitation source reveal only the sp^2-hybridized carbon fraction, the observations are in excellent agreement with the trends evident in the EDX analysis (*Figure 4.9*)**.**

Table 4.1. Summary of peak fitting data obtained after deconvolution of Raman spectra deposited at different ion beam currents. PtC deposits used in these studies were approx. 100 nm thick and consisted of four sub-patterns each with an area of 8 μm^2.

Ion beam current [pA]	I_D/I_G	G-Band Position [cm^{-1}]	FWHM [cm^{-1}]	Intensity [a.u.]
10	0.82 ± 0.01	1534.6 ± 1.1	158.2 ± 0.9	57.1 ± 4.6
30	0.85 ± 0.01	1536.0 ± 2.0	157.2 ± 1.7	48.0 ± 3.8
50	0.87 ± 0.04	1535.3 ± 0.8	157.1 ± 1.2	46.0 ± 8.4
100	0.86 ± 0.02	1533.7 ± 1.4	159.0 ± 0.3	42.6 ± 0.3
300	0.83 ± 0.04	1534.3 ± 1.4	156.8 ± 1.7	29.8 ± 1.4
500	0.87 ± 0.02	1534.5 ± 2.4	157.9 ± 1.1	29.7 ± 2.7

4.3.2.4 Four-point probe measurements

Electrical resistivity of PtC deposits was evaluated in a four-point probe arrangement. Four micro-fabricated platinum contacts were connected to PtC deposits with PtC lines (*Figure 4.13A*); current was applied at the two outer contacts, and the voltage drop was measured between the two inner contacts. The electrical resistivity of a sample is derived from current-voltage characteristics while compensating for geometrical effects related to the dimensions and shape of a sample. The resistivity ρ of a material is defined by

$$\rho = \frac{A}{l} \times R\,, \tag{4.1}$$

where A is the cross-sectional area of the sample, l is the length of the sample, and R is the resistance. *Figure 4.13B* shows an exemplary current-voltage curve of four different PtC deposits (generated at identical conditions) showing a linear relationship between current and voltage. Based on Ohm's law, the resistance is obtained from the slope of the curve. PtC deposit dimensions were retrieved from AFM measurements. Although deposits fabricated at different ion beam currents were evaluated, no particular trend in resistivity could be observed. The electrical resistivity obtained averaging over all ion beam currents was $1.8 \pm 0.3 \times 10^{-3}$ Ω cm, which is within the range of values reported in literature[7, 20].

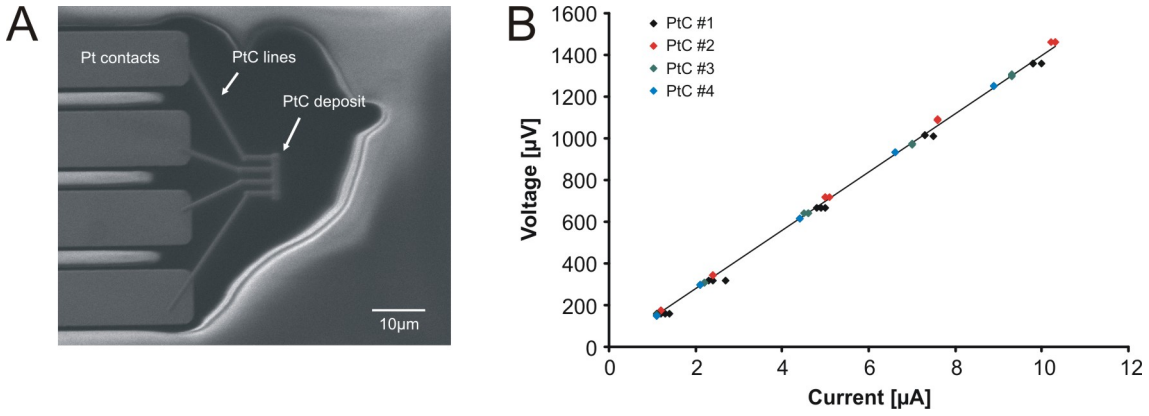

Figure 4.13. (A) SEM image showing the FPP configuration used for measurements of electrical resistivity. (B) Current-voltage curves measured at four different samples deposited at the same ion beam current (30 pA).

4.3.2.5 Electrochemical characterization of PtC deposits

In order to evaluate the electrochemical behavior of PtC layers fabricated by IBID in more depth, conventional platinum disk UMEs were used as substrates. As UMEs can be re-polished after each experiment and re-used for deposition of new and pristine PtC layers, this is a substantially more cost and time efficient approach compared to using AFM-SECM probes. Again, IBID was used to cover the surface of the platinum microwire with a PtC deposit. Similar to the initial experiments conducted at AFM-SECM probes, two redox systems, $Ru(NH_3)_6^{3+/2+}$ and $Fe(CN)_6^{3-/4-}$, were used for the electrochemical studies. *Figure 4.14* shows CVs obtained in $Ru(NH_3)_6^{3+/2+}$ and $Fe(CN)_6^{3-/4-}$ before and after the deposition of PtC, along with a SEM image showing the top view of a PtC UME (inset *Figure 4.14A*).

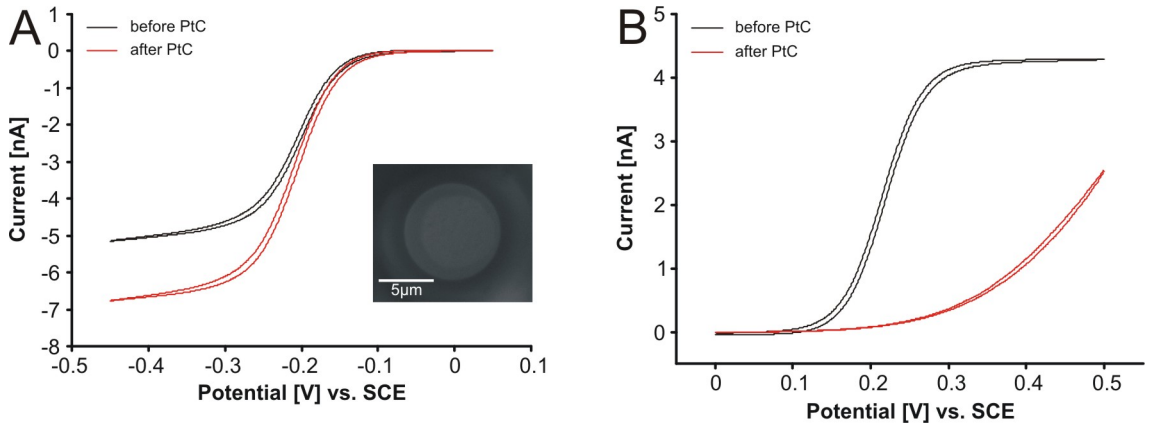

Figure 4.14. CVs obtained at UMEs before and after deposition of PtC layers in 5 mM $Ru(NH_3)_6^{3+/2+}$ (A), and 5 mM $Fe(CN)_6^{3-/4-}$ (B) solution containing 0.5 M KCl (scan rate 0.02 V s^{-1}). The inset in (A) shows a SEM image of a PtC deposit (top view).

The CV measured in $Ru(NH_3)_6^{3+/2+}$ (*Figure 4.14A*) shows an increase in limiting steady-state current after the deposition of PtC, which can be attributed to the increased

electroactive area. The protruded PtC layer disk UME was approximated with a flat disk UME in order to obtain an estimated electroactive area. The limiting steady-state current measured at a disk UME can be correlated to the electrode radius *r* via *Equation (2.6)*. The radius obtained before the deposition of PtC equals 3.4 ± 0.2 µm (n = 5). Handling of microwires with such small radii (nominal: 2.5 µm) is challenging, and a minute tilt of the wire in the sealed glass capillary may lead to slightly larger exposed UME cross-sections, and thus, larger true electrode radii observed. After the deposition, the radius corresponds to 4.7 ± 0.2 µm (n = 5). The difference to the nominal electrode radius of 4 µm is due to the protrusion of the electrode, and the fact that patterns fabricated by IBID are typically slightly larger than targeted. Excluding the increase in limiting steady-state current, the recorded CVs after the deposition of PtC are similar to CVs recorded at conventional platinum UMEs. There is no increase in charging current contribution or change in the CV shape, thereby indicating similar charge transfer characteristics. Moreover, they match the initial studies performed at AFM-SECM probes.

Similar to the experimental results at AFM-SECM probes and in contrast to the fast electron transfer behavior observed in $Ru(NH_3)_6^{3+/2+}$, CVs obtained in $Fe(CN)_6^{3-/4-}$ show a significantly slower electron transfer rate (*Figure 4.14B*). Considering these results and the high amount of carbon present in the deposits as determined by EDX analysis, the characteristics of carbon electrodes have to be discussed. Carbon based electrodes have several distinct advantages including low-cost, wide potential window, as well as a rich surface chemistry advantageous for chemical derivatization[33]. However, reproducible preparation and characterization of carbon surfaces is frequently considered challenging, since carbon materials exhibit a considerably large variety in surficial moieties and bulk

structures along with an innate tendency of adsorbing adventitious impurities. Careful surface preparation in addition to electrode surface activation steps is frequently necessary, in order to observe satisfying heterogeneous electron transfer rates for certain redox active species. The heterogeneous electron transfer process between the $Ru(NH_3)_6^{3+/2+}$ couple and the carbon electrode surface proceeds via a conventional outer-sphere mechanism that does not require direct interaction of the mediator with the sample surface, and therefore is not a surface sensitive process[29]. In contrast, the electron transfer mechanism for $Fe(CN)_6^{3-/4-}$ at carbon electrodes is quite complex[34]. Depending on the carbon material used and influenced by surface history drastically differing k^0 values have been observed[33]; for example, k^0 values vary from > 0.1 cm s^{-1} on glassy carbon fractured in solution to 1×10^{-6} cm s^{-1} at the basal plane of highly ordered pyrolytic graphite[33]. Although it seems that the electron transfer for $Fe(CN)_6^{3-/4-}$ at carbon electrodes does not depend on surface oxidation, it is clearly surface sensitive, since it has been shown that a monolayer of covalently bonded nitrophenyl groups causes a significant decrease in the electron transfer rate[35]. In order to quantify the electron transfer behavior at the PtC electrode interface digital simulations were performed, which will be discussed in *Section 4.3.3.4*.

As discussed above, the high carbon content seems to be an obstacle for certain electrochemical reactions, which is a particularly important consideration in the context of amperometric biosensor design. Since the original contribution by Guilbault and Lubrano in 1973, oxidase-based biosensors are often based on the oxidation of H_2O_2 as by-product of the enzymatic reaction to generate a current signal proportional to the analyte concentration[36]. Platinum has been frequently used as transducer for the anodic

determination of H_2O_2 since it exhibits catalytic properties favored by platinum oxides at the electrode surface[37, 38]. Therefore, techniques to improve the electron transfer rate at the PtC transducer material were investigated focusing on the removal or reduction of carbon in the composite, consequently shifting the material composition toward a higher relative amount of surficial platinum. Studies on H_2O_2 oxidation experiments were also performed at pristine PtC electrodes, and revealed slow electron transfer behavior; those results will be discussed in *Chapter 5* within the context of biosensing experiments.

4.3.3 Annealing of PtC deposits for improvement of the electron transfer rate

4.3.3.1 EDX analysis of annealed PtC deposits

Botman et al. showed that annealing of PtC patterns produced via EBID in reactive (O_2) environments leads to partial removal of carbon[23]. The authors compared samples annealed at different temperatures in N_2 (with 1 ppm O_2), air and pure O_2 environment. PtC composites annealed at elevated O_2 levels (air and pure O_2) showed similar results leading to a substantial decrease in carbon concentration from approx. 85 at% to approx. 30 at%. The authors concluded that carbon is removed via a thermally activated oxidation process, presumably releasing carbon in form of CO and/or CO_2. Adapting the procedure of Botman et al., PtC deposits were annealed at different temperatures in air. *Figure 4.15* shows that the carbon concentration starts decreasing at elevated temperatures and stabilizes at 400 °C to approx. 5 at%. Another evident trend is that the oxygen concentration in the sample substantially increases, presumably resulting from the oxidation of gallium and platinum in the composite material.

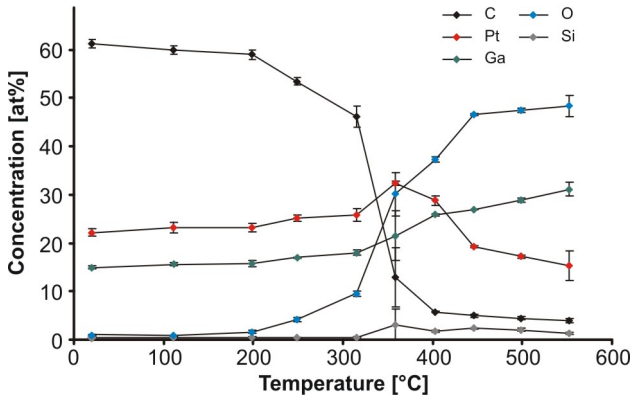

Figure 4.15. Atomic composition of PtC deposits after annealing for 11 min at varying temperatures. EDX measurements were performed at three different deposits fabricated at same conditions. Lines connecting the data points are included only to help visualizing the trend.

4.3.3.2 Raman analysis of annealed PtC deposits

Raman spectroscopic studies were performed at annealed PtC patterns, since G-band position, FWHM, and I_D/I_G are indicative of ordering of the sp^2-hybridized carbon, which is presumably influenced by the temperature treatment. The foremost evident spectral feature recognizable in *Figure 4.16* is the steadily decreasing Raman scattering intensity with increasing annealing temperature. Ultimately, at temperatures above 400 °C the intensity of the sp^2-hybridized carbon band drops below the detectable limit. Similar to the ion beam current variation studies discussed in *Section 4.3.2.3*, the decrease in Raman scattering intensity is complemented by the trend observed during EDX analysis. Further evaluation of the Raman spectrum acquired at 200 °C indicates that the sp^2-hybridized carbon phase undergoes a crystalline re-arrangement, which is indicated by the increased scattering intensity of the D-band along with the minor blue-shift of the G-band maximum. At 300 °C, these spectral changes become even more pronounced resulting in a G-band shift from 1539 ± 1 cm^{-1} to 1563 ± 5 cm^{-1} in addition to the narrower FWHM

(from 152 ± 3 cm^{-1} to 120 ± 4 cm^{-1}). Additionally, I_D/I_G increases from 0.83 ± 0.01 to 1.36 ± 0.13. At 350 °C, the sp^2-carbon content becomes too low to be reliably quantified. The combined observed spectral trends suggest that annealing induces considerable re-arrangement of the initially amorphous carbon phase into a more structured state composed of six-membered carbon rings (graphite-like). Similar trends have been reported for other annealed amorphous carbon materials deposited via conventional physical and chemical vapor deposition techniques both in the presence[39] and absence[40, 41] of platinum.

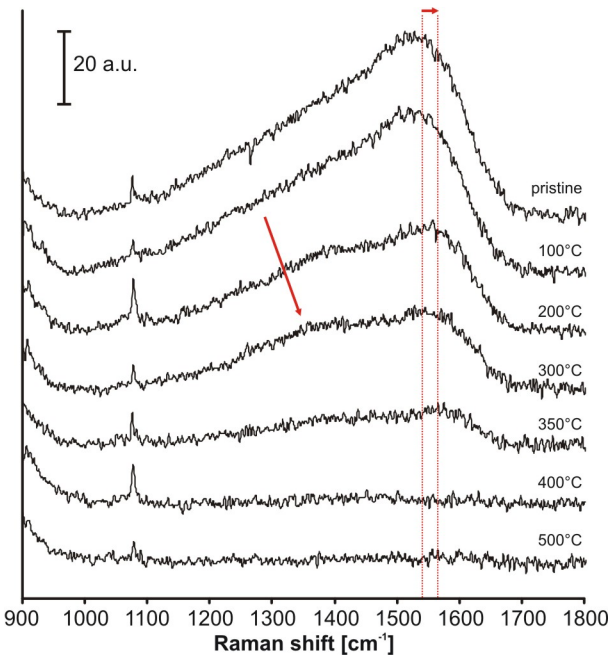

Figure 4.16. Raman spectra recorded at pristine and annealed PtC deposits. Spectra are offset for clarity. Red arrows mark the G-band shift and D-band intensity increase at 300 ºC.

4.3.3.3 High resolution atomic force microscopy

Dynamic mode atomic force microscopy imaging at pristine and annealed PtC deposits was performed to evaluate morphological changes as a function of the annealing temperature. IBID PtC materials were previously investigated by transmission electron microscopy (TEM) analysis; the material is described as composition of crystalline platinum grains dispersed in a matrix of gallium doped amorphous carbon[6, 42] with grain diameters in the range of 3 - 8 nm[20, 42]. *Figure 4.17* shows dynamic mode AFM images of the sample topography obtained at pristine (A), and annealed samples (B) (400 °C). It can be clearly seen that the microstructure of the sample changes: pristine PtC deposits have larger surface feature sizes, and the roughness of the samples increases during the annealing process (rms height increases from 2 to 11.5 nm).

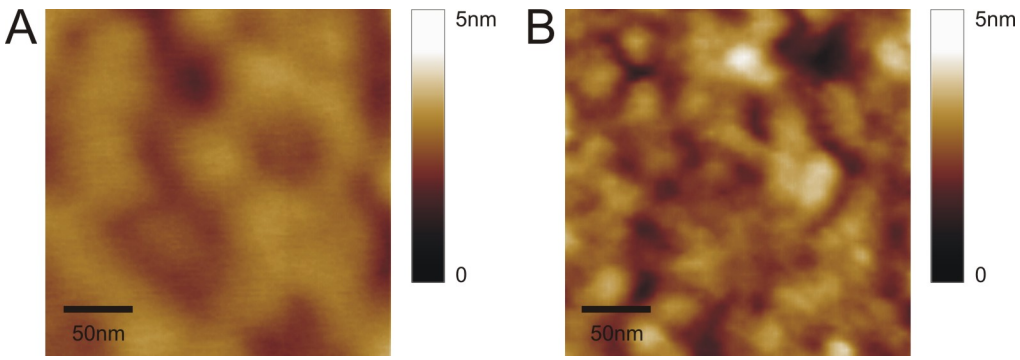

Figure 4.17. Dynamic mode AFM topography images obtained at pristine (A), and annealed (B) (400 ºC) PtC deposits.

4.3.3.4 Electrochemical characterization of annealed PtC deposits

In order to minimize excessive oxidation of the PtC layers while still removing carbon, annealing of the electrodes was performed at approx. 400 °C. SEM was performed after

selected electrochemical experiments proofing appropriate coverage of the electrode, and excluding contributions from the underlying platinum UME after the temperature treatment. *Figure 4.18* shows CVs obtained at pristine and annealed UMEs in $Ru(NH_3)_6^{3+/2+}$ (*A*) and $Fe(CN)_6^{3-/4-}$ (*B*). The CV in $Ru(NH_3)_6^{3+/2+}$ shows only a minor increase in limiting steady-state current by approx. 10 % while maintaining the typical curve shape, as opposed to the CV obtained in $Fe(CN)_6^{3-/4-}$, which changes drastically yielding a sigmoidal response after the annealing step. The first observation is attributed to an increase in surface roughness ($r_{annealed} = 5.2 \pm 0.1$ µm, n = 5), and the latter to the removal of carbon impurities from the electrode improving the electron transfer rate for $Fe(CN)_6^{3-/4-}$. Although the electron transfer for the $Fe(CN)_6^{3-/4-}$ couple at platinum electrodes is also dependent on electrode cleaning procedures, the k^0 values are generally in the range of 1×10^{-2} cm s^{-1} to 2.3×10^{-1} cm s^{-1} [43].

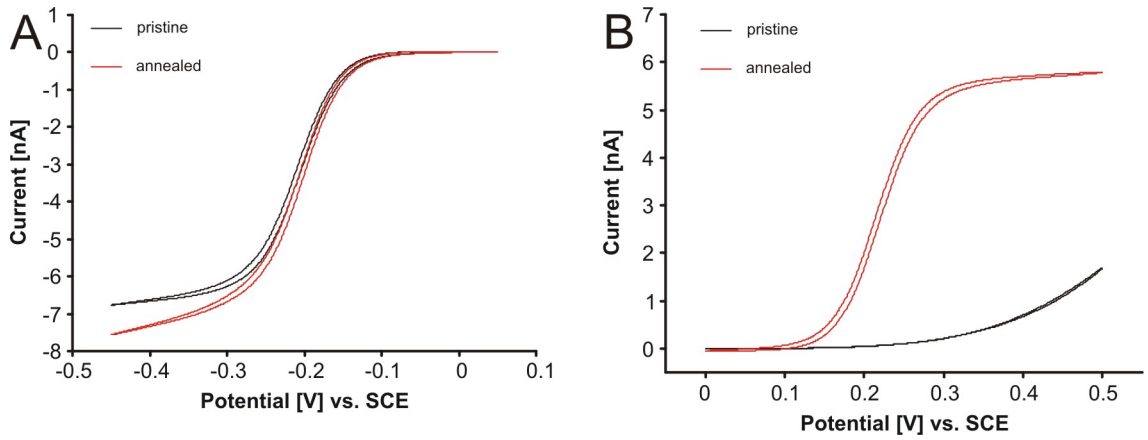

Figure 4.18. CVs obtained at pristine and annealed PtC UMEs in 5 mM $Ru(NH_3)_6^{3+/2+}$ (A), and 5 mM $Fe(CN)_6^{3-/4-}$ (B) solution containing 0.5 M KCl as supporting electrolyte (scan rate 0.02 V s^{-1}).

For further investigations of the improvement of the heterogeneous electron transfer behavior, simulations were performed based on the measured CVs to obtain kinetic parameters, which are summarized in *Table 4.2*. As expected from the initial inspection of the results, the standard heterogeneous rate constant k^0 for the reduction of $Ru(NH_3)_6^{3+/2+}$ does not substantially change aside from a minor improvement of 7.1×10^{-2} cm s^{-1} to 1.3×10^{-1} cm s^{-1}. In contrast, k^0 values extracted from CVs for the oxidation of $Fe(CN)_6^{3-/4-}$ drastically change from 3.3×10^{-4} cm s^{-1} to 1.5×10^{-1} cm s^{-1} corresponding to an improvement of almost three orders of magnitude. After the thermal annealing procedure, both mediators investigated exhibit a reversible electron transfer behavior.

Table 4.2. Kinetic parameters determined from simulations at pristine and annealed PtC UMEs (n = 5).

	$Ru(NH_3)_6^{3+/2+}$ k^0 [cm s^{-1}]	α	$Fe(CN)_6^{3-/4-}$ k^0 [cm s^{-1}]	α
pristine	$7.1\times10^{-2} \pm 1.1\times10^{-2}$	0.46 ± 0.04	$3.3\times10^{-4} \pm 1.0\times10^{-4}$	0.69 ± 0.01
annealed	$1.3\times10^{-1} \pm 5.9\times10^{-2}$	0.31 ± 0.03	$1.5\times10^{-1} \pm 5.8\times10^{-2}$	0.70 ± 0.01

Charging currents measured in the supporting electrolyte used during kinetic studies were investigated by recording CVs at varying scan rates at pristine and annealed PtC UMEs (*Figure 4.19A*). As depicted in *Figure 4.19B*, charging currents show a linear dependency on the scan rate, which is in agreement with theory[44]. The apparent electrode capacitance was calculated from this dependency utilizing *Equation (2.11)*, and resulted in an increase from approx. 60 µF cm^{-2} to approx. 830 µF cm^{-2} after annealing. Typical capacitance values recorded at electrodes in aqueous solutions are in the range of 20 µF cm^{-2} [45]. The capacitance recorded at the pristine PtC layer shows a reasonable range, however, after annealing there is a considerable increase observed. It seems likely

that this increase in capacitance originates from the increase in surface roughness documented by AFM studies at annealed layers, as charging currents are - in contrast to faradaic currents - more sensitive to microscopic surface roughness changes[33].

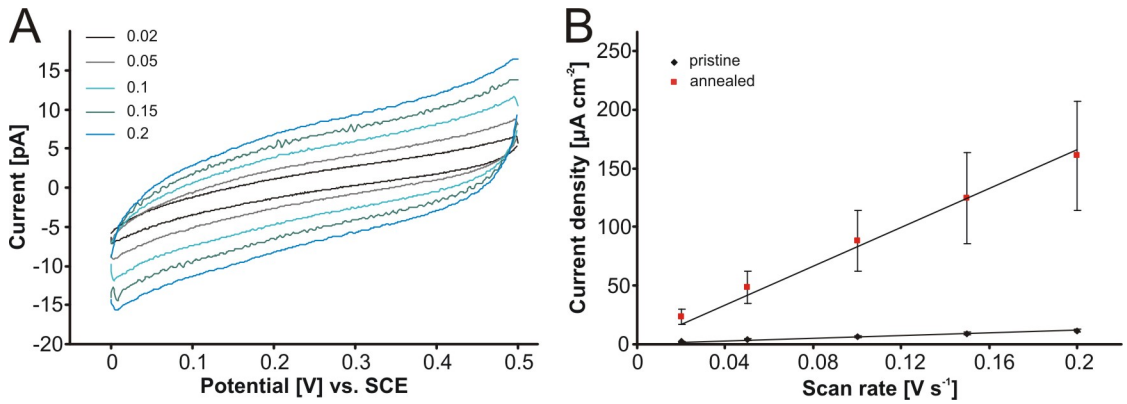

Figure 4.19. (A) CVs measured at pristine PtC UME at different scan rates (0.02 V s^{-1} to 0.2 V s^{-1}) in 0.5 M KCl. (B) Scan rate dependency of charging currents recorded at pristine and annealed PtC UMEs in 0.5 M KCl (n = 4).

An important aspect of new electrode materials is the useful working potential range. Working potential windows of PtC-based UMEs in H_2SO_4 were evaluated before and after the thermal treatment. *Figure 4.20* compares the working potential window, and shows a decrease of approx. 0.24 V at the anodic end of the potential range as a result of the annealing step suggesting that O_2 formation is favored after the annealing.

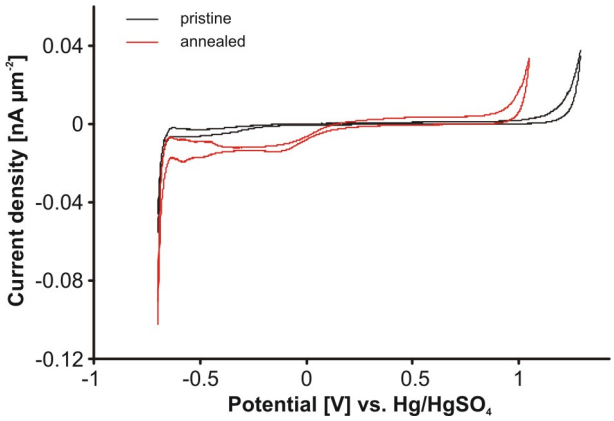

Figure 4.20. Working potential windows at pristine and annealed PtC UMEs recorded in 0.5 M H_2SO_4 (scan rate 0.1 V s^{-1}).

Working potential windows of carbon-based electrodes vary substantially depending on the actual carbon structure. Values of approx. 3.5 - 3.7 V were reported for high quality boron-doped diamond and nitrogen-doped diamond-like carbon electrodes, whereas approx. 2 - 2.1 V were reported for more graphitic electrodes, such as glassy carbon or highly-oriented pyrolytic graphite[46-48]. It has been suggested that an increase in sp^2-carbon content at the electrode surface is correlated with a decrease of the working potential window range, since it facilitates adsorption of dissolved species to the surface compared to the more inert hydrocarbon-like surface, such as boron-doped diamond[29, 46, 49]. In general, carbon-based electrodes show significantly slower kinetics for surface oxidation and hydrogen evolution compared to metal electrodes[29]. Typically, CVs recorded at platinum electrodes in aqueous acidic media show evolution of hydrogen below 0 V (vs. SHE), whereas oxygen evolution occurs above approx. 1.5 V (vs. SHE). Hence, the decrease of the potential range observed after the temperature treatment is correlated to the increased amount of platinum present at the electrode surface due to the partial removal of carbon.

Additionally features in the CV after the annealing step show a very characteristic shape for platinum surfaces including the voltammetric signatures for the adsorption of hydrogen (*Figure 4.20*). The charge resulting from the adsorption of H^+ was used to estimate the electrochemically active platinum surface area. This approximate charge can be extracted from CVs recorded in acidic aqueous media by integration of the cathodic current in the potential range of -0.63 V to -0.26 V (vs. $Hg/HgSO_4$) after correcting for charging current contributions. For this approximation, a surface interaction of 1:1 (H:Pt) was assumed, and a hydrogen adsorption charge of 210 $\mu C\ cm^{-2}$ per monolayer[50]. Using these approximations, an adsorption charge of 6.9×10^{-5} µC was calculated, which corresponds to a platinum surface area of approx. 33 μm^2. Assuming a flat disk-shaped electrode and utilizing the electrode radius of 5.2 µm obtained from the limiting steady-state current, the total area of the electrode is 84.6 μm^2. However, since the diffusion-controlled current is typically proportional to the projected area and is not affected by the microscopic surface roughness to the extent adsorption or capacitive effects are influenced, the true total surface area may differ from this value. Consequently, this may contribute to the observed discrepancy between the relative amount of platinum obtained by EDX analysis (28.8 ± 1.0 at%), compared to the approx. 39.1 % of platinum fraction calculated from the hydrogen adsorption data. Additionally, as EDX is a bulk technique, possible enrichment of platinum at the surface due to annealing is not resolvable, whereas the electrochemical adsorption data is highly surface sensitive.

Concluding, it could be shown that annealing is efficient in removing the carbon from the composite material, and leads to the desired improvement of electrode characteristic.

4.3.3.5 Annealing of AFM-SECM probes

AFM-SECM probes were annealed at the same conditions (11 min, 400 ºC) used for PtC layers on UMEs in order to evaluate transfer of the developed process to the cantilevers. *Figure 4.21* shows optical micrographs of an AFM-SECM probe before and after the annealing. As marked with the red circle in *Figure 4.21B*, the AFM cantilever bends after the annealing procedure. This bending is sufficient to disturb the deflection of the laser spot from the cantilever such that the optical readout of the deflection in the experimental setup is not possible. The bending results from different temperature expansion coefficients of the layered gold and silicon nitride material. Hence, the thermal annealing process successfully applied at UMEs may not be transferred to AFM-SECM probes, and a more "gentle" approach has to be developed.

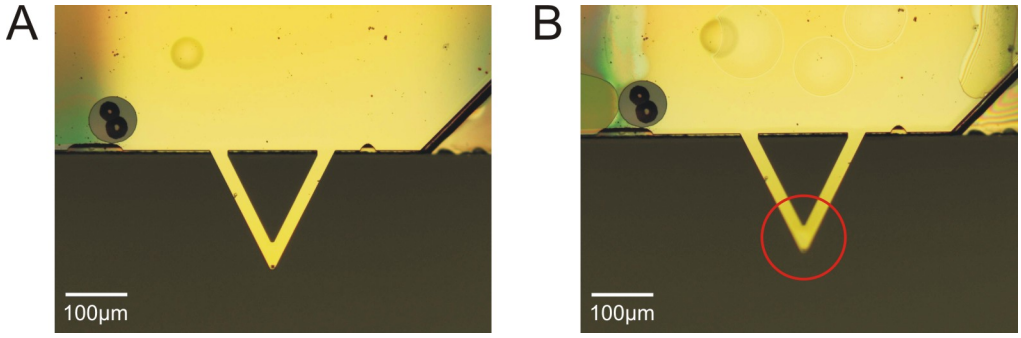

Figure 4.21. Optical micrographs of AFM-SECM probes before (A) and after (B) annealing (400 ºC, 11 min). The red circle marks the cantilever bending evident by the tip moving out of focus.

4.3.4 Alternative approaches to improve the electron transfer behavior

4.3.4.1 UV/ozone treatment

An alternative approach to treat PtC layers for improvement of electron transfer kinetics is based on a UV/ozone exposure derived from a study published by Wipf and co-workers[51]. The authors observed an improvement of electron transfer kinetics for catechols and ascorbic acid at glassy carbon electrodes after a UV/ozone treatment step. They concluded that a carbon overlayer, produced during polishing with alumina paste, was removed by oxidation of the carbon to CO_2 by this treatment. Additionally, a cleaning effect was observed removing other contaminants from the surface, and therefore restoring the electrode activity.

Based on the obtained results from PtC layers on UMEs in respect to the sensitivity of $Fe(CN)_6^{3-/4-}$ to the condition and reactivity of the PtC surface, $Fe(CN)_6^{3-/4-}$ was selected as a "probe" to determine the effectiveness of alternative treatment procedures. Similar to *Sections 4.3.2.5* and *4.3.3.4*, PtC-covered UMEs were used for evaluation of the treatment procedures. CVs in $Fe(CN)_6^{3-/4-}$ were performed at PtC UMEs after 30 min UV/ozone treatment intervals as shown in *Figure 4.22* to evaluate the time required for sufficient carbon removal from the surface. Similar to thermal annealing, this treatment appears to improve the electron transfer at the PtC UME, and the response to the oxidation of $Fe(CN)_6^{3-/4-}$ is stabilized after approx. 3 hrs. Kinetic parameters derived from simulations are summarized in *Table 4.3* for the pristine and UV/ozone-treated (after 3 hrs treatment) PtC-modified UME. The standard heterogeneous rate constant improved by almost two orders of magnitude.

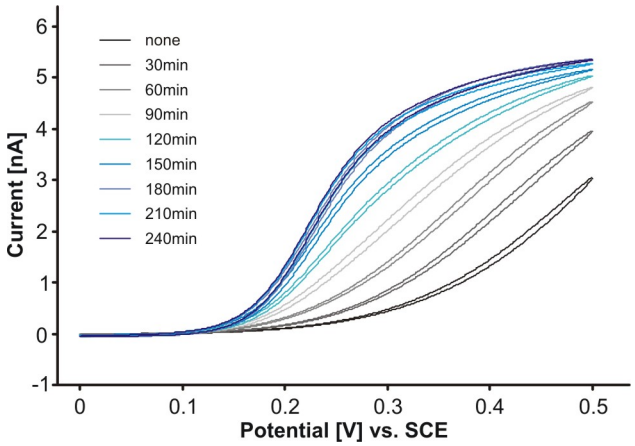

Figure 4.22. CVs in 5 mM $Fe(CN)_6^{3-/4-}$ containing 0.5 M KCl were performed at PtC UMEs in between 30 min UV/ozone treatment steps (scan rate 0.02 V s^{-1}).

Table 4.3. Kinetic parameters determined from digital simulations at pristine and 3 hrs ozone-treated PtC UME.

	$Fe(CN)_6^{3-/4-}$ k^0 [cm s^{-1}]	α
pristine	5.2×10^{-4}	0.66
ozone-treated	1.6×10^{-2}	0.61

After initial studies determining the time needed to obtain improved electron transfer kinetics, the UV/ozone treatment was applied continuously for a period of 3 hrs. CVs were recorded at PtC UMEs before and after exposure to the UV/ozone atmosphere in $Ru(NH_3)_6^{3+/2+}$ (*Figure 4.23A*), and $Fe(CN)_6^{3-/4-}$ (*Figure 4.23B*), respectively. In contrast to the values reported in *Table 4.3* where the treatment was obtained during six UV/ozone treatment steps, the standard heterogeneous rate constant for the oxidation of $Fe(CN)_6^{3-/4-}$ improved only slightly from 4.9×10^{-4} cm s^{-1} to 2.0×10^{-3} cm s^{-1} (*Table 4.4*). The CV in $Ru(NH_3)_6^{3+/2+}$ remained essentially unaltered with only a minor increase of the standard heterogeneous rate constant from 8.1×10^{-2} cm s^{-1} to 1.3×10^{-1} cm s^{-1} (*Table 4.4*), as previously observed for thermal annealing.

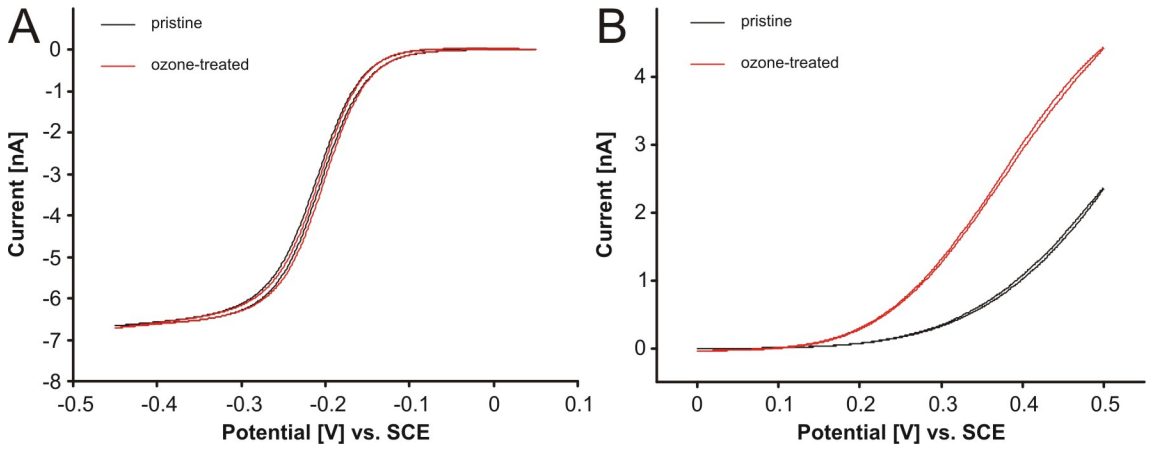

Figure 4.23. CVs obtained at pristine and ozone-treated PtC UMEs in 5 mM $Ru(NH_3)_6^{3+/2+}$ (A), and 5 mM $Fe(CN)_6^{3-/4-}$ (B) solution containing 0.5 M KCl (scan rate 0.02 V s^{-1}).

Table 4.4. Kinetic parameters determined from simulations at pristine and 3 hrs ozone-treated PtC UMEs (n = 3; continuous treatment).

	$Ru(NH_3)_6^{3+/2+}$ k^0 [cm s^{-1}]	α	$Fe(CN)_6^{3-/4-}$ k^0 [cm s^{-1}]	α
pristine	$8.1\times10^{-2} \pm 3.3\times10^{-2}$	0.48 ± 0.07	$4.9\times10^{-4} \pm 2.1\times10^{-4}$	0.69 ± 0.01
ozone-treated	$1.3\times10^{-1} \pm 6.0\times10^{-4}$	0.37 ± 0.01	$2.0\times10^{-3} \pm 7.8\times10^{-4}$	0.65 ± 0.02

Additional studies were conducted to evaluate this behavior. In a first step, the UV/ozone chamber was vented to remove possibly enriched contaminants in the atmosphere of the chamber, and a dipping/flushing step with H_2O was introduced to wash off possibly adhering contaminants from the electrode surface in between the treatment steps. None of these sets of studies led to the same extent of improvement in electrode kinetics, as initially observed in *Figure 4.22*, where a potential ramp in form of cyclic voltammetry was applied between the treatment steps. Hence, the initial experiments were repeated, with the only difference that PtC electrodes were biased in KCl solutions every 30 min throughout the 3 hrs UV/ozone treatment steps by cycling the potential between 0 – 0.5 V (vs. SCE) in order to investigate the influence of an applied potential. Only before and

after the treatment one CV was recorded in $Fe(CN)_6^{3-/4-}$. In this experiment, a similar trend was obtained, as in the first set of experiments. This indicates that the solution exposure and potential sweeping in combination with the UV/ozone treatment has an additional cleaning effect on the PtC UMEs. Given the fabrication time and cost for AFM-SECM probes, any additional handling steps and electrochemical experiments are usually minimized before the targeted application to avoid possible damage of the combined probes. Thus, a pre-treatment procedure based on prolonged electrochemical biasing is not an ideal approach, and hence, was not further considered relevant for these studies. Additionally, the presented approach of potential cycling of the PtC layers in between UV/ozone treatment steps is highly labor intensive, since every single electrode needs to be individually treated for an extended period of time. Therefore, the precise evaluation of mechanisms involved during UV/ozone treatment is the scope of future studies.

4.3.4.2 Post-deposition FIB milling

The third approach for reducing the carbon content is based on preferential sputtering of carbon with the focused ion beam. During preferential sputtering, the ejection of lighter elements is favored resulting in a surficial enrichment of heavier elements[52].

Similarly to *Section 4.3.4.1*, $Fe(CN)_6^{3-/4-}$ was again selected as a "probe" to determine the effectiveness of the preferential sputtering process. Initial studies were conducted at PtC UMEs exposed to the FIB for varying periods of time at a beam current of 10 pA immediately after the IBID process. *Figure 4.24* shows selected CVs recorded in $Fe(CN)_6^{3-/4-}$ after post-deposition FIB milling. It is apparent from those CVs that the

electron transfer rate drastically improves with an increase of milling time, and remains essentially unaltered after approx. 16 min.

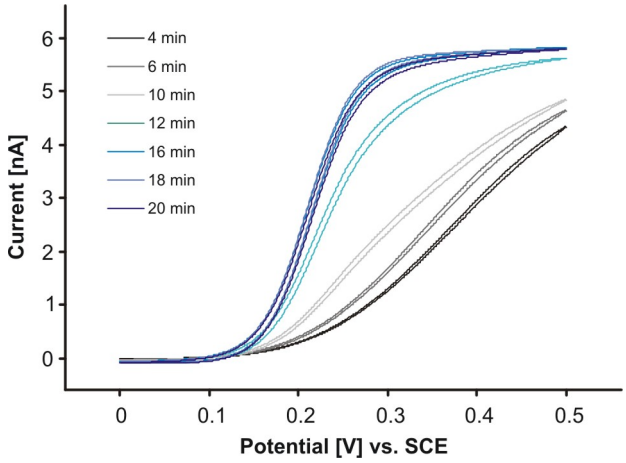

Figure 4.24. CVs recorded at PtC UMEs after FIB milling for varying periods of time in 5 mM $Fe(CN)_6^{3-/4-}$ solution containing 0.5 M KCl (scan rate 0.02 V s^{-1}).

After determination of the optimum FIB milling time, CVs at PtC UMEs were again recorded in $Fe(CN)_6^{3-/4-}$ and $Ru(NH_3)_6^{3+/2+}$. Standard heterogeneous rate constants were determined from the CVs, as previously described, and are summarized in *Table 4.5*. The electron transfer rate is enhanced after the FIB milling procedure for $Fe(CN)_6^{3-/4-}$ in comparison to pristine PtC UMEs, and the obtained rates are similar to the results obtained at thermally annealed PtC UMEs. In contrast, the reduction of $Ru(NH_3)_6^{3+/2+}$ proceeds at similar rates as at pristine layers.

Table 4.5. Kinetic parameters determined from simulations at pristine and FIB-milled PtC UMEs (n = 3). Values for pristine layers are reproduced from Table 4.2 for comparative purposes.

	$Ru(NH_3)_6^{3+/2+}$ k^0 [cm s^{-1}]	α	$Fe(CN)_6^{3-/4-}$ k^0 [cm s^{-1}]	α
pristine	$7.1\times10^{-2} \pm 1.1\times10^{-2}$	0.46 ± 0.04	$3.3\times10^{-4} \pm 1.0\times10^{-4}$	0.69 ± 0.01
FIB-milled	$5.1\times10^{-2} \pm 7.2\times10^{-3}$	0.47 ± 0.03	$2.1\times10^{-1} \pm 3.8\times10^{-2}$	0.84 ± 0.02

Again, working potential windows in H_2SO_4 at PtC UMEs after FIB milling for 16 min were analyzed. *Figure 4.25* shows the working potential window in comparison to the working potential window at a pristine PtC UME. In comparison to the pristine PtC layer, there is a minor decrease by approx. 0.13 V at the anodic potential end. Although the change is not as pronounced as for the thermally-annealed PtC UMEs (*Section 4.3.3.4*), the same trend is obtained, and may be again attributed to the localized increase of surficial platinum content. In contrast to the annealing data presented earlier, the signature for the adsorption of hydrogen to platinum is not pronounced enough to allow reliable quantification however, it is still qualitatively visible.

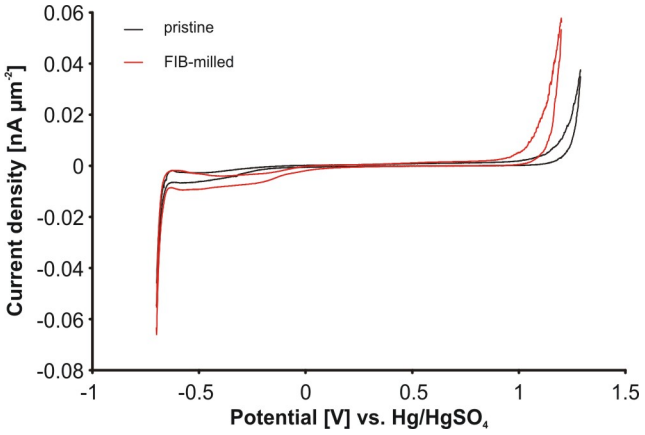

Figure 4.25. Working potential windows at pristine and PtC UMEs FIB-milled for 16 min recorded in 0.5M H_2SO_4 (scan rate 0.1 V s^{-1}).

Finally, PtC frame electrodes were deposited on AFM-SECM probes, and subsequently exposed to a post-deposition FIB milling step. The post-deposition FIB milling time had to be increased by 4 min to 20 min for AFM-SECM probes in order to achieve stable unaltered CVs. This difference to UME treatment is most likely due to the different deposition parameters (targeted electrode area 8 μm^2 and ion beam current 30 pA) used, which presumably have an influence on the PtC composition. *Figure 4.26* shows CVs in $Fe(CN)_6^{3-/4-}$ at such AFM-SECM probes before and after the deposition of PtC followed by consecutive FIB milling. It is crucial that the insulation layer after the milling step is not damaged, which can be derived from SEM imaging and the CV showing the conventional sigmoidal shape characteristic for such small electrodes. This approach seems promising for the design of IBID-increased electrodes, and will be further evaluated for studies using H_2O_2 as target analyte in biosensing applications (*Chapter 5*).

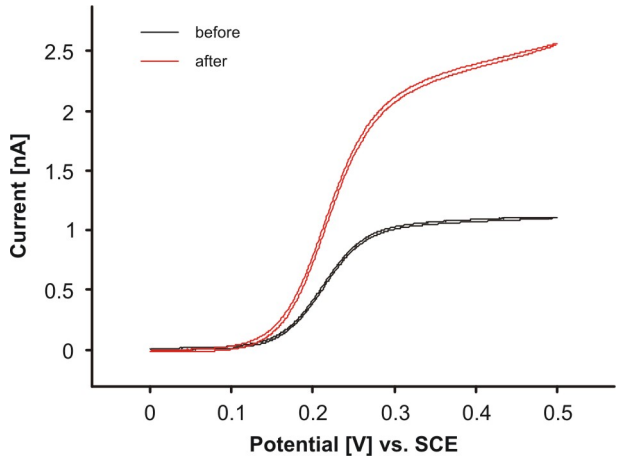

Figure 4.26. CVs recorded at tip-integrated AFM-SECM probe before and after the deposition of PtC layer via IBID in 5 mM $Fe(CN)_6^{3-/4-}$ containing 0.5 M KCl supporting electrolyte (scan rate 0.1 V s^{-1}). The PtC layer was treated by immediate post-deposition FIB milling for 20 min.

4.4 Final remarks

The properties of pristine and treated PtC deposits fabricated by IBID were investigated as novel patternable electrode materials. Initial results performed at PtC tip-integrated AFM probes are promising; EDX, Raman analysis, FPP, and AFM along with cyclic voltammetric studies were performed to investigate in detail the properties of this composite material. A high content of carbon in the composite materials was defined as an obstacle for applications in tip-integrated biosensor design.

Consequently, several electrode pre-treatment procedures were evaluated focusing on the removal of carbon to increase the relative amount of the surficial platinum content. Annealing PtC deposits at varying temperatures revealed a trend, which includes a pronounced decrease in carbon content stabilizing at approx. 5 at% carbon above 400 ºC, as determined by EDX analysis. These results are complemented by Raman spectroscopic and electrochemical studies. Annealing PtC deposits appears to be an excellent approach to gain the electrode characteristics of interest, however, this procedure induces unacceptable bending of AFM cantilevers when applied to AFM-SECM probes.

UV/ozone treatment and post-deposition FIB milling were evaluated as alternative procedures to improve the electron transfer rate particularly at AFM-SECM probes. Experimental results obtained during UV/ozone treatments indicate complex surface reaction mechanisms; a close inspection of these processes is beyond the scope of this thesis. FIB milling of PtC deposits directly after IBID leads to promising results indicating preferential sputtering of carbon when compared to platinum and gallium. Additionally, this procedure is compatible with AFM-SECM probes, and hence, will be

further evaluated in the following chapter utilizing IBID transducers with post-deposition treatment for advanced biosensor design.

This chapter demonstrated that PtC composite electrodes fabricated by IBID are an attractive approach for patterning individual and highly-confined electroactive features at a precise position. Future work to improve the understanding of IBID PtC materials should focus on a detailed study of the UV/ozone treatment process, and its influence on the electrochemical response. Additionally, as any generic PtC pattern may be deposited, this aspect should be further evaluated by fabricating e.g. fine grid structures, which could lead to a more significant increase of the observable steady-state current.

4.5 References

(1) Lin, J. F.; Bird, J. P.; Rotkina, L.; Bennett, P. A. *Classical and quantum transport in focused-ion-beam-deposited platinum nanointerconnects*, Appl. Phys. Lett. **2003**, *82*, 802-804.

(2) Sadki, E. S.; Ooi, S.; Hirata, K. *Focused-ion-beam-induced deposition of superconducting nanowires*, Appl. Phys. Lett. **2004**, *85*, 6206-6208.

(3) Li, P. G.; Jin, A. Z.; Tang, W. H. *Pt/Ga/C and Pt/C composite nanowires fabricated by focused ion and electron beam induced deposition*, Phys. Status Solidi A **2006**, *203*, 282-286.

(4) De Marzi, G.; Iacopino, D.; Quinn, A. J.; Redmond, G. *Probing intrinsic transport properties of single metal nanowires: Direct-write contact formation using a focused ion beam*, J. Appl. Phys. **2004**, *96*, 3458-3462.

(5) Hernandez-Ramirez, F.; Rodriguez, J.; Casals, O.; Russinyol, E.; Vila, A.; Romano-Rodriguez, A.; Morante, J. R.; Abid, M. *Characterization of metal-oxide nanosensors fabricated with focused ion beam (FIB)*, Sens. Actuators, B **2006**, *B118*, 198-203.

(6) Tham, D.; Nam, C.-Y.; Fischer, J. E. *Microstructure and composition of focused-ion-beam-deposited Pt contacts to GaN nanowires*, Adv. Mater. **2006**, *18*, 290-294.

(7) Vila, A.; Hernandez-Ramirez, F.; Rodriguez, J.; Casals, O.; Romano-Rodriguez, A.; Morante, J. R.; Abid, M. *Fabrication of metallic contacts to nanometer-sized materials using a focused ion beam (FIB)*, Mater. Sci. Eng., C **2006**, *26*, 1063-1066.

(8) Wagner, A.; Levin, J. P.; Mauer, J. L.; Blauner, P. G.; Kirch, S. J.; Longo, P. *X-ray mask repair with focused ion beams*, J. Vac. Sci. Technol., B: Microelectron. Nanometer Struct. **1990**, *8*, 1557-1564.

(9) Matsui, S.; Kaito, T.; Fujita, J.-i.; Komuro, M.; Kanda, K.; Haruyama, Y. *Three-dimensional nanostructure fabrication by focused-ion-beam chemical vapor deposition*, J. Vac. Sci. Technol., B: Microelectron. Nanometer Struct. **2000**, *18*, 3181-3184.

(10) Allameh, S. M.; Yao, N.; Soboyejo, W. O. *Synthesis of self-assembled nanoscale structures by focused ion-beam induced deposition*, Scr. Mater. **2004**, *50*, 915-919.

(11) Tao, T.; Wilkinson, W.; Melngailis, J. *Focused ion beam induced deposition of platinum for repair processes*, J. Vac. Sci. Technol., B: Microelectron. Nanometer Struct. **1991**, *9*, 162-164.

(12) Young, R. J.; Puretz, J. *Focused ion beam insulator deposition*, J. Vac. Sci. Technol., B: Microelectron. Nanometer Struct. **1995**, *13*, 2576-2579.

(13) Edinger, K.; Melngailis, J.; Orloff, J. *Study of precursor gases for focused ion beam insulator deposition*, J. Vac. Sci. Technol., B: Microelectron. Nanometer Struct. **1998**, *16*, 3311-3314.

(14) Folch, A.; Tejada, J.; Peters, C. H.; Wrighton, M. S. *Electron beam deposition of gold nanostructures in a reactive environment*, Appl. Phys. Lett. **1995**, *66*, 2080-2082.

(15) Edinger, K.; Gotszalk, T.; Rangelow, I. W. *Novel high resolution scanning thermal probe*, J. Vac. Sci. Technol., B: Microelectron. Nanometer Struct. **2001**, *19*, 2856-2860.

(16) Gopal, V.; Stach, E. A.; Radmilovic, V. R.; Mowat, I. A. *Metal delocalization and surface decoration in direct-write nanolithography by electron beam induced deposition*, Appl. Phys. Lett. **2004**, *85*, 49-51.

(17) Spoddig, D.; Schindler, K.; Roediger, P.; Barzola-Quiquia, J.; Fritsch, K.; Mulders, H.; Esquinazi, P. *Transport properties and growth parameters of PdC and WC nanowires prepared in dual-beam microscope*, Nanotechnology **2007**, *18*, 495202/495201-495202/495212.

(18) Tao, T.; Ro, J. S.; Melngailis, J.; Xue, Z.; Kaesz, H. D. *Focused ion beam induced deposition of platinum*, J. Vac. Sci. Technol., B: Microelectron. Nanometer Struct. **1990**, *8*, 1826-1829.

(19) Telari, K. A.; Rogers, B. R.; Fang, H.; Shen, L.; Weller, R. A.; Braski, D. N. *Characterization of platinum films deposited by focused ion beam-assisted chemical vapor deposition*, J. Vac. Sci. Technol., B: Microelectron. Nanometer Struct. **2002**, *20*, 590-595.

(20) Langford, R. M.; Wang, T. X.; Ozkaya, D. *Reducing the resistivity of electron and ion beam assisted deposited Pt*, Microelectron. Eng. **2007**, *84*, 784-788.

(21) Blauner, P. G.; Butt, Y.; Ro, J. S.; Thompson, C. V.; Melngailis, J. *Focused ion beam induced deposition of low-resistivity gold films*, J. Vac. Sci. Technol., B: Microelectron. Nanometer Struct. **1989**, *7*, 1816-1818.

(22) Della Ratta, A. D.; Melngailis, J.; Thompson, C. V. *Focused-ion beam-induced deposition of copper*, J. Vac. Sci. Technol., B: Microelectron. Nanometer Struct. **1993**, *11*, 2195-2199.

(23) Botman, A.; Mulders, J. J. L.; Weemaes, R.; Mentink, S. *Purification of platinum and gold structures after electron-beam-induced deposition*, Nanotechnology **2006**, *17*, 3779-3785.

(24) Langford, R. M.; Ozkaya, D.; Sheridan, J.; Chater, R. *Effects of Water Vapoyr on Electron and Ion Beam Deposited Platinum*, Microsc. Microanal. **2004**, *10*, 1122.

(25) Utke, I.; Hoffmann, P.; Dwir, B.; Leifer, K.; Kapon, E.; Doppelt, P. *Focused electron beam induced deposition of gold*, J. Vac. Sci. Technol., B: Microelectron. Nanometer Struct. **2000**, *18*, 3168-3171.

(26) Botman, A.; Hesselberth, M.; Mulders, J. J. L. *Improving the conductivity of platinum-containing nano-structures created by electron-beam-induced deposition*, Microelectron. Eng. **2008**, *85*, 1139-1142.

(27) Liao, Z.-M.; Xu, J.; Zhang, X.-Z.; Yu, D.-P. *The relationship between quantum transport and microstructure evolution in carbon-sheathed Pt granular metal nanowires*, Nanotechnology **2008**, *19*, 305402/305401-305402/305409.

(28) http://www.elchsoft.com/; **03/2009**.

(29) McCreery, R. L. *Advanced Carbon Electrode Materials for Molecular Electrochemistry*, Chem. Rev. **2008**, *108*, 2646-2687.

(30) Iliadis, A. A.; Andronescu, S. N.; Yang, W.; Vispute, R. D.; Stanishevsky, A.; Orloff, J. H.; Sharma, R. P.; Venkatesan, T.; Wood, M. C.; Jones, K. A. *Pt and W Ohmic contacts to p-6H-SiC by focused ion beam direct-write deposition*, J. Electron. Mater. **1999**, *28*, 136-140.

(31) Ferrari, A. C.; Robertson, J. *Interpretation of Raman spectra of disordered and amorphous carbon*, Phys. Rev. B: Condens. Matter Mater. Phys. **2000**, *61*, 14095-14107.

(32) Ferrari, A. C.; Robertson, J. *Raman spectroscopy of amorphous, nanostructured, diamond-like carbon, and nanodiamond*, Philos. Trans. R. Soc. London, Ser. A **2004**, *362*, 2477-2512.

(33) McCreery, R. L.; Cline, K. K. *Carbon Electrodes*, In *Laboratory Techniques in Electroanalytical Chemistry,* 2nd ed.; Kissinger, P., Heineman, W. R., Eds.; CRC Press, 1996, pp 293.

(34) McCreery, R. L. *Carbon Electrodes: Structural Effects on Electron Transfer Kinetics*, In *Electroanal. Chem.*; Bard, A. J., Ed.; Marcel Dekker: New York, 1991; Vol. 17.

(35) Chen, P.; McCreery, R. L. *Control of electron transfer kinetics at glassy carbon electrodes by specific surface modification*, Anal. Chem. **1996**, *68*, 3958-3965.

(36) Guilbault, G. G.; Lubrano, G. J. *Enzyme electrode for the amperometric determination of glucose*, Anal. Chim. Acta **1973**, *64*, 439-455.

(37) Hall, S. B.; Khudaish, E. A.; Hart, A. L. *Electrochemical oxidation of hydrogen peroxide at platinum electrodes. Part 1. An adsorption-controlled mechanism*, Electrochim. Acta **1997**, *43*, 579-588.

(38) Hall, S. B.; Khudaish, E. A.; Hart, A. L. *Electrochemical oxidation of hydrogen peroxide at platinum electrodes. Part II: effect of potential*, Electrochim. Acta **1998**, *43*, 2015-2024.

(39) Jin, C.; Zhou, H.; Graham, S.; Narayan, R. J. *In situ Raman spectroscopy of annealed diamondlike carbon-metal composite films*, Appl. Surf. Sci. **2007**, *253*, 6487-6492.

(40) Conway, N. M. J.; Ferrari, A. C.; Flewitt, A. J.; Robertson, J.; Milne, W. I.; Tagliaferro, A.; Beyer, W. *Defect and disorder reduction by annealing in hydrogenated tetrahedral amorphous carbon*, Diamond Relat. Mater. **2000**, *9*, 765-770.

(41) McCann, R.; Roy, S. S.; Papakonstantinou, P.; Bain, M. F.; Gamble, H. S.; McLaughlin, J. A. *Chemical bonding modifications of tetrahedral amorphous carbon and nitrogenated tetrahedral amorphous carbon films induced by rapid thermal annealing*, Thin Solid Films **2005**, *482*, 34-40.

(42) Liao, Z. M.; Xu, J.; Song, Y. P.; Zhang, Y.; Xing, Y. J.; Yu, D. P. *Quantum interference effect in single Pt(Ga)/C nanowire*, Appl. Phys. Lett. **2005**, *87*, 182112/182111-182112/182113.

(43) Goldstein, E. L.; Van de Mark, M. R. *Electrode cleaning and anion effects on ks for potassium ferricyanide couple*, Electrochim. Acta **1982**, *27*, 1079-1085.

(44) Bard, A. J.; Faulkner, L. R. *Electrochemical Methods: Fundamentals and Applications*, 2nd ed.; John Wiley & Sons, Inc.: New York, 2001.

(45) Wightman, R. M.; Wipf, D. O. *Voltammetry at Ultramicroelectrodes*, In *Electroanal. Chem.*; Bard, A. J., Ed.; Marcel Dekker, Inc.: New York, 1989; Vol. 15, pp 267-353.

(46) Martin, H. B.; Argoitia, A.; Landau, U.; Anderson, A. B.; Angus, J. C. *Hydrogen and oxygen evolution on boron-doped diamond electrodes*, J. Electrochem. Soc. **1996**, *143*, L133-L136.

(47) Yoo, K.; Miller, B.; Kalish, R.; Shi, X. *Electrodes of nitrogen-incorporated tetrahedral amorphous carbon. A novel thin-film electrocatalytic material with diamond-like stability*, Electrochem. Solid-State Lett. **1999**, *2*, 233-235.

(48) Zeng, A.; Liu, E.; Tan, S. N.; Zhang, S.; Gao, J. *Cyclic voltammetry studies of sputtered nitrogen doped diamond-like carbon film electrodes*, Electroanalysis **2002**, *14*, 1110-1115.

(49) Bennett, J. A.; Wang, J.; Show, Y.; Swain, G. M. *Effect of sp2-Bonded Nondiamond Carbon Impurity on the Response of Boron-Doped Polycrystalline Diamond Thin-Film Electrodes*, J. Electrochem. Soc. **2004**, *151*, E306-E313.

(50) Biegler, T.; Rand, D. A. J.; Woods, R. *Limiting oxygen coverage on platinized platinum; relevance to determination of real platinum area by hydrogen adsorption*, J. Electroanal. Chem. Inter. Electrochem. **1971**, *29*, 269-277.

(51) Zhou, J.; Wipf, D. O. *UV/ozone pretreatment of glassy carbon electrodes*, J. Electroanal. Chem. **2001**, *499*, 121-128.

(52) Gianuzzi, L. A.; Prenitzer, B. I.; Kempshall, B. W. *Ion-Solid Interactions*, In *Introduction to Focused Ion Beams: Instrumentation, Theory, Techniques and Practice*; Gianuzzi, L. A., Stevie, F. A., Eds.; Springer New York, 2005, pp 26.

5 TOWARDS THE APPLICATION OF AFM-SECM FOR IMAGING OF LIVE BIOLOGICAL SPECIMEN

In this chapter, the groundwork towards the imaging and detection of localized activity using scanning probe microscopy techniques in general and AFM-SECM in particular is described. Live epithelial cell monolayers are characterized by AFM. Additionally, ATP detection at epithelial cell monolayers is achieved with amperometric biosensors combined with non-invasive SECM, and laterally-resolved AFM-SECM. PtC deposits introduced in *Chapter 4* are further evaluated as electrode material for H_2O_2 detection, and as transducer platforms for glucose biosensors.

5.1 Motivation

Bifunctional AFM-SECM probes are exciting platforms for the incorporation of miniaturized biosensors. AFM tip-integrated amperometric glucose biosensors have been developed, and were used to image model surfaces enabling simultaneous topographical and electrochemical imaging of glucose membrane transport. However, depending on the targeted analyte and investigated sample surface, there are several challenges associated with using these devices; among those are the low signal (current) levels, and the dynamics and softness of complex biological samples, which render the experimental conditions challenging. Particularly for detection and localization of biologically-relevant

molecules at live cell surfaces more development is needed for reliable measurements in a routine regime.

Cellular surfaces are soft and dynamic biological entities, and prone to changes depending on their environment. Hence, biological samples require a thorough characterization within the targeted imaging environment prior to performing more complex chemical sample analysis. Reliable performance of miniaturized biosensors needs to be verified at a μm-sized level prior to implementation and further miniaturization for tip-integrated electrodes. Therefore, this section focuses on characterization and imaging of epithelial cells by AFM, and the development of suitable transducers and experimental conditions towards the detection of ATP at the surface of these cells.

5.1.1 Amperometric biosensors and scanning probe microscopy

The development of SECMs in the late 1980's[1-3] opened new doors for applications of biosensors. Horrocks et al. described the application of a H_2O_2 biosensor as a SECM probe[4]. Scanning miniaturized biosensors across sample surfaces enables imaging of biologically relevant processes. However, their use in conventional SECM is limited. Biosensing layers typically require electrode surface modification, which prevents conventional SECM positioning methods utilizing faradaic currents measured at UMEs, while approaching the sample surface. Hence, alternative positioning strategies have to be used, which will be discussed in the following. In the aforementioned example, Horrocks et al. positioned a H_2O_2 biosensor by measuring the solution resistance between tip and auxiliary electrode via application of a high-frequency alternating potential to the tip. Changes of the resistance in the vicinity of the sample surface may then be correlated

to the tip-to-sample distance. Alternatively, dual-UME assemblies have been introduced, where one UME is modified with a biosensing layer, while the second unmodified UME is used to position the sensing assembly at the sample surface via conventional feedback mode SECM[5]. As an example, a dual assembly was applied to locally detect ATP, and for laterally-resolved imaging of ATP transport through an artificial membrane[5]. However, this approach involved scanning the sample in constant height mode, which leads to convolution of topography and electrochemical activity in cases where the samples show significant topographical changes for example like single cells and cell assemblies.

As already described in *Section 2.2.2*, positioning of UMEs using shear force is an interesting approach to position and scan an UME in constant distance above a sample surface. This technique has been applied to electrochemical imaging with microbiosensors by Schuhmann and co-workers[6]. In their contribution, fiber-shaped glass capillaries were filled with either GOx or GDH entrapped in a hydrogel matrix. Subsequently, those probes were scanned across bare platinum (for GOx) or poly(methylene blue)-modified (for GDH) UMEs.

As discussed in earlier sections of this thesis, another possibility to achieve constant distance between electrodes and surfaces is the integration of AFM and SECM technology. *Figure 5.1* shows a schematic of such an AFM tip-integrated biosensor illustrating the signal generation. Tip-integrated glucose biosensors have been used to monitor glucose diffusion through a track-etched model membrane[7]. Glucose diffusion could also be quantified by application of a single pore model, and prior calibration of the tip-integrated glucose sensor. In addition, a tip-integrated H_2O_2 biosensor based on horseradish peroxidase immobilized at the electrode was applied for localized detection

of H_2O_2[7, 8]. Both approaches have exclusively been applied to electrochemical imaging of model substrates so far. Summarizing, extensive studies using SECM with biosensors have not been performed to date.

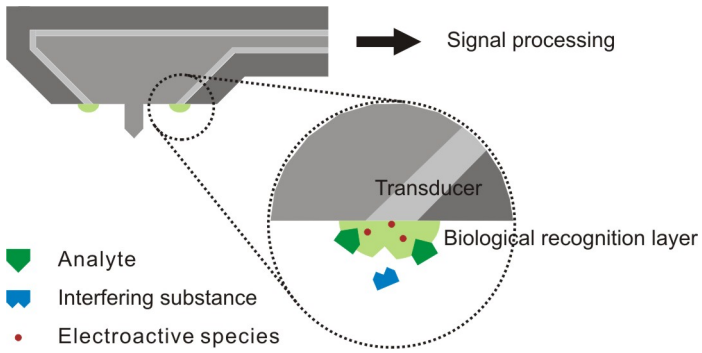

Figure 5.1. Schematic of AFM tip-integrated biosensor.

Consequently, AFM tip-integrated ATP biosensors for the detection of ATP at live epithelial cell monolayers were fabricated. *Figure 5.2* shows representative initial measurements. The AFM-SECM probe used was a FIB-fabricated probe with an electrode edge length of 1.5 µm (width: 0.1 µm). Experimental details for the fabrication of the biosensor are described in detail in *Section 5.2.2*. As described in *Section 2.1.3*, the biosensor is based on the competitive enzyme reaction of GOx and HEX, and due to the involved reactions (*Equations (2.14)* - *(2.16)*) the presence of ATP leads to a current decrease. However, as revealed in the current image (*Figure 5.2B*), no detectable current response from the biosensor was obtained.

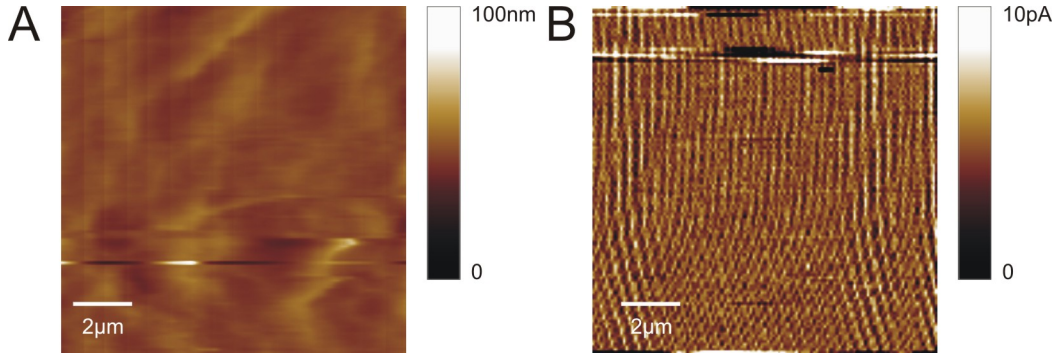

Figure 5.2. Representative AFM-SECM experiment obtained with AFM tip-integrated ATP biosensor during initial studies at live epithelial cell monolayer showing topography (A), and current (B). Electrode was biased at 0.65 V vs. AgQRE, and imaging was performed in PBS solution (pH 7.4) containing 3 mM glucose and 5 mM $MgCl_2$. A FIB-fabricated probe was utilized with a tip length of 1.1 µm and a frame edge length of 1.5 µm, and the scan rate was 0.501 lines s^{-1} at an original scan size of 25 × 25 $µm^2$.

This result demonstrates that the size of an unmodified tip-integrated electrode is insufficient for immobilizing sufficient quantities of biomolecules close to the electrode surface, thus not providing a resolvable current signal from the biosensor. Extrapolating the saturation current obtained at UME-based ATP biosensors (diameter: 25 µm; i_{sat} ~ 30 - 40 pA)[9] indicates that current levels expected at unmodified tip-integrated ATP biosensors are in the low pA to sub-pA range. This once more emphasizes the necessity for increasing the tip-integrated electrode area in order to obtain detectable current levels.

5.2 Experimental

5.2.1 Cell cultures

Cell samples were cultured at Emory University at the Department of Physiology (in collaboration with Dr. Douglas C. Eaton). Highly transporting 2F3 epithelial cells, which are a clone of the A6 epithelial cell line derived from the distal nephron of Xenopus laevis, were used as model cell system throughout this thesis.

Cell cultures were prepared as described elsewhere[10]. Briefly, cell culture media consisted of a 50 % (v/v) mix of DMEM and Ham's F-12 medium adjusted to amphibian tonicity additionally adding 0.6 % penicillin, 1.0 % streptomycin, 5 % (v/v) fetal bovine serum, 1.5 μM aldosterone (Fisher Scientific, Pittsburgh, PA), 1 mM glutamine, and 25 mM $NaHCO_3$ (Fisher Scientific). Confluent cells were detached from T-75 flasks (Corning, Lowell, MA) with 0.05 % Trypsin-EDTA enzymatic dissociation solution. In the following, the cells were rinsed, centrifuged, repeatedly resuspended, and plated onto tissue culture inserts (part# 161395, Nunc, Rochester, NY) for all further experiments. Cells were incubated at 26 ºC and 4 % CO_2, and nurtured every other day with fresh medium. All chemicals and solutions used during culturing were obtained from Invitrogen (Carlsbad, CA), unless otherwise noted.

On the 7th day after plating, the cells were transported to the Georgia Institute of Technology, and kept at the same incubating conditions until experiments were performed. A new cell passage was obtained every week at approx. 100 % confluency, and cell passage numbers of 96 to 105 were used.

5.2.2 Electrochemical techniques

UMEs used for PtC experiments were prepared as described in *Section 4.2*. PtC layers were either left pristine or pretreated after the deposition, and then immediately used for H_2O_2 sensing experiments or for glucose biosensor preparations. Dual-barreled UMEs as transducers for ATP biosensing experiments were prepared by sealing platinum microwires (diameter 25 μm, Goodfellow, U.K.) into theta borosilicate glass capillaries (Hilgenberg, Germany). After encapsulation, the electrode surfaces were ground/polished, as described in *Section 4.2.4*. Electrical connection to platinum

microwires was established with copper magnet wires, and two-component silver conductive epoxy (same as in *Section 3.2.3*). CVs were performed to confirm electrical separation of the two UMEs in the assembly. Prior to enzymatic modifications, dual-UMEs were briefly re-polished, sonicated, and cleaned in 0.5 M H_2SO_4 (same cleaning sequence as described in *Section 4.2.4*). Platinum counter electrodes and Ag/AgCl or SCE reference electrodes were used throughout all experiments, unless otherwise stated.

For enzyme immobilization, two different types of electrodeposition paints were used, namely Glassophor ZQ 8-43225 Canguard (BASF, Germany) and Resydrol AY498w/35WA (Cytec, Smyrna, GA). EDP-enzyme solutions were prepared using a final pre-polymerization solution concentration of 70 μL (EDP) mL^{-1} (HPLC grade water), and 600 U (enzyme) mL^{-1} (HPLC grade water). Glucose oxidase from aspergillus niger (Type X-S), and hexokinase from yeast overproducer were obtained from Sigma (St. Louis, MO) and Roche Applied Science (Indianapolis, IN), respectively, and HPLC grade water was obtained from J. T. Baker (Phillipsburg, NJ). All solutions were prepared separately and mixed to the resulting final concentrations noted above before polymerization. For glucose biosensors, EDP-water solutions and GOx-water solutions were prepared, and mixed together before storage in ice for 30 min before the polymerization. In the case of ATP biosensors, HEX-EDP-water solutions were additionally mixed after cooling the EDP-water solution for 25 min. Similar to the glucose sensor, after a period of 30 min the polymerization was performed after mixing the GOx-EDP-water and the HEX-EDP-water suspensions in a 1:1 ratio. Pulsed potential profiles applied for the precipitation depended on the used EDP, and were 2.2 V for 0.2 s, 0.8 V for 1 s, and 0 V for 5 s or 1.9 V for 0.2s, and -0.3 V for 5 s in the case of Canguard

or Resydrol, respectively. The number of deposition cycles was varied from 1 - 5 depending on the biosensor. After polymerization, the biosensors were dipped in cold phosphate buffered saline (PBS, pH 7.4; Invitrogen, Carlsbad, CA) for removal of un-precipitated EDP-enzyme residues, and stored in PBS at 4 ºC for at least 1 h prior to use.

PtC UME-based calibrations for H_2O_2 (Sigma-Aldrich, St. Louis, MO) and glucose (Fluka, St. Louis, MO) biosensors were obtained by constant potential amperometry at 0.65 V vs. SCE, and addition of H_2O_2 or glucose, respectively. After each addition, the solution was gently mixed generating some noise observed in the presented current plots. PtC UMEs were recycled after each experiment, as mentioned in *Section 4.2.4*.

5.2.3 Scanning probe techniques

The same AFM and AFM-SECM setup described in *Section 3.2.3* was used for all studies. For AFM imaging of epithelial cell surfaces, an approx. $2 - 3\ cm^2$ sized cell sample was obtained from the tissue culture insert by gently breaking the cell substrate with ethanol-cleaned tweezers. Cells were washed with PBS and mounted in the AFM liquid cell. AFM cell imaging was performed in PBS solution with silicon nitride tips (Veeco, Woodbury, NY) for both contact and dynamic mode measurements. Typically, the resonant frequency of the utilized silicon nitride cantilevers in liquid is the range of 43 kHz.

AFM-SECM probes were either fabricated as described in *Section 3.2.1*, or obtained by a batch-fabrication process developed in our research group[11, 12]. Prior to experiments, the AFM-SECM probe quality was tested recording CVs in a reversible redox mediator solution and the probes were then mounted in the AFM nose cone assemblies. The cells were placed on the AFM stage, as previously described. AFM-SECM feedback imaging

was performed in 5 mM $Fe(CN)_6^{3-/4-}$ and PBS solution. During low-force contact mode imaging, the AFM probe was retracted from the sample surface until force impact was minimized. AFM tip-integrated ATP biosensors were prepared with one deposition cycle following the procedure described in *Section 5.2.2*. ATP biosensing experiments at live epithelial cells were performed in PBS solution containing 5 mM $MgCl_2$ (Fluka, St. Louis, MO) and 3 mM glucose. For control experiments, the PBS/$MgCl_2$/glucose solution in the AFM flow cell was exchanged with a HEX solution at a concentration of 5 U mL^{-1} in PBS/$MgCl_2$/glucose.

Typically, AFM images were post-processed via flattening of the background. In some cases, for electrochemical images, Fourier filtering was performed to remove the line frequency at 60 Hz, or the data was smoothed.

SECM measurements were conducted utilizing a home-build setup located in a Faraday cage (Warner Instruments, Hamden, CT). The SECM consists of a micropositioning system (SPI Scientific Precision Instruments, Oppenheim, Germany) combined with a sample stage, and potentiostats from CH instruments (*Section 3.2.4*). The SECM is controlled via an AD/DA board (DAS1602-16, Plug-In-Electronic, Eichenau, Germany) with a personal computer. The software that controls the positioning system, and enables data acquisition was developed by Dr. Gunther Wittstock (University of Oldenburg, Germany).

All SECM and AFM-SECM measurements were performed in a three-electrode setup. A platinum counter electrode was used, and all potentials are reported against AgQRE. The dual-UME acted as the working electrode; for positioning the bare platinum wire (WE 2)

was biased at -0.52 V, and for ATP biosensing the biosensor (WE 1) at 0.65 V. The solution used during all experiments was PBS with 5 mM $MgCl_2$ and 5 mM glucose.

WE 1 was modified with a biosensing layer, as described in *Section 5.2.2* applying three deposition cycles. Prior to SECM experiments, the ATP biosensors were calibrated by constant potential amperometry via addition of ATP (Aldrich, St. Louis, MO) to the solution. For SECM experiments, epithelial cells were mounted in a custom-build cell, and partially covered by a 50 µm thick plastic film. The dual-UME device was mounted in the SECM setup, and approached to the plastic film (velocity 1.6 µm s^{-1}) by biasing WE 2 at -0.52 V vs. AgQRE for the reduction of oxygen. After detection of a negative feedback signal, the z-approach was stopped at approx. 90 % of the current measured in bulk. For ATP biosensing above epithelial cells, a line scan was recorded (velocity 1.6 µm s^{-1}) while biasing WE 1 at 0.65 V vs. AgQRE for the oxidation of H_2O_2. After control experiments were performed by adding free HEX to solution (two times 5 µL) resulting in a final concentration of approx. 70 U mL^{-1}, the same volume of PBS/$MgCl_2$/glucose was added to the liquid cell to investigate any cross interferences.

5.3 Results and discussion

5.3.1 AFM imaging of epithelial cell monolayers

Atomic force microscopy is a versatile tool for high-resolution imaging of live cell surfaces in physiological solutions. However, optimization of AFM imaging conditions is required for each individual type of live samples prior to extended investigations for characterizing these soft and dynamic biological entities at their particular culturing conditions.

AFM imaging of epithelial cells was performed in contact mode and dynamic mode operation. *Figure 5.3* shows typical topographical images acquired in contact mode AFM. The images are flattened with a 4th order flattening function. In general, the z-scale of flattened images does not represent true height variations of the surface. True height variations of epithelial cell monolayers are typically in the range of 0.5 - 4 µm depending on the scanned image size. Polygonal cell shapes of individual cells within the monolayer are observed. Cell borders between neighboring cells clearly form resolvable tight junctions similar to results obtained at A6 epithelial cell layers published in literature[13]. Mechanical impact of the AFM probe on the soft cell sample surface was evaluated by continuous scanning at the same sample spot. It could be observed that the structures at the cells remain essentially unaltered despite continuous scanning over a time period of 1.5 hrs; representative images after a period of 26 min are shown in *Figure 5.3B*. However, the middle sections of the single cells are indented during imaging in respect to the surrounding cell borders.

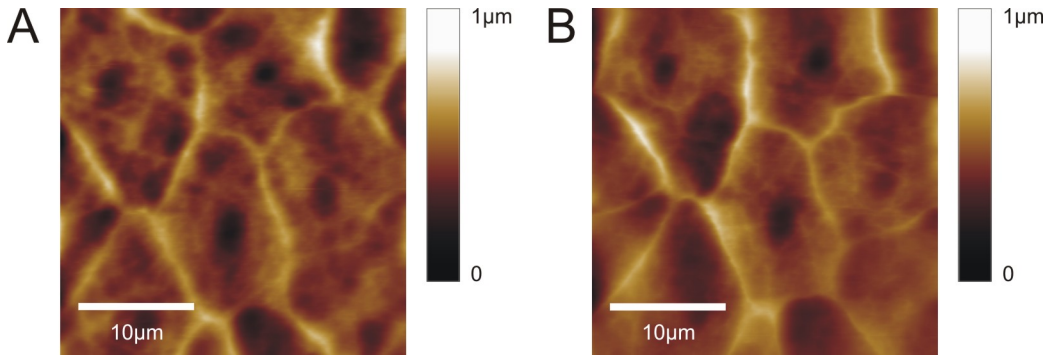

Figure 5.3. Topographical AFM images of live epithelial cells in PBS solution acquired in contact mode operation. Continuous imaging was performed and images at the beginning (A) and after 26 min (B) are shown (scan rate: 0.815 lines s^{-1}). Images are flattened with a 4th order flattening function.

Imaging of soft sample surfaces is frequently performed in dynamic mode AFM, since the reduced tip-sample contact time results in minimization of force impact[14-16]. *Figure 5.4* shows representative images obtained in dynamic mode AFM at live cell surfaces, while varying the amplitude setpoint. It can be clearly demonstrated that an amplitude ratio ($A_{surface}/A_{free}$) of 0.77 (*Figure 5.4A*) reduces the force impact: the middle section of single cells is not indented, however, less features are resolved. Increasing the force during dynamic mode imaging (amplitude ratio of 0.67) of the same sample spot results in more pronounced feature representation (*Figure 5.4B*), yet, the cell membranes appear indented in comparison to the cell borders, as similarly observed during contact mode imaging (*Figure 5.3*). Hence, there is an optimized balance between achieving sufficient resolution of cell features, and minimizing indenting cell surfaces during imaging.

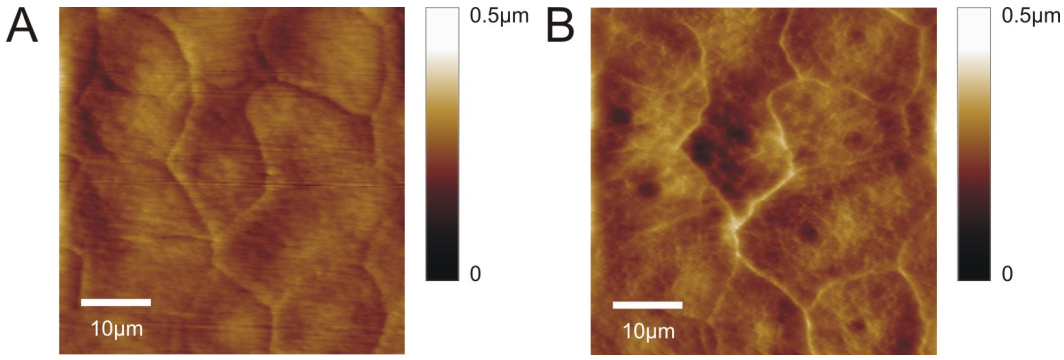

Figure 5.4. Topographical AFM images of live epithelial cells acquired during dynamic mode operation in PBS solution. The amplitude ratio ($A_{surface}/A_{free}$) was varied from 0.77 (A) to 0.67 (B). The resonant frequency was approx. 43 kHz, and the scan rate was 0.798 lines s^{-1}. The images are flattened with a 4th order flattening function.

However, dynamic mode imaging with AFM tip-integrated biosensors at cell surfaces appears less favorable, as vibration of the cantilever at its resonance frequency may affect tip-integrated biosensors due to limited mechanical stability of the biosensing layer

adsorbed at the transducer surface. This effect is presumably less pronounced for non-resonating AFM probes. Thus, at the present development stage CM AFM was used for biosensing studies at live epithelial cells until the mechanical stability of the sensing architectures at the electrode surface is further advanced.

Structural changes at cell surfaces occurring over a certain time period after plating were monitored in an effort to determine the optimum time frame for AFM imaging. *Figure 5.5* shows representative contact mode images acquired at different days at cells from the same cell passage. The large area AFM scans do not show any apparent differences between the 7^{th} and 11^{th} day after plating. However, it should be noted that larger accumulations of dead cells were detected on top of the cell monolayer at longer periods of time after plating. Cell imaging was therefore typically performed between the 8^{th} and the 10^{th} day after plating.

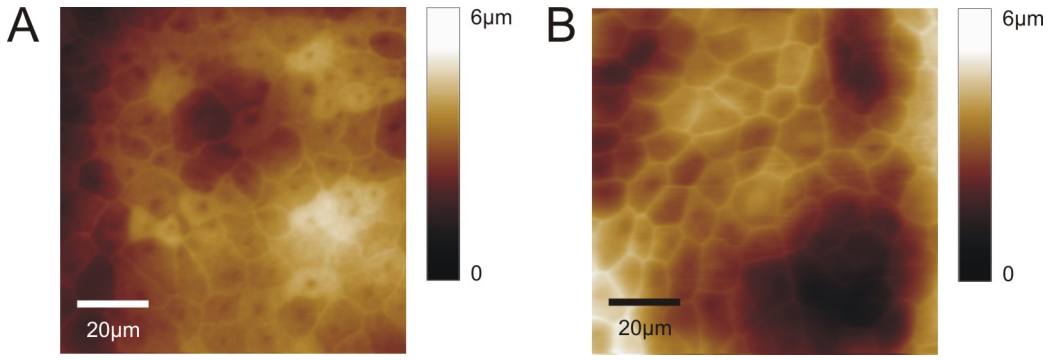

Figure 5.5. Topographical AFM images of live epithelial cells in PBS solution acquired in contact mode. Images obtained on the 7^{th} (A) and the 11^{th} (B) day after plating are depicted. The scan rate was 0.501 lines s^{-1} (A), and 0.553 lines s^{-1} (B). Raw images are shown.

5.3.2 AFM-SECM feedback imaging

As already discussed in earlier sections of this work, combined AFM-SECM has the strength of deconvoluting the electrochemical signal from topographical influences. However, signal deconvolution is still presumably influenced by sample properties such as stiffness, roughness, and the dimension of surface features.

AFM topographical studies reveal that height variations of epithelial cell monolayers have typical dimensions in the 0.5 - 4 µm range. Since cell surfaces are soft structures, it is advisable to perform AFM-SECM imaging at live cell monolayers in SECM feedback mode to evaluate the possibility of current contributions from topographical features. $Fe(CN)_6^{3-/4-}$ was used during these studies, since lipid cell membranes are impermeable for hydrophilic redox mediators[17]. Consequently, negative feedback is observed with hydrophilic mediators, as the diffusion to the UME is blocked in the vicinity of the cell membrane. This was confirmed while approaching the AFM-SECM probes to the cell surface. *Figure 5.6* shows representative topography (*A, C*), and current (*B, D*) images obtained during these experiments. The tip-integrated electrode was biased at 0.6 V (*A, B*) or 0 V vs. AgQRE (*C, D*). Again, the z-scale in the topographical images is not representative of the real height variations, since a 4^{th} order flattening function was used for enhanced graphic representation of the image.

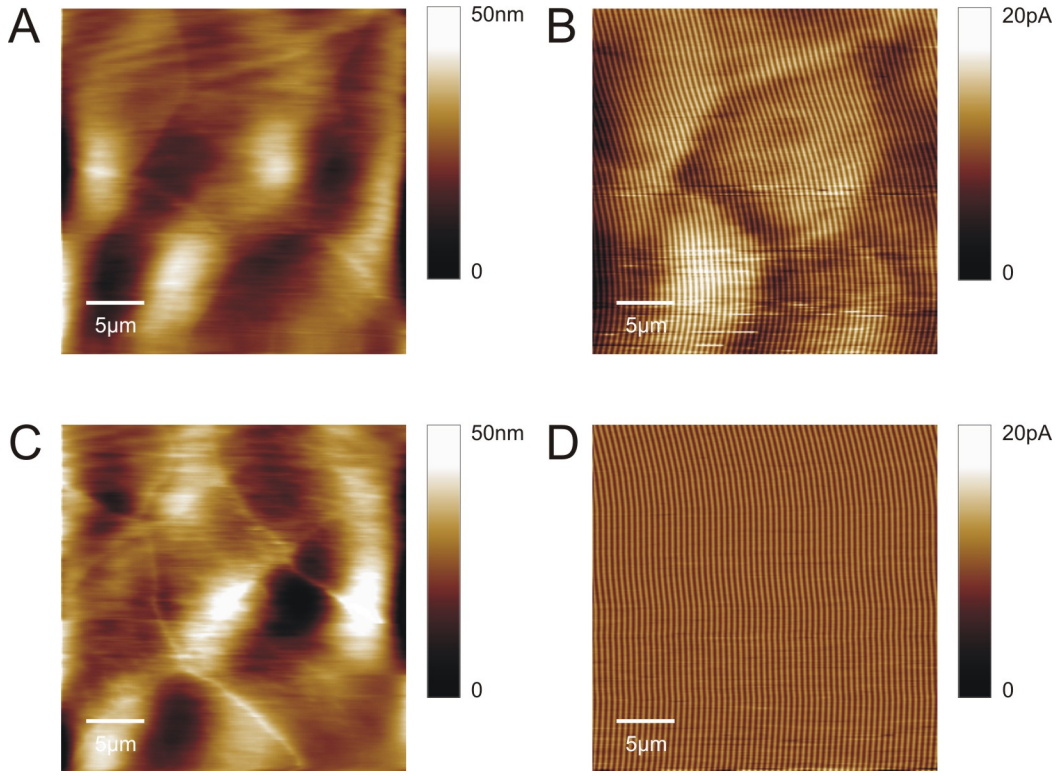

Figure 5.6. Simultaneously recorded topography (A, C), and current images (B, D) at live epithelial cells in AFM contact mode, and SECM feedback mode. The tip-integrated electrode was biased at 0.6 V (A, B) and 0 V (C, D) vs. AgQRE, and scanned in 5 mM $Fe(CN)_6^{3-/4-}$ and PBS solution (scan rate: 0.501 lines s^{-1}). AFM tip length of the FIB-milled probe was 0.78 µm, and the frame electrode edge length was 2.04 µm. Topographical images were flattened with a 4^{th} order flattening function.

It is evident that the current image (*Figure 5.6B*) shows features matching the morphology of the cells (*Figure 5.6A*). This implies that the topography recorded in conventional contact mode AFM is convoluted with the SECM feedback current response in those experiments. As mentioned before, flattened topographical images as shown in *Figure 5.6* do not represent the real height variation across the sample surface. Raw data images of the topography reveal a similar height of the topographical features (approx. 0.5 - 1 µm), which are comparable to the length of the FIB-milled AFM tip (0.78 µm). Hence, CM imaging at higher forces requires a tip length significantly larger than the

feature size. No SECM feedback image is obtained during control experiments recorded at 0 V, since there is no considerable oxidation of $Fe(CN)_6^{3-/4-}$ at this applied potential.

Additional to dynamic mode AFM, low-force contact mode AFM has been described as an alternative operational mode particularly useful for studies at soft biological materials, since it may significantly reduce the force impact on the sample surface[18, 19]. *Figure 5.7* shows AFM-SECM topography and current images recorded while reducing the force applied to the sample. Again, the images were flattened, thus the z-scale is not representative of the true height variation (which was on the order of 0.5 - 1 μm). The force was reduced during image acquisition at the location, which is marked by the asterisk. The tip-integrated electrode was biased at 0.6 V vs. AgQRE, and $Fe(CN)_6^{3-/4-}$ was used as redox mediator. It can be seen that smaller topographical current effects are observed after minimizing the force impact. However, the topography of the image is also deteriorated at this point. Although further optimization of topographical imaging is required, this observation is nevertheless encouraging illustrating the potential of this alternative low-force impact AFM mode. Although dynamic mode AFM-SECM has been successfully demonstrated without impairing the tip current or image quality at model samples[20], it is not practical for initial studies toward the integration of tip-integrated biosensors, as described earlier. However, once the biosensor architecture is improved, this imaging mode should be revisited.

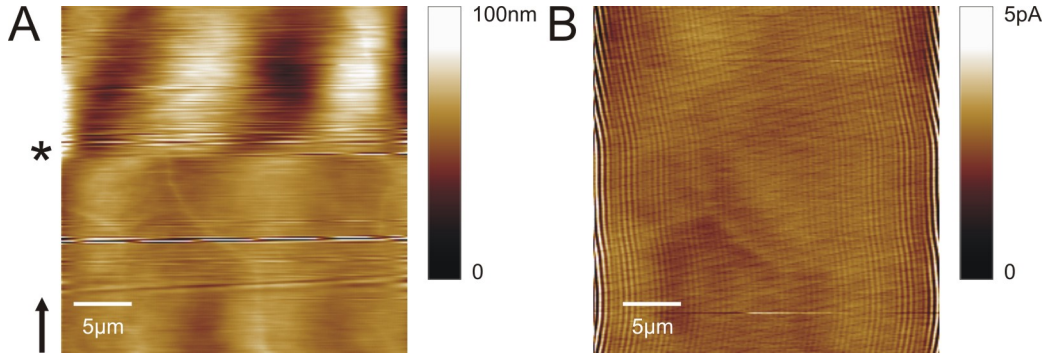

Figure 5.7. Topography (A) and current (B) images of live epithelial cells obtained in AFM contact mode and SECM feedback mode. The tip-integrated electrode was biased at 0.6 V vs. AgQRE, and scanned in 5 mM $Fe(CN)_6^{3-/4-}$ and PBS solution (scan rate: 0.501 lines s^{-1}). The asterisk marks when the force was reduced, and the arrow indicates the scan direction. The FIB-milled AFM probe had a tip length of 0.78 µm, and a frame electrode with an edge length of 2.04 µm. The topographical image was flattened with 4th order flattening function.

5.3.3 SECM-based detection of ATP at epithelial cells

As already mentioned in *Section 5.1.1*, positioning and distance control of UME-based sensors at sample surfaces is challenging, as the change in faradaic current when approaching the surface is of limited accessibility with modified electrodes. One approach reported during conventional SECM experiments is the application of dual-UME assemblies[36, 37]. In this configuration, one UME is modified with the sensing layer, whereas the second UME is left unmodified for positioning. In our research group, Kueng et al. have developed a dual-UME based ATP biosensor, and have imaged ATP transport through a porous membrane in SECM operation[5]. ATP detection is based on a competitive enzymatic reaction of GOx and HEX for the substrate glucose[21-23]. Both enzymes are co-immobilized in an EDP layer at the electrode surface deposited via electrochemically-induced pH-shift[9, 24, 25]. Anodic EDPs used within this work contain negatively charged groups such as carboxylic side chains, which are protonated due to a localized generation of H^+ at the electrode surface. This pH change induces a drastic

change in solubility, and consequently results in polymer precipitation along with inclusion of the enzymes present in the polymerization solution.

Based on the detection scheme discussed in *Equations (2.14)* - *(2.16)*, addition of glucose results in a current increase due to the GOx-catalyzed formation of H_2O_2. Correspondingly, at a constant concentration of glucose, ATP addition leads to a proportional current decrease, since there is less glucose available. Units of GOx and HEX are kept at a ratio of 1:1. Mg^{2+} is added as $MgCl_2$, which is a co-factor for the HEX-catalyzed reaction. Oxygen is a co-substrate during the GOx-catalyzed reaction. Interestingly, it could be shown that depleted (approx. 1 ppm) oxygen concentrations did not influence the current response of the biosensor when compared to oxygen levels resulting from equilibration at air (approx. 6 ppm)[9], implying that experiments are independent of oxygen level variations in that range.

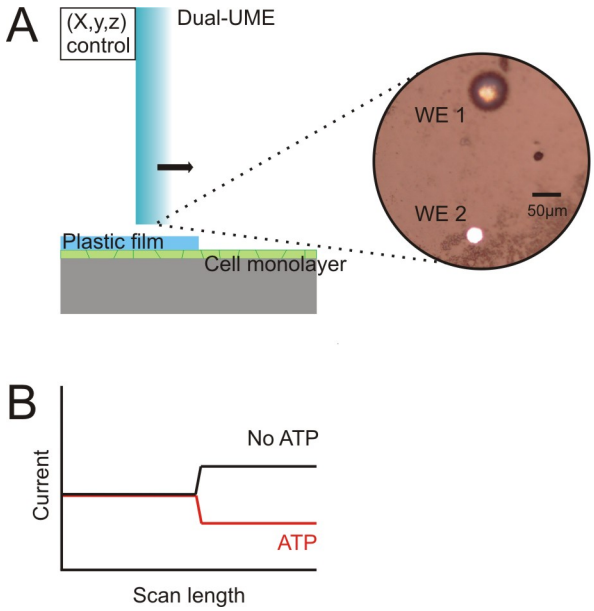

Figure 5.8. (A) Schematic SECM setup illustrating a dual-UME line scan across an edge between plastic film and cell monolayer. The optical micrograph shows the top view of a representative dual-UME with EDP layer (WE 1), and unmodified UME (WE 2). (B) Expected current response after scanning across the edge.

It is known that cells may react to mechanical stress, and it is hypothesized that for epithelial cells mechanical stimulation may contribute to the localized release of ATP. Thus, it is of interest to further investigate possibilities of non-invasive ATP detection. Therefore, dual-UME based ATP biosensors[5] were used to confirm ATP release at live epithelial cell monolayers during non-invasive SECM operation. Dual-UMEs were scanned across an edge between a plastic film and a cell monolayer in constant height SECM (*Figure 5.8*). The step was designed such that the distance between the UME and the sample increases once the UME is located above the cell monolayer. Because of this design, a current decrease after scanning across the edge can solely be attributed to the presence of ATP. In case there is no ATP released, a current increase is expected since glucose diffusion is enhanced due to an increased electrode-sample distance. The magnified section in *Figure 5.8A* shows a representative optical micrograph of the dual-

UME assembly revealing the EDP layer with entrapped enzymes (WE 1, ATP biosensor), and the unmodified UME used for approaching to the surface (WE 2).

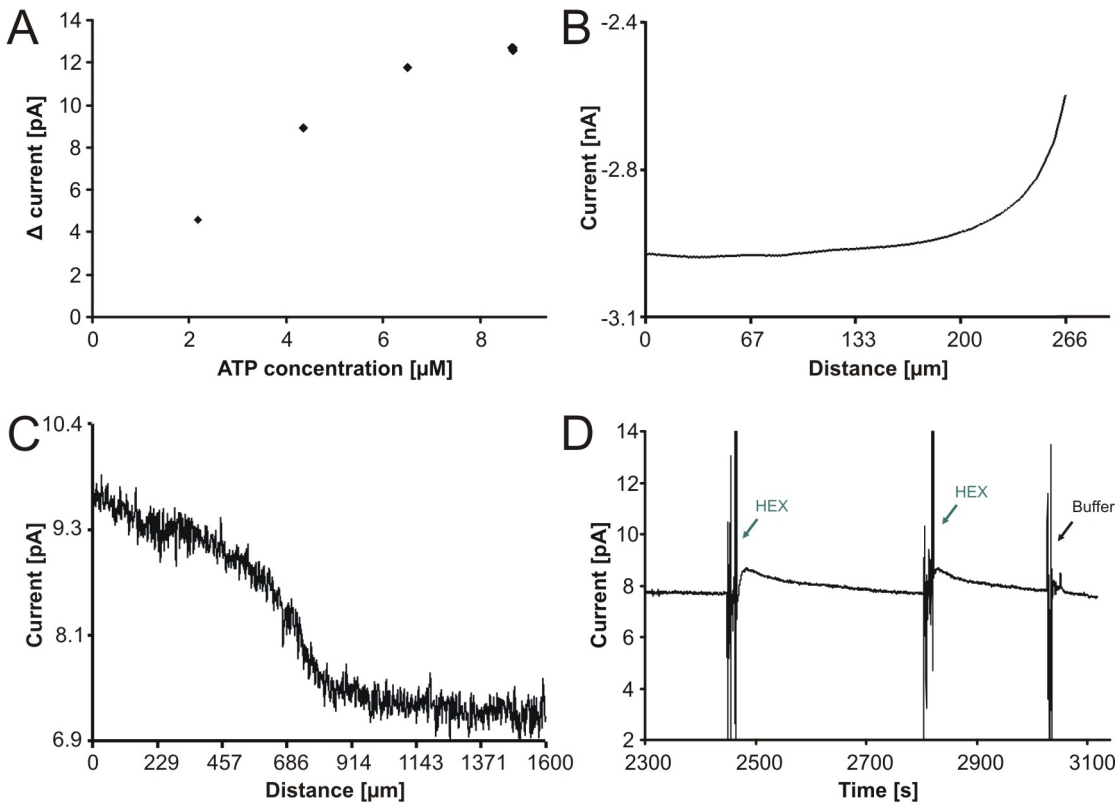

Figure 5.9. (A) ATP calibration curve obtained from amperometric response curve at an ATP biosensor during addition of ATP (WE 1, biased at 0.65 V). (B) Approach curve used to position dual-UME above the plastic film; WE 2 was biased at -0.52 V for the reduction of oxygen. Note that the scale is negative. (C) Line scan recorded with ATP biosensor (WE 1; E = 0.65 V) while scanning the dual-UME across the edge between the plastic film and the cell monolayer. (D) Control experiment illustrating the amperometric current recorded at the ATP biosensor (WE 1; E = 0.65 V) positioned above the epithelial cell layer while adding HEX and buffer. All measurements were performed in PBS solution at pH 7.4 containing 5 mM glucose and 5 mM $MgCl_2$ and all potentials are reported against AgQRE.

Figure 5.9A shows a representative calibration curve obtained at a dual-UME based ATP biosensor (WE 1). After calibration, the dual-UME was approached to the surface of the plastic film while biasing the unmodified UME (WE 2) at -0.52 V monitoring the reduction of oxygen. As expected, a negative feedback effect can be observed in close

proximity to the plastic film in the amperometric approach curve (*Figure 5.9B*). After positioning, the dual-UME was scanned in constant height across the edge (film thickness of 50 µm) towards the surface of the epithelial cells. The current signal recorded while biasing the biosensor at 0.65 V (WE 1) is plotted in *Figure 5.9C.* The expected decrease in current after passing the edge between the film and the cells was recorded indicating the presence of ATP. ATP detection was further confirmed in a control experiment while the sensor was positioned at the cell surface by adding an excess of HEX to the solution (*Figure 5.9D*). After the addition of free-diffusing HEX, a corresponding current increase was observed since free-diffusing HEX depletes ATP present in solution faster than the immobilized HEX in the EDP. Due to the decrease in ATP concentration, more glucose was available for the GOx-catalyzed conversion of glucose, and hence, an increased amount of H_2O_2 induced a current increase. As expected, addition of buffer did not result in any change of current level. This study clearly shows that ATP release from the epithelial cell monolayer may be detected with the proposed ATP biosensor. However, it is also evident that due to the limited resolution of the UME no variations in ATP level could be observed. Thus, further miniaturization has to be performed to investigate whether there are localized differences in ATP release patterns.

5.3.4 AFM-SECM tip-integrated ATP biosensors

Further miniaturization of the ATP biosensors was performed by deposition of the enzyme containing EDP layer onto batch-fabricated AFM-SECM probes[11, 12]. Batch-fabricated AFM-SECM probes have tip-integrated ring electrodes with typical inner diameters of 2.7 µm and ring widths of 0.7 - 2.6 µm[11], which is a significantly increased electrode area compared to FIB-based AFM-SECM probes. *Figure 5.10* shows an SEM

image of such a combined AFM-SECM probe. By using these batch-fabricated probes laterally-resolved imaging of ATP release at the surface of live epithelial cells was performed for the first time.

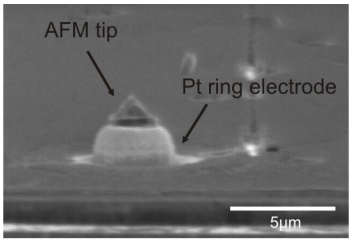

Figure 5.10. SEM image of batch-fabricated AFM-SECM probe showing electrode and tip shape.

Figure 5.11 shows representative topographical and electrochemical images obtained with a tip-integrated ATP biosensor at the model cell system. The tip-integrated electrode was biased at 0.65 V (vs. AgQRE) to oxidize enzymatically produced H_2O_2. Reactions catalyzed by the enzymes are the same, as presented in *Section 2.1.3* (*Equations (2.14) - (2.16)*). The electrochemical image in *Figure 5.11B* reveals areas of localized current decrease (selected areas are marked with red ellipses), which may correspond to elevated levels of ATP. Moreover, similar cell shapes reported during conventional AFM imaging of epithelial cells are resolvable with the AFM tip-integrated biosensor.

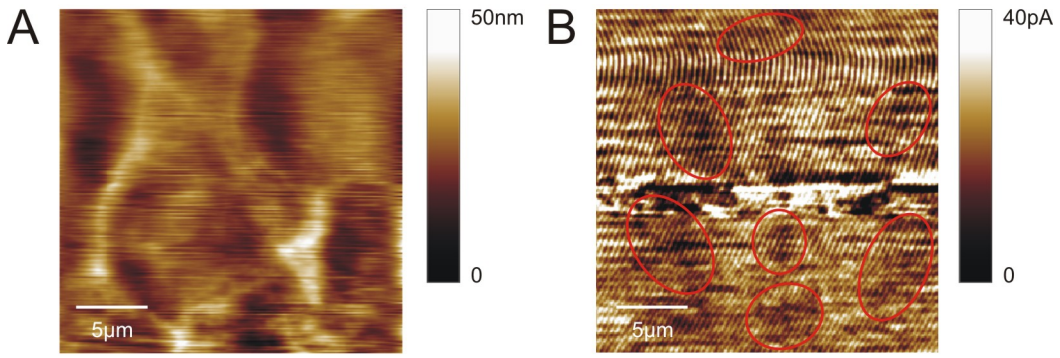

Figure 5.11. Simultaneously recorded topography (A) and current (B) at the surface of live epithelial cells while biasing AFM tip-integrated ATP biosensor at 0.65 V (vs. AgQRE). Red ellipses mark areas of localized current decrease. Imaging was performed in PBS solution (pH 7.4) containing 3 mM glucose and 5 mM $MgCl_2$ (scan rate: 0.501 lines s^{-1}, original scan size: 25 × 25 µm^2). The batch-fabricated AFM tip had a length of 1.58 µm and an inner/outer electrode radius of 2.43/5.68 µm. Topographical image flattened with a 4th order flattening function.

A control experiment similar to the one described in *Section 5.3.3* was performed. An excess of free-diffusing HEX was added to the AFM liquid flow cell, while scanning the sensor across the epithelial cell monolayer surface. *Figure 5.12* shows the amperometric response curve recorded at the biosensor during addition of HEX and corresponding electrochemical images before and after the addition of the free-diffusing enzyme. Similar to the SECM cell experiments, an addition of excess HEX confirmed the presence of ATP inducing a current increase due to the fact that more glucose (and consequently more H_2O_2) was present because of the consumption of ATP in solution. Moreover, the electrochemical image shows only random noise after the addition of HEX but a uniform current level, indicating no localized variation of the ATP levels. The detection of cellularly-secreted ATP at a bi-enzymatic tip-integrated biosensor is complex in nature, as the current levels detected are in the pA range, and since the biosensors have to be calibrated prior to experiments. Furthermore, the signal generation is based on a mixed generation-collection/feedback mode experiment. Hence, appropriate control

experiments are needed accounting for all variable experimental parameters including the force impact during AFM imaging, while maximizing the sensor response and minimizing the noise during the measurements.

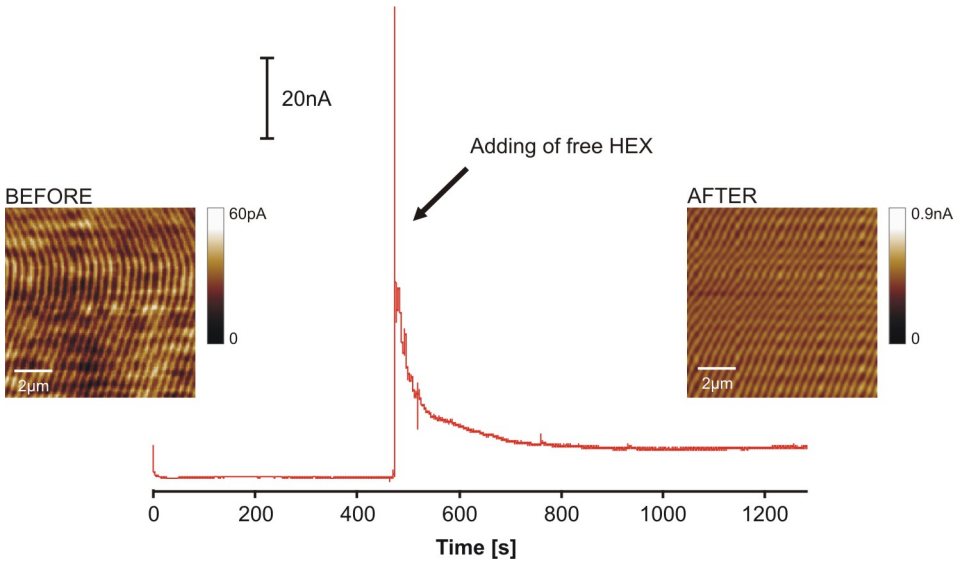

Figure 5.12. Control experiment showing the amperometric response curve recorded at a tip-integrated ATP biosensor at an electrode bias of 0.65 V (vs. AgQRE), when the sensor is positioned above the epithelial cells. Additionally simultaneously recorded electrochemical images are shown before and after adding of the free-diffusing HEX. Experiments were performed in PBS solution (pH 7.4) containing 3 mM glucose and 5 mM $MgCl_2$. The same AFM probe as in Figure 5.11 was used. The scan rate was 0.501 lines s^{-1} (original scan size: 25 × 25 μm^2).

5.3.5 Batch-fabricated vs. FIB-fabricated AFM-SECM probes

Initial proof of concept studies show localized detection of ATP at the surface of live epithelial cell monolayers with batch-fabricated AFM-SECM probes exhibiting an electroactive area in the µm range. However, there are several limitations associated with the use of batch-fabricated AFM-SECM probes. The tip length (sensitivity) and the outer electrode diameter (resolution) are typically in the range of 2.5 µm to 6 µm (*Figure*

5.13A), respectively. Also, the cantilever arm is comparatively wide (approx. 30 µm, *Figure 5.13B*), and due to the close position to the sample (tip length approx. 2.5 µm) leads to additional diffusion hindrance potentially interfering with the diffusion of glucose from the bulk solution. Additionally, batch-fabricated AFM-SECM probes are made from silicon as a bulk material. Due to the semiconducting nature of silicon, caution has to be taken not to harm the insulation layer between silicon and electrode material since this induces interferences with the recorded current signal.

On the other hand, FIB-fabricated AFM-SECM probes with integrated PtC electrodes offer several advantages in the tip dimensions due to the customized FIB process (*Figure 5.13C*). The tip length for individual probes is variable allowing the adaptation of tip length; the electrode can be positioned in an optimized distance to the sample surface, improving the sensitivity of the electrochemical measurement. Additionally, the critical electrode dimension (edge length of the frame electrode) is reduced compared to batch-fabricated probes leading to improved electrochemical resolution. Despite the smaller electrode dimension steady-state currents observed at tip-integrated PtC electrodes are in the same range as current values recorded at batch-fabricated probes. This can be attributed to the fact that batch-fabricated electrodes are typically slightly recessed, whereas PtC electrodes are protruding, thereby enhancing the current. Therefore, FIB-fabricated AFM-SECM probes with tip-integrated PtC electrodes are promising alternatives for ATP detection at live epithelial cell monolayers.

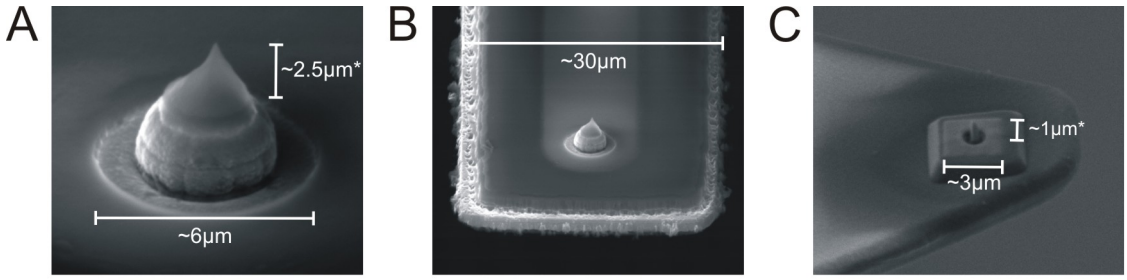

Figure 5.13. SEM images comparing critical dimensions of batch-fabricated (A and B) and FIB-fabricated (C) AFM-SECM probes. Asterisks indicate that dimensions are tilt-corrected.

5.3.6 PtC composite electrodes as transducer for H_2O_2 oxidation

As H_2O_2 is the target analyte in the proposed biosensor design, PtC composite electrodes were evaluated towards their functionality in respect to electron transfer rates and stability as transducer for the oxidation of H_2O_2. Similar to the majority of electrochemical studies presented in *Chapter 4*, platinum disk UMEs modified with PtC layers were used for this optimization and for studies presented in *Section 5.3.7*. Again, time and cost efficiency are the relevant driving force.

The current response to the oxidation of H_2O_2 at 0.65 V (vs. SCE) was evaluated for pristine and post-treated PtC UMEs. *Figure 5.14* shows a typical amperometric response curve obtained after addition of H_2O_2 to PBS solution at a biased post-deposition FIB-milled PtC UME. As expected, every addition of H_2O_2 results in a corresponding current increase proportional to the concentration. As a control, the last addition was PBS (marked with a black arrow) showing no oxidative current response.

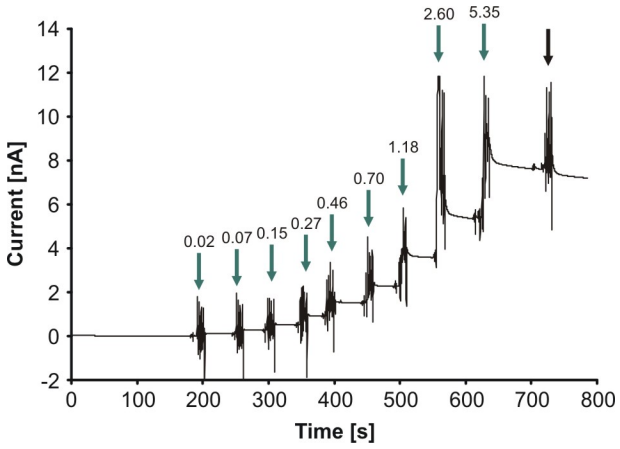

Figure 5.14. Amperometric response curve obtained at a FIB-milled PtC UME (biased at 0.65 V vs. SCE) by adding H_2O_2 to PBS solution. H_2O_2 additions are marked with green arrows and PBS addition with black arrow. Numbers above the arrows correspond to the final concentration in [mM] after each addition of H_2O_2.

Calibration curves for pristine, FIB-milled and annealed PtC layers are shown in comparison to platinum UMEs as reference material in *Figure 5.15*. For comparative purposes, each current response was normalized to average electrode areas obtained from CVs in $Ru(NH_3)_6^{3+/2+}$ for the respective type of electrodes. Pristine PtC layers show a sluggish oxidation behavior for H_2O_2, and hence, are not suitable as transducers. As discussed in the previous chapter, the high carbon content of these layers presumably inhibits fast electron transfer. Pretreatment techniques such as annealing or post-deposition milling lead to an improved response for H_2O_2 oxidation. As previously discussed, a decrease of carbon content within the layer is leading to an enhanced amount of surficial platinum, and platinum is electro-catalytically active towards the oxidation of H_2O_2[26, 27]. Comparing the response of pretreated PtC layers to pure platinum shows that annealing at approx. 400 ºC leads to a response of 119.9 ± 33.8 pA μm^{-2} at 5.35 mM H_2O_2 (pure platinum 156.6 ± 2.8 pA μm^{-2}). FIB-milled PtC layers lead to a current response of 100.1 ± 12.1 pA μm^{-2} at the same H_2O_2 concentration. Summarizing this

observation indicates that the presence of carbon in the bulk does not impair the electrode quality, however, the composition and platinum content of the surficial layer appears to be the crucial factor. Compared to the pristine PtC UMEs (8.3 ± 1.1 pA μm^{-2}), the current response improves approx. 12 - 15 fold after the treatment. The loss in linearity observed at treated PtC and bare platinum UMEs, which is evident at H_2O_2 concentrations exceeding approx. 1 mM, has been previously attributed to a saturation of the platinum surface by the adsorption of H_2O_2 and O_2[28].

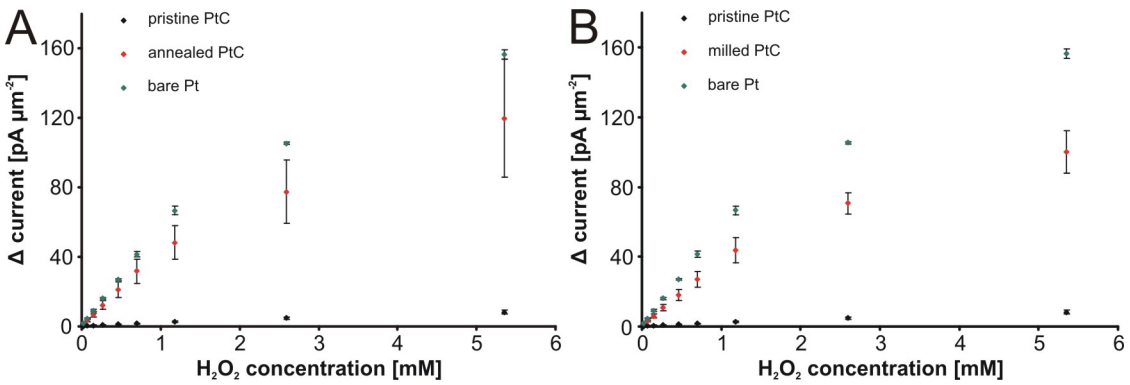

Figure 5.15. Calibration curves for annealed (A) and FIB-milled (B) PtC UMEs in comparison to pristine PtC and bare Pt. Annealing was performed at 400 °C. Calibration curves were obtained from amperometric response curves during addition of H_2O_2 to PBS at a UME bias of 0.65 V vs. SCE (n = 3).

Annealed PtC layers are the preferred transducers from the perspective of their kinetic behavior, however the annealing procedure cannot be applied to AFM-SECM probes due to cantilever bending induced by the thermal treatment. Also, the post-deposition FIB milling step seems to result in a more reproducible response as can be derived from the statistical evaluation. Calibration curves shown in *Figure 5.15* are average current responses obtained from three different FIB-milled PtC UMEs. Repetitive measurements at one FIB-milled PtC UME lead to an almost identical result (100.0 ± 9.9 pA μm^{-2} at

5.35 mM H_2O_2, n = 3). Results obtained in these experiments show that milled PtC layer electrodes are suitable for oxidation of H_2O_2 and will be evaluated in the following as biosensor transducers.

5.3.7 Glucose biosensors based on post-deposition FIB-milled PtC UMEs

Similar to results presented in *Sections 5.3.3* and *5.3.4*, biosensors were prepared by entrapment of enzymes in an EDP film precipitated by a locally-induced pH shift. Given the limited availability of Canguard, alternative EDPs have to be investigated for future applications. Thus, Resydrol was used as an EDP in the following section which has not yet been characterized as thoroughly as Canguard. Pulse polymerization procedures have been optimized with respect to pulse cycles, applied potentials and pulse duration. Although electron transfer kinetics of H_2O_2 at FIB-milled PtC UMEs were characterized in the previous section, evaluation of the polymerization procedure at milled PtC layers is required since e.g. the difference in electrode shape might lead to altered polymer precipitation or mechanical stability of the deposited layer. GOx-based biosensors were prepared as a model for the more complex dual enzymatic system required for ATP detection.

EDP layers were deposited with similar pulse polymerization protocols as previously developed in our research group[29], while focusing on variation of the number of pulse cycles to optimize polymer film thickness. *Figure 5.16A* depicts an amperometric response curve for the addition of glucose obtained at a glucose biosensor biased at 0.65 V. *Figure 5.16B* shows a representative calibration curve averaged from response curves at three different glucose biosensors prepared with five deposition cycles. The

biosensors saturate at a current response of approx. 12 pA corresponding to a glucose concentration of 15 mM. The sensitivity is approx. 1 pA mM^{-1} in a linear range of 0 – 9 mM. Normalization of this sensitivity to an average electrode surface area retrieved from CVs in $Ru(NH_3)_6^{3+/2+}$ results in a value of 1.38 mA M^{-1} cm^{-2}, which lies in the reported range for GOx-based biosensors[30-32].

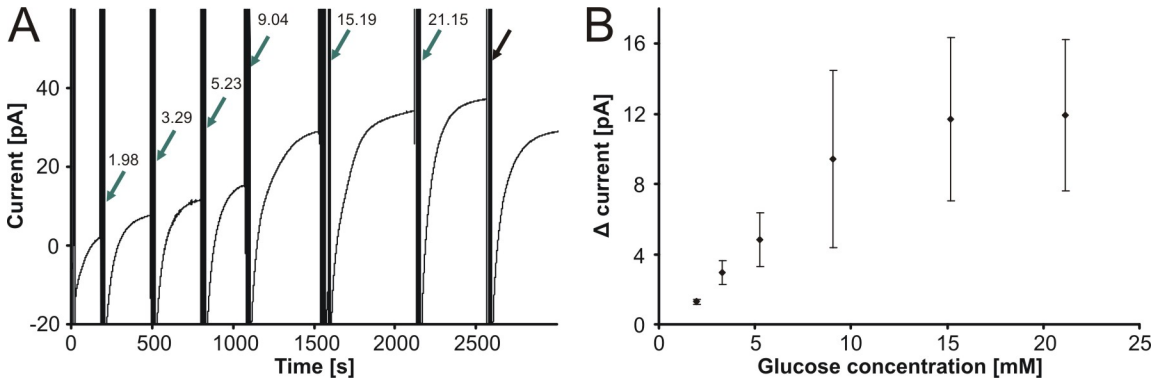

Figure 5.16. (A) Amperometric response curve obtained at a FIB-milled PtC UME based glucose biosensor (biased at 0.65 V vs. SCE). Glucose additions to PBS solution are marked with green arrows; PBS addition is marked with black arrow. Numbers above the arrows correspond to the final concentration in [mM] after each spike of glucose. (B) Average calibration curve obtained from amperometric current response during addition of glucose at FIB-milled PtC UMEs based GOx biosensor (n = 3, E = 0.65 V vs. SCE).

Figure 5.16A reveals that the steady-state response time, which is the time required to reach 90 % of the steady-state response after analyte addition[33], is on the order of 300 s. This value represents an average derived from individual response times after single glucose additions for one particular run. A summary of response times for experiments recorded at glucose biosensors prepared with different cycle numbers is shown in *Figure 5.17*. This data indicates that generally a larger saturation current results in a slower biosensor response. Ideally, a saturation current in the range of 18 pA is expected from

extrapolation of data reported at platinum disk electrodes with a diameter of 25 µm[29]. For saturation currents in this range, the response time is on the order of 300 - 400 s, which is not acceptable for targeted imaging experiments with these biosensors and additionally is 20 – 40 x increased compared with previously observed response times at platinum electrode-based glucose biosensors[29]. Nevertheless, observed saturation currents and sensitivities are in a similar range as expected from other studies, which is very encouraging.

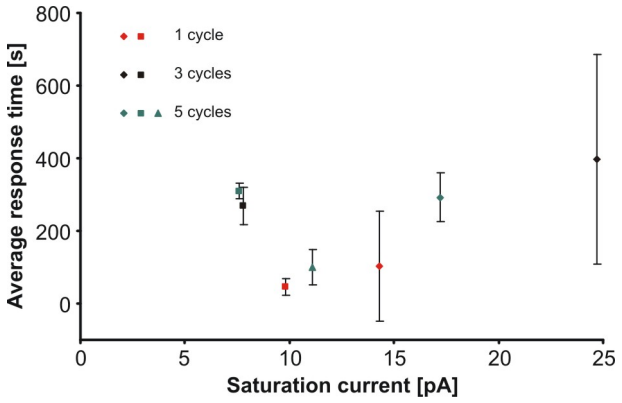

Figure 5.17. Average response time as a function of saturation current obtained at glucose biosensors deposited with different numbers of cycles.

Although H_2O_2 additions also resulted in minor sporadic baseline drift, response times until a stable signal/drift was reached were typically on the order of 15 s. Therefore, it can be concluded that the slow response time observed at glucose biosensors is not related to poor electron transfer kinetics. *Figure 5.18* shows a representative optical microscopy image of an EDP layer deposited at a FIB-milled PtC UME. It is noticed that the polymer film seems to extend over the edges of the PtC UME in a ring shape as previously observed at regular Pt UME. However, compared to conventional polished

platinum UMEs PtC surfaces exhibit a rougher surface morphology next to having a different composition. It may be hypothesized that these differences result in a thicker EDP layer which may contribute to an increase in biosensor response time due to an increased diffusion path of H_2O_2.

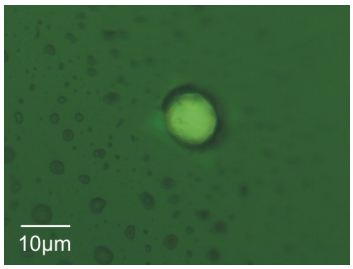

Figure 5.18. Optical micrograph of EDP layer containing glucose oxidase deposited at FIB-milled PtC UME using 5 deposition cycles.

These studies indicate that EDP layers are promising immobilization matrices at FIB-milled PtC electrodes since satisfying saturation current levels and sensitivities are observed. However, further adaptation of previously reported polymerization protocols is required to optimize the biosensor response time. Application of shorter or lower potential pulses is suggested as an improvement, which generally leads to a higher permeability of the polymer layer. Additionally, such a change of parameters is also advantageous for enzyme stability as it implies a lower potential-induced stress and smaller pH variation.

5.4 Final remarks

Live epithelial cell monolayers were characterized thoroughly by means of contact mode and dynamic mode AFM. Epithelial cells were found to be stable towards imaging for a

longer amount of time. Additionally, dynamic mode studies showed that soft cell surfaces are very sensitive to the applied force resulting either in loss of resolved features (low force) or indentation of surfaces (high force). Imaging of epithelial cell monolayers at different times after plating did not result in substantial differences of cell morphology or shapes. AFM-SECM feedback experiments revealed that feedback currents are sensitive for topographical surface features due to surface roughness of the cells. Forces applied to the cell surfaces have to be controlled and optimized carefully, since height variations of the cells are in the range of the tip lengths (for FIB-fabricated AFM-SECM probes). However, application of low force contact mode AFM results in substantial improvement of current convolution.

SECM-based detection of ATP was achieved at live epithelial cell surfaces. A dual-UME based device was used to position ATP biosensors in close proximity to cell monolayers. Dual-UMEs were scanned across the edge between an insulating surface and an epithelial cell monolayer. Non-invasive release of ATP was observed and confirmed in control experiments by adding excess of free-diffusing HEX. The ATP biosensors were further miniaturized and integrated into batch-fabricated AFM-SECM probes. Laterally resolved detection of ATP was achieved in these proof of concept studies.

Since there are several drawbacks of batch-fabricated AFM-SECM probes for targeted life cell imaging, PtC-based electrodes were evaluated as H_2O_2 transducers. It was found that pristine PtC layers are not suitable due to the high amount of carbon present at the composite material surface. Pretreatment of PtC UMEs via annealing or post-deposition FIB milling leads to a significant improvement of H_2O_2 electrooxidation, similar to the behavior of pure platinum. FIB-milled PtC UMEs were further tested as transducer

platforms for glucose biosensors. It was found that although sensitivity and saturation currents observed are satisfying and in agreement with results reported in literature, the response time of the biosensors at this point is not acceptable. Biosensors were also fabricated at AFM-SECM tip-integrated PtC electrodes, however, not yet applied during quantitative studies.

Combining all experimental improvements obtained throughout these studies with further optimization of the polymerization procedure, a successful miniaturized tip-integrated ATP biosensor providing localized measurements of ATP concentration levels at live epithelial cells is anticipated. As a last improvement, variation of potentials and pulse time is suggested to improve the permeability and porosity of the EDP layer. Additionally, shorter enzyme storage times prior to the polymerization may lead to an enhanced enzymatic response behavior.

5.5 References

(1) Engstrom, R. C.; Weber, M.; Wunder, D. J.; Burgess, R.; Winquist, S. *Measurements within the diffusion layer using a microelectrode probe*, Anal. Chem. **1986**, *58*, 844-848.

(2) Liu, H. Y.; Fan, F. R. F.; Lin, C. W.; Bard, A. J. *Scanning electrochemical and tunneling ultramicroelectrode microscope for high-resolution examination of electrode surfaces in solution*, J. Am. Chem. Soc. **1986**, *108*, 3838-3839.

(3) Bard, A. J.; Fan, F. R. F.; Kwak, J.; Lev, O. *Scanning electrochemical microscopy. Introduction and principles*, Anal. Chem. **1989**, *61*, 132-138.

(4) Horrocks, B. R.; Schmidtke, D.; Heller, A.; Bard, A. J. *Scanning electrochemical microscopy. 24. Enzyme ultramicroelectrodes for the measurement of hydrogen peroxide at surfaces*, Anal. Chem. **1993**, *65*, 3605-3614.

(5) Kueng, A.; Kranz, C.; Mizaikoff, B. *Imaging of ATP membrane transport with dual micro-disk electrodes and scanning electrochemical microscopy*, Biosens. Bioelectron. **2005**, *21*, 346-353.

(6) Hengstenberg, A.; Kranz, C.; Schuhmann, W. *Facilitated tip-positioning and applications of non-electrode tips in scanning electrochemical microscopy using a shear force based constant-distance mode*, Chem.--Eur. J. **2000**, *6*, 1547-1554.

(7) Kueng, A.; Kranz, C.; Lugstein, A.; Bertagnolli, E.; Mizaikoff, B. *AFM-tip-integrated amperometric microbiosensors: High-resolution imaging of membrane transport*, Angew. Chem., Int. Ed. **2005**, *44*, 3419-3422.

(8) Kueng, A.; Kranz, C.; Mizaikoff, B. *Scanning probe microscopy with integrated biosensors*, Sens. Lett. **2003**, *1*, 2-15.

(9) Masson, J.-F.; Kranz, C.; Mizaikoff, B.; Gauda, E. B. *Amperometric ATP microbiosensors for the analysis of chemosensitivity at rat carotid bodies*, Anal. Chem. **2008**, *80*, 3991-3998.

(10) Becchetti, A.; Malik, B.; Yue, G.; Duchatelle, P.; Al-Khalili, O.; Kleyman, T. R.; Eaton, D. C. *Phosphatase inhibitors increase the open probability of ENaC in A6 cells*, Am J Physiol Renal Physiol **2002**, *283*, F1030-1045.

(11) Shin, H.; Hesketh, P. J.; Mizaikoff, B.; Kranz, C. *Batch Fabrication of Atomic Force Microscopy Probes with Recessed Integrated Ring Microelectrodes at a Wafer Level*, Anal. Chem. **2007**, *79*, 4769-4777.

(12) Shin, H.; Hesketh, P. J.; Mizaikoff, B.; Kranz, C. *Development of wafer-level batch fabrication for combined atomic force-scanning electrochemical microscopy (AFM-SECM) probes*, Sens. Actuators, B **2008**, *B134*, 488-495.

(13) Smith, P. R.; Bradford, A. L.; Schneider, S.; Benos, D. J.; Geibel, J. P. *Localization of amiloride-sensitive sodium channels in A6 cells by atomic force microscopy*, Am. J. Physiol. **1997**, *272*, C1295-C1298.

(14) Hansma, P. K.; Cleveland, J. P.; Radmacher, M.; Walters, D. A.; Hillner, P. E.; Bezanilla, M.; Fritz, M.; Vie, D.; Hansma, H. G.; et al. *Tapping mode atomic force microscopy in liquids*, Appl. Phys. Lett. **1994**, *64*, 1738-1740.

(15) Putman, C. A. J.; van der Werf, K. O.; De Grooth, B. G.; Van Hulst, N. F.; Greve, J. *Tapping mode atomic force microscopy in liquid*, Appl. Phys. Lett. **1994**, *64*, 2454-2456.

(16) Le Grimellec, C.; Giocondi, M.-C.; Pujol, R.; Lesniewska, E. *Tapping mode atomic force microscopy allows the in situ imaging of fragile membrane structures and of intact cells surface at high resolution*, Single Molecules **2000**, *1*, 105-107.

(17) Liu, B.; Rotenberg, S. A.; Mirkin, M. V. *Scanning electrochemical microscopy of living cells: different redox activities of nonmetastatic and metastatic human breast cells*, Proc. Natl. Acad. Sci. U. S. A. **2000**, *97*, 9855-9860.

(18) Le Grimellec, C.; Lesniewska, E.; Giocondi, M.-C.; Finot, E.; Vie, V.; Goudonnet, J.-P. *Imaging of the surface of living cells by low-force contact-mode atomic force microscopy*, Biophys. J. **1998**, *75*, 695-703.

(19) Lesniewska, E.; Milhiet, P. E.; Giocondi, M.-C.; Le Grimellec, C. *Atomic Force Microscope Imaging of Cells and Membranes*, In *Atomic Force Microscopy in Cell Biology*; Jena, B. P., Hoerber, H. J. K., Eds.; Academic Press: San Diego, 2002; Vol. 68.

(20) Kueng, A.; Kranz, C.; Mizaikoff, B.; Lugstein, A.; Bertagnolli, E. *Combined scanning electrochemical atomic force microscopy for tapping mode imaging*, Appl. Phys. Lett. **2003**, *82*, 1592-1594.

(21) Scheller, F.; Pfeiffer, D. *Glucose oxidase-hexokinase bienzyme electrode sensor for adenosine triphosphate*, Anal. Chim. Acta **1980**, *117*, 383-386.

(22) Compagnone, D.; Guilbault, G. G. *Glucose oxidase/hexokinase electrode for the determination of ATP*, Anal. Chim. Acta **1997**, *340*, 109-113.

(23) Anicet, N.; Bourdillon, C.; Moiroux, J.; Saveant, J.-M. *Step-by-Step Avidin-Biotin Construction of Bienzyme Electrodes. Kinetic Analysis of the Coupling between the Catalytic Activities of Immobilized Monomolecular Layers of Glucose Oxidase and Hexokinase*, Langmuir **1999**, *15*, 6527-6533.

(24) Kurzawa, C.; Hengstenberg, A.; Schuhmann, W. *Immobilization method for the preparation of biosensors based on ph shift-induced deposition of biomolecule-containing polymer films*, Anal. Chem. **2002**, *74*, 355-361.

(25) Kueng, A.; Kranz, C.; Mizaikoff, B. *Amperometric ATP biosensor based on polymer entrapped enzymes*, Biosens. Bioelectron. **2004**, *19*, 1301-1307.

(26) Hall, S. B.; Khudaish, E. A.; Hart, A. L. *Electrochemical oxidation of hydrogen peroxide at platinum electrodes. Part 1. An adsorption-controlled mechanism*, Electrochim. Acta **1997**, *43*, 579-588.

(27) Hall, S. B.; Khudaish, E. A.; Hart, A. L. *Electrochemical oxidation of hydrogen peroxide at platinum electrodes. Part II: effect of potential*, Electrochim. Acta **1998**, *43*, 2015-2024.

(28) Zhang, Y.; Wilson, G. S. *Electrochemical oxidation of hydrogen peroxide on platinum and platinum + iridium electrodes in physiological buffer and its applicability to hydrogen peroxide-based biosensors*, J. Electroanal. Chem. **1993**, *345*, 253-271.

(29) Weber, C.; Mizaikoff, B.; Kranz, C. *unpublished results*, **2008**.

(30) Szamocki, R.; Velichko, A.; Muecklich, F.; Reculusa, S.; Ravaine, S.; Neugebauer, S.; Schuhmann, W.; Hempelmann, R.; Kuhn, A. *Improved enzyme immobilization for enhanced bioelectrocatalytic activity of porous electrodes*, Electrochem. Commun. **2007**, *9*, 2121-2127.

(31) Cosnier, S.; Szunerits, S.; Marks, R. S.; Novoa, A.; Puech, L.; Perez, E.; Rico-Lattes, I. *A rapid and easy procedure of biosensor fabrication by micro-encapsulation of enzyme in hydrophilic synthetic latex films. Application to the amperometric determination of glucose*, Electrochem. Commun. **2000**, *2*, 851-855.

(32) Csoeregi, E.; Schmidtke, D. W.; Heller, A. *Design and Optimization of a Selective Subcutaneously Implantable Glucose Electrode Based on "Wired" Glucose Oxidase*, Anal. Chem. **1995**, *67*, 1240-1244.

(33) Thevenot, D. R.; Toth, K.; Durst, R. A.; Wilson, G. S. *Electrochemical biosensors: recommended definitions and classification*, Pure Appl. Chem. **1999**, *71*, 2333-2348.

6 CONCLUSIONS AND OUTLOOK

The main goal of this thesis was to improve AFM-SECM based sensing platforms for biological applications in several aspects including implementation of thin insulation layers, and increasing of the tip-integrated electrode size. PFE-insulated AFM-SECM probes with thin insulation layers were successfully developed, and applied for combined AFM-SECM measurements. Moreover, IBID-based PtC composites were applied as electrode materials for the first time including a detailed physical and electrochemical characterization, and successful integration into bifunctional AFM-SECM probes. Live epithelial cell monolayers were studied with AFM and for the first time ATP was detected with amperometric biosensors during non-invasive SECM, and laterally-resolved AFM-SECM studies.

Plasma-polymerized PFE membranes were applied as novel insulation layers for AFM-SECM probes and UMEs. It was shown that a decrease of layer thickness of 2 - 3 x compared to state-of-the-art insulation materials such as Parylene C or silicon nitride/silicon oxide was achieved without impairing the insulation quality. Specifically, layer thicknesses of < 300 nm were reported with excellent insulating properties. Long-term studies revealed an approximate 20 % increase with time in the observed faradaic current; however, this was confirmed as minor obstacle in relation to the time scale of typical AFM-SECM experiments. Combined approach and cantilever deflection curves were recorded along with AFM-SECM imaging revealing excellent lateral resolution. Future improvements of plasma-polymerized PFE layers should focus on improving the cross-linking density of the polymer film to further enhance the long-term stability.

Moreover, optimization of the oxygen plasma cleaning step implemented prior to PFE layer deposition should be performed, which should lead to advanced adhesion of the layer. Both improvements are expected to result in a better temporal stability of the PFE insulation layer. Furthermore, PFE-insulated AFM-SECM probes should be tested at live epithelial cell monolayers for imaging studies and AFM-SECM based biosensor performance. One major expected advantage of the thin polymeric insulation material is the rather minor alteration of the cantilevers force constant, thereby improving the potential for future dynamic mode AFM-SECM applications.

Ion beam induced deposition was used to fabricate PtC composites at precisely located positions. The materials were thoroughly characterized in respect of physical and electrochemical properties including EDX studies, Raman analysis, FPP, and AFM along with CV. PtC electrodes deposited at AFM-SECM cantilevers lead to an increase in electrode area, as derived from CV studies, thus fulfilling the purpose of increasing tip-integrated electrodes without substantially limiting the electrochemical resolution of combined AFM-SECM experiments. However, it was found that the pristine material contained a high fraction of carbon, which impaired the electrode behavior in respect to certain applications, such as oxidation of surface sensitive mediators (e.g. $Fe(CN)_6^{3-/4-}$). Therefore, different pre-treatment strategies were evaluated focusing on the removal of carbon in the electroactive deposits. EDX analysis revealed that thermal annealing of PtC composites above 400 ºC decreased the carbon fraction to approx. 5 at%. Graphitization of carbon prior to removal was observed during Raman spectroscopic studies. Summarizing, annealing of PtC electrodes lead to a substantial improvement of the electrochemical behavior, as confirmed by simulations, by almost three orders of

magnitude for the standard heterogeneous rate constant for the oxidation of $Fe(CN)_6^{3-/4-}$. However, thermal annealing also induced unacceptable bending of AFM cantilevers. Alternatively, UV/ozone treatment and post-deposition FIB milling were evaluated for improvement of the charge transfer characteristics at the electrode. UV/ozone treatment indicated complex mechanisms of the occurring surface chemistry, which are beyond the scope of this work; however, post-deposition FIB milling proved a successful improvement of the observed charge transfer characteristics along with the advantage of applicability at AFM-SECM cantilevers. Continuing efforts to enhance fundamental understanding on PtC materials should concentrate on a thorough evaluation of the mechanisms involved during UV/ozone treatment. In addition, in-depth physical characterization of these materials and post-deposition milled PtC features should be performed to quantify the electrochemically observed improvements in terms of physical material parameters. Since IBID-based fabrication offers the advantage of selecting pattern shapes and dimensions, different pattern geometries should be evaluated for tip-integrated electrodes such as fine grid structures expecting to increase the currently observed steady-state currents.

Finally, thorough AFM investigations at live epithelial cell layers were performed. It was found that epithelial cell layers were readily amenable to extended AFM imaging, although the transferred force from the tip to the sample has to be optimized carefully. AFM imaging at different times after plating did not reveal any substantial differences of the cell morphological features. AFM-SECM based feedback mode imaging was performed revealing that the faradaic current was sensitive to the elevated surface features of the cells. During low-force contact mode AFM, current features were

substantially improved highlighting the need for particularly careful force optimization during AFM-SECM based measurements, since the surface features observed are in the range of the AFM tip length for to date FIB-fabricated AFM-SECM probes. ATP biosensors were used to detect ATP release at live epithelial cell monolayers by two different approaches: non-invasive SECM-based experiments were performed, along with further miniaturization of the sensing device by integration into batch-fabricated AFM-SECM probes. AFM-SECM studies have for the first time demonstrated the potential for locally-resolved measurements of ATP at the surface of live biological specimen. In both experimental studies the presence of ATP was confirmed by appropriate control experiments. PtC-based materials introduced in this thesis were further investigated as transducer platforms for oxidase-based biosensors. It was discovered that the transducer response toward electrooxidation of H_2O_2 was substantially improved for annealed and FIB-milled PtC UMEs in comparison to pristine materials almost showing the behavior of pure platinum. Glucose biosensors based on FIB-milled PtC-based UMEs were furthermore tested, and it was found that sensitivity and saturation currents observed were satisfying, although currently lacking the response time needed for imaging experiments. It is suggested that future applications focus on the optimization of the biosensor fabrication procedure in order to obtain an improved permeability and porosity of the EDP layer. Additionally, continuing research should evaluate alternative shapes of PtC-patterned electrodes at combined AFM-SECM probes. For example the implementation of grid structures is also expected to advance the mechanical stability of EDP-based biosensors due to improving adhesion effects via a controlled surface roughness. It is anticipated that combining the improvements described throughout this

thesis will result in improved miniaturized AFM tip-integrated ATP biosensors for routine localized detection of ATP at the surface of live biological specimen.